THE ZEEMAN-RAMAN AND -INFRARED SPECTRA OF TRANSITION-METAL IONS IN SINGLE CRYSTALS

A thesis submitted in partial fulfilment
of the requirements for the Degree of
Doctor of Philosophy in Physics
in the University of Canterbury
Christchurch, New Zealand

by

Meng Hau Kuok

1977

To

My parents

ABSTRACT

The results of Raman and infrared investigations of the spectra of Co^{2+} ions in $CsCdCl_3$ and $CsMgCl_3$ are reported. These ions substitute for the divalent cations in these double chlorides and experience a trigonal crystal field which splits the four spin-orbit levels of the $^4T_{1g}(^4F)$ ground manifold into six Kramers doublets with energies lying within 0 - 1400 cm^{-1}. Electronic transitions within this ground term have been observed and are satisfactorily fitted using the complete $3d^7$ configuration crystal field matrices. Zeeman-Raman and -infrared experiments on $CsCdCl_3$:Co and $CsMgCl_3$:Co have been performed and yield g values for the excited electronic states. These excited state g values are also calculated using crystal field theory and are in good agreement with those obtained experimentally. Selection rules governing the occurrence of the electronic Zeeman transitions are derived for the appropriate cobalt ion site symmetries and are in agreement with the results. The Raman and infrared spectra of Co^{2+} ions in $CsCoCl_3$ and $KCdCl_3$ are measured and are presented, together with the results of optical studies of Co^{2+} ions in $CsCdCl_3$. A preliminary investigation of the electronic transitions of Fe^{2+} ions in $CdCl_2$-type crystals has been carried out using Raman and infrared spectroscopy. The spectral data, together with a tentative analysis, are presented.

ACKNOWLEDGMENTS

Many fellow postgraduate colleagues and members of the academic and technical staff of the Physics Department have assisted in the preparation and presentation of this thesis. I am indebted to all of them, but more especially to the following people.

I wish to express my gratitude to Professors A.G. McLellan, B.G. Wybourne and W.L. Jones for accepting me as a postgraduate student and the tax-payers of New Zealand for providing me with a Teaching Fellowship.

I greatly appreciate the help of my amiable supervisor, Dr. Glynn D. Jones. His unflagging optimism, enthusiasm and morale-boosting confidence have carried me through this research project. Thanks are due to Dr. Rod W. Syme for helpful discussions, useful suggestions and his supervision during Dr. Jones' absence. Sincere thanks go to my old mate Chris Tomblin for experimental assistance and his companionship.

My acknowledgment is extended to the following:

Messrs. Bob Tyree and Terry Rowe for technical assistance and advice;

Tom Walker for his prompt supply of cryogenic refrigerants;

Ross Ritchie for growing some of the crystals;

Laurie Hunter for his high quality photographic work;

Ms Philippa MacLean for tracing the diagrams; and

Mrs. Mary Boswell for the neat typing of this thesis.

My parents are a constant inspiration to me. I am deeply indebted to them for this, their understanding, moral and financial support.

Last, but not least, I am grateful to Bill and Jean Orchard for providing me with a home from home.

Meng Hau Kuok

24 November, 1977.

CONTENTS

LIST OF FIGURES

LIST OF TABLES

CHAPTER I

INTRODUCTION

The principal part of this research work involves the investigation of the electronic spectra of the cobaltous ions present as impurities in single crystals of $CsCdCl_3$ and $CsMgCl_3$. The divalent cobalt ions substitute for the divalent cations in these double chlorides and experience a crystalline field of predominantly cubic symmetry with a slight trigonal distortion.

The electronic transitions of interest are between the spin-orbit and trigonal crystal field states of the $^4T_{1g}$ cubic field ground term. They are readily observed by Raman scattering and infrared absorption spectroscopy. Analyses of the spectra recorded were made using crystal field theory. The energy levels of the cobalt ion were calculated using all 120 energy states of the $3d^7$ configuration.

The $CsMgCl_3$:Co and $CsCdCl_3$:Co systems differ in several respects. For the centrosymmetric $CsMgCl_3$:Co, electric dipole transitions within the d^7 configuration are strictly forbidden by Laporte's rule. Electronic transitions in $CsMgCl_3$:Co however were found to occur through the magnetic dipole mechanism. For $CsCdCl_3$, the majority of cobalt ions substitute for the C_{3v} cadmium ion sites. These sites lack inversion symmetry so the electronic transitions observed are electric dipole allowed and are thus more intense than those of $CsMgCl_3$:Co.

The goal of this work was to measure the Zeeman effect on the cobalt spectra. There are several reasons for this. Firstly only a magnetic field can lift the Kramer's degeneracy of the cobalt ion energy levels. Secondly Zeeman studies could test the adequacy or otherwise of the crystal field theory for interpreting the spectra obtained. Finally such studies could help identify the many vibronic absorptions encountered in the infrared spectra. The lines of the spectra of cobalt ions in $CsMgCl_3$ and $CsCdCl_3$ are sufficiently intense and narrow for

Zeeman-Raman and -infrared investigations to be feasible. No such investigation on any transition-metal ion has been reported in the literature.

An outline of the structure of this thesis is as follows.

Chapter II contains a description of the structures of the crystals examined. An account of the theory of single cobaltous ion spectra is given for the $CsMgCl_3$ and $CsCdCl_3$ systems. This includes the Hamiltonian interactions appropriate for the cobaltous ion and their associated parameters.

The experimental techniques and instruments employed for the infrared- and optical-absorption and Raman scattering experiments are documented in Chapter III. A section on the growth, orientation and preparation of the crystals is also included.

Chapters IV to VII deal with the zero-field and Zeeman-Raman and infrared investigations on the $CsMgCl_3$:Co and $CsCdCl_3$:Co systems and constitute the major portion of this thesis. The recorded spectra are presented, discussed and analysed using the complete $3d^7$ crystal field analysis of Chapter II. Magnetic splitting factors for the low-lying energy levels of the cobalt ion are determined from the Zeeman spectra.

A preliminary examination of $CsCoCl_3$ and cobalt-doped $KCdCl_3$ using Raman scattering and infrared absorption spectroscopy was performed. The spectral data are presented in Chapter VIII. Also included in this chapter are experimental results of optical absorption studies on $CsCdCl_3$:Co.

Preliminary Raman and infrared studies on the electronic spectra of the ferrous ion have initiated a new field of research in the department. $CdBr_2$ and $CdCl_2$ crystals are found to be suitable hosts for this ion. Intraconfigurational electronic transitions are expected to be only magnetic dipole allowed for the centrosymmetric $CdCl_2$-type system. However electric dipole electronic transitions were observed

for the ferrous-doped $CdBr_2$ in the infrared region thus inferring the manifestation of a Jahn-Teller distortion. Chapter IX is concerned with the Raman and infrared spectra of the ferrous ion.

Finally Chapter X contains an overall summary and conclusion of this thesis work undertaken, together with suggestions for further research.

CHAPTER II

THEORY

2.1 CRYSTAL STRUCTURE

2.1.1 $CsCdCl_3$

$CsCdCl_3$ [1] crystallizes in the hexagonal space group D^4_{6h}. There are two crystallographically distinct types of cadmium ions occupying sites of D_{3d} and C_{3v} symmetries and these are labelled Cd(1) and Cd(2) respectively. The unit cell shown in Fig.2-1 has six molecules which include two Cd(1) and four Cd(2) ions. In both sites the cadmium ions are surrounded by distorted octahedra of chloride ions. The chloride ions Cl(2) surrounding the Cd(1) ions form nearly perfect octahedra whereas the octahedra of chloride ions, Cl(1) and Cl(2), surrounding the Cd(2) ions are more distorted. The angle subtended at the Cd(2) ion by the Cl(2) ion and the threefold axis is 56.45° while the corresponding angle for the Cl(1) ion is 50.86°. As these angles are not too different and as the Cd(2)-Cl(2) distance (2.588Å) is about equal to the Cd(2)-Cl(1) distance (2.639Å), the C_{3v} symmetry of the Cd(2) ion site is approximately D_{3d}.

Two octahedra containing Cd(2) ions share a face forming a $[Cd_2Cl_9]^{5-}$ unit which then shares corners with six different octahedra containing Cd(1) ions.

2.1.2 $CsMgCl_3$ and $CsCoCl_3$

Both $CsMgCl_3$ [2] and $CsCoCl_3$ [3] are isostructural with the hexagonal $CsNiCl_3$ which belongs to the space group D^4_{6h} with two formula units per unit cell. The divalent cations occupy trigonal D_{3d} sites, the coordination spheres about them being octahedra of chloride ions. These octahedra share faces to form infinite parallel linear chains directed along the crystallographic c axis. Within a chain, pairs of divalent cations are bridged by three chloride ions. Fig.2-2 shows a perspective view of the unit cell content of these two compounds.

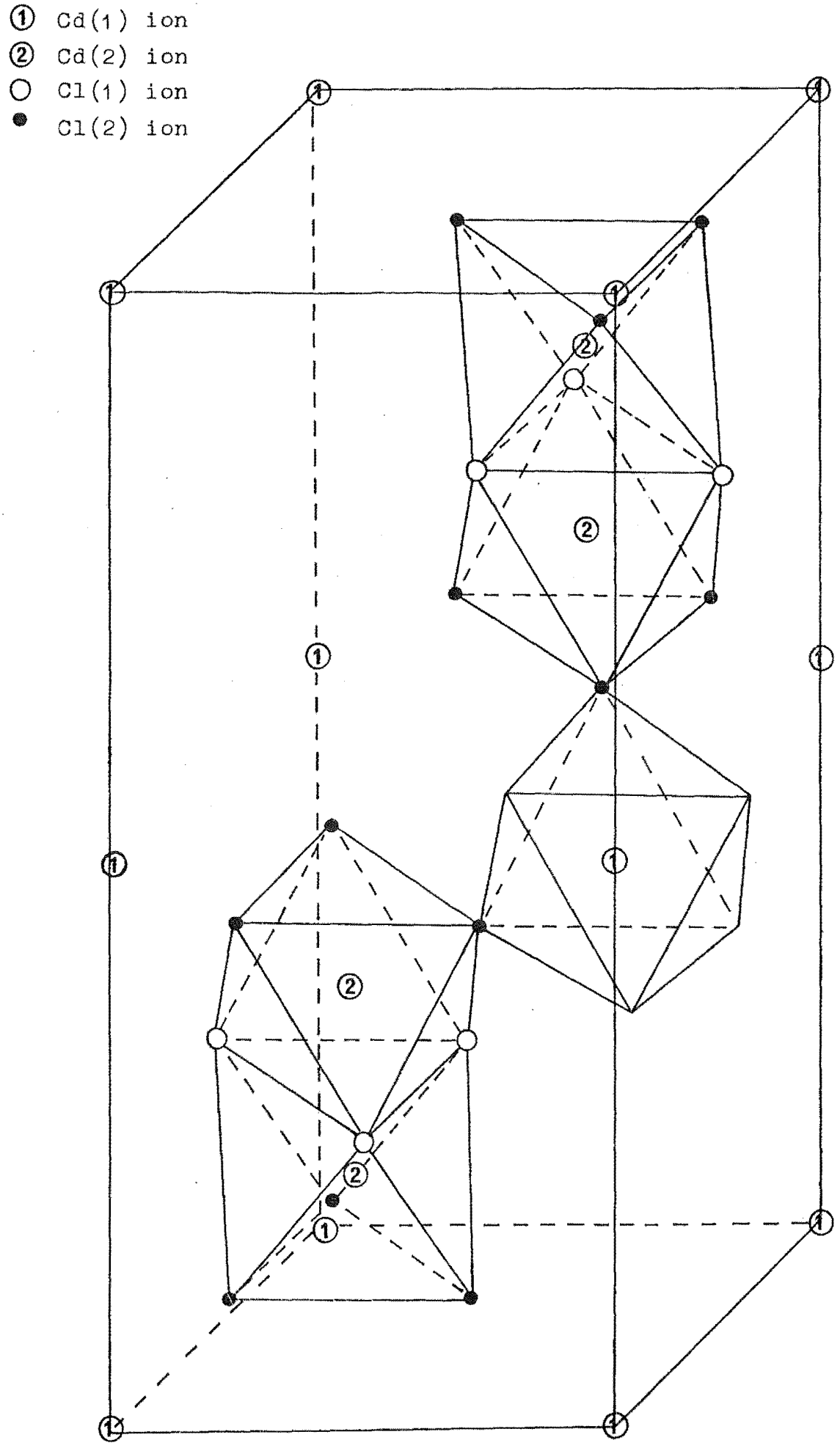

Fig. 2-1: Unit cell structure of the $CsCdCl_3$ crystal.

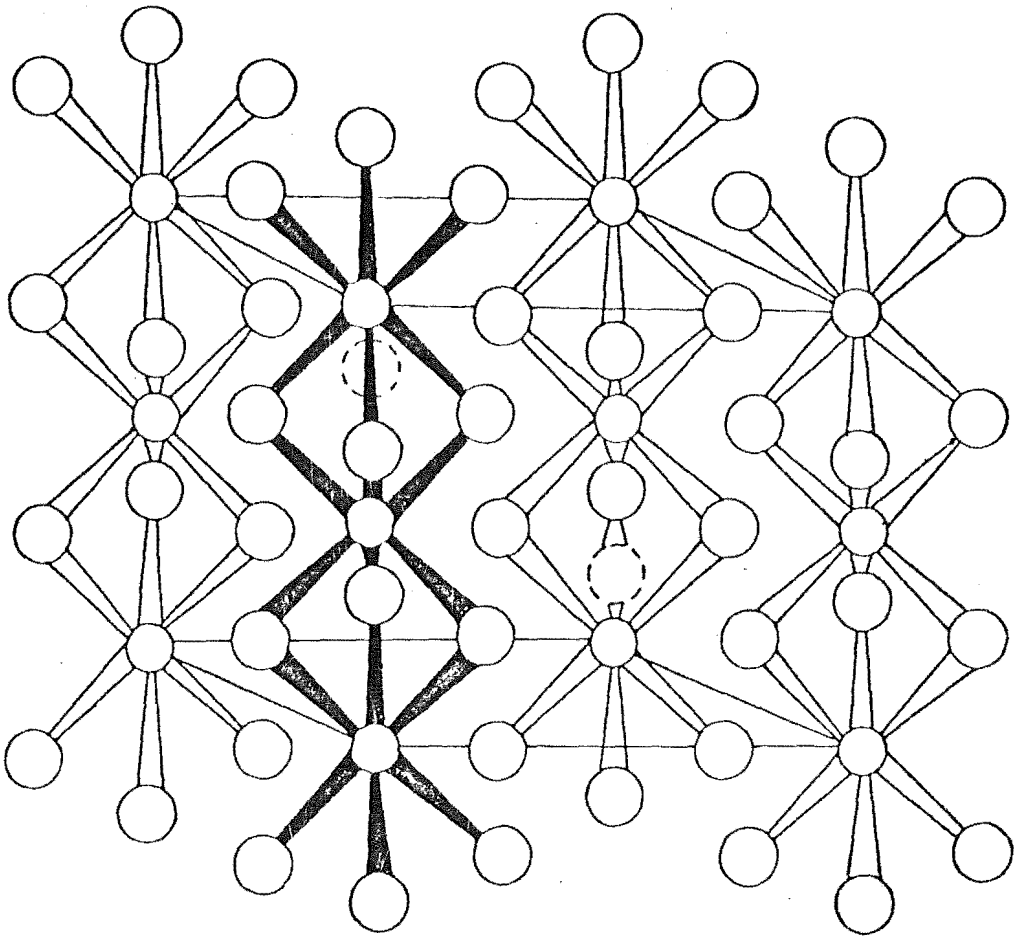

○ Mg, Co.

○ Cl.

◌ Cs.

Fig. 2-2: $CsMgCl_3$-type structure

2.1.3 $KCdCl_3$

$KCdCl_3$ is isomorphous[4],[5] with NH_4CdCl_3 which is orthorhombic with the space group D_{2h}^{16}. Each cadmium ion is located at a monoclinic C_s site and is surrounded by a distorted octahedron of chloride ions. This site symmetry can be approximately described by the C_{2h} point group[6]. The unit cell comprises four $KCdCl_3$ molecules.

2.1.4 $CdCl_2$ and $CdBr_2$

$CdBr_2$ has the $CdCl_2$-type structure which has the D_{3d}^5 space group with one molecule unit per unit cell[7]. The cadmium ion in $CdCl_2$ is located in the centre of a distorted octahedron of chloride ions and has a trigonal D_{3d} site symmetry. The $CdCl_2$ crystal comprises layers of chloride ions which are nearly cubic close packed, with cadmium ions sandwiched between alternative chloride-ion layers which are perpendicular to the crystal c axis.

2.2 THE THEORY OF SINGLE COBALTOUS ION SPECTRA

2.2.1 Introduction

In this work the double chlorides $CsMgCl_3$, $CsCdCl_3$, $CsCoCl_3$ and $KCdCl_3$ were examined. With the exception of $KCdCl_3$, the divalent cations of these crystals occupy sites of trigonal symmetry. The cobalt impurity ions substitute for the divalent cations in $CsMgCl_3$ and $CsCdCl_3$. Each Co^{2+} ion is surrounded by six chloride ligands forming a distorted octahedron with the degree of distortion varying from crystal to crystal. The Co^{2+} ion has a lowest-energy electronic configuration $[Ar]3d^7$ which possesses 120 states.

In a crystalline environment the appropriate Hamiltonian for a Co^{2+} ion is

$$\mathcal{H} = -\sum_i \left(\frac{\hbar^2}{2m}\nabla_i^2 + \frac{Ze^2}{r_i}\right) + \frac{1}{2}\sum_{i\neq j}\frac{e^2}{r_{ij}} + \sum_i \xi(r_i)\underline{\ell}_i\cdot\underline{s}_i + V \qquad (2.1)$$

where the summations are over all the electrons. The first term

represents the central field potential; the second term, the interelectronic repulsion and the third term, the spin-orbit coupling. The final term V represents the potential provided by the ion's ligands and may be written as

$$V = V_c + V_T \tag{2.2}$$

where V_c and V_T are the cubic and lower-symmetry crystal field potentials.

Application of an external magnetic field $\underline{H}$ adds an extra interaction term to the Hamiltonian (the Zeeman term) given by

$$\mathcal{H}_z = \beta \sum_i (\underline{\ell}_i + 2\underline{s}_i) \cdot \underline{H} = \beta (\underline{L} + 2\underline{S}) \cdot \underline{H} \tag{2.3}$$

where $\left(\beta = \frac{e\hbar}{2mc}\right)$ is the Bohr magneton.

The coulombic interaction among the seven d electrons gives rise to eight free-ion L-S multiplets ^4F, ^4P, ^2G, ^2F, $2x^2D$, ^2H and ^2P of which the lowest energy one is ^4F. This ^4F multiplet has sevenfold orbital and fourfold spin degeneracy. For the ion in a crystal field the degeneracy of all the multiplets are partially lifted to give terms which may be labelled by the irreducible representations (irreps) of the crystal field symmetry group. In a field of cubic symmetry, the Co^{2+} free-ion terms are split as follows:

$$\begin{aligned}
^4F &\rightarrow {}^4T_{1g} + {}^4T_{2g} + {}^4A_{2g} \\
^4P &\rightarrow {}^4T_{1g} \\
^2G &\rightarrow {}^2A_{1g} + {}^2E_g + {}^2T_{1g} + {}^2T_{2g} \\
^2D &\rightarrow {}^2E_g + {}^2T_{2g} \\
^2H &\rightarrow {}^2E_g + 2\,{}^2T_{1g} + {}^2T_{2g}
\end{aligned} \tag{2.4}$$

For the $3d^7$ configuration all these terms are even under inversion symmetry and this is signified by the subscript g.

The ground term $^4T_{1g}(^4F)$ of the cubic field is split by the spin-orbit

interaction into levels labelled by the irreps of the cubic double group. They are derived from the direct product of T_{1g} and the irrep Γ_8 of the spin $^3/_2$ function associated with the $^4T_{1g}$ term. The direct product yields $\Gamma_6^+, \Gamma_8^+, \Gamma_8'^+$ and Γ_7^+ states listed in order of increasing energy.

For crystals having D_{3d} or C_{3v} trigonal symmetry these states are further split by the trigonal crystal field into levels γ_4^+ and $\gamma_5^+ + \gamma_6^+$ described by the irreps of the trigonal double group. In the case of the C_{3v} symmetry, which lacks inversion symmetry, these levels have no parity. The γ_5^+ and γ_6^+ irreps are complex conjugates and degenerate in the absence of a magnetic field and are henceforth referred to as $\gamma_{5,6}^+$. Each Γ_8^+ quartet gives rise to the γ_4^+ and $\gamma_{5,6}^+$ states while the Γ_6^+ and Γ_7^+ each becomes a γ_4^+ state.

All these trigonal crystal field states are Kramers doublets and the application of a magnetic field will remove this degeneracy. Zeeman investigation on cobalt ions in the D_{3d} sites of $CsMgCl_3$ and the C_{3v} sites of $CsCdCl_3$ (Sec.4.4) has been carried out in this work. The magnetic field reduces these D_{3d} and C_{3v} symmetries with the resulting symmetries being dependent on its orientation with respect to the crystal axes. A field directed along the c axis will lower these symmetries to C_{3i} and C_3 respectively. In the case of a field applied perpendicular to the c axis, different symmetries result depending whether or not it is directed along a twofold axis. (The Co(2) ion site symmetry in $CsCdCl_3$ is approximately D_{3d} (Sec.2.1) and a pseudo twofold axis is implied for the case of this ion.) For the field along such an axis the D_{3d} and C_{3v} site symmetries of the cobalt ions reduce to C_{2h} and C_2, and for arbitrary orientations the respective symmetries are C_i and C_1.

The Zeeman levels can be labelled by the irreps of the appropriate point groups and can be derived by use of Koster's compatibility tables[8]. Fig. 2-3 shows the energy level scheme of the cobalt ion for the successive application of the various interactions of equations (2.1) and (2.3). The assignment for the Zeeman levels shown in the figure is purely schematic.

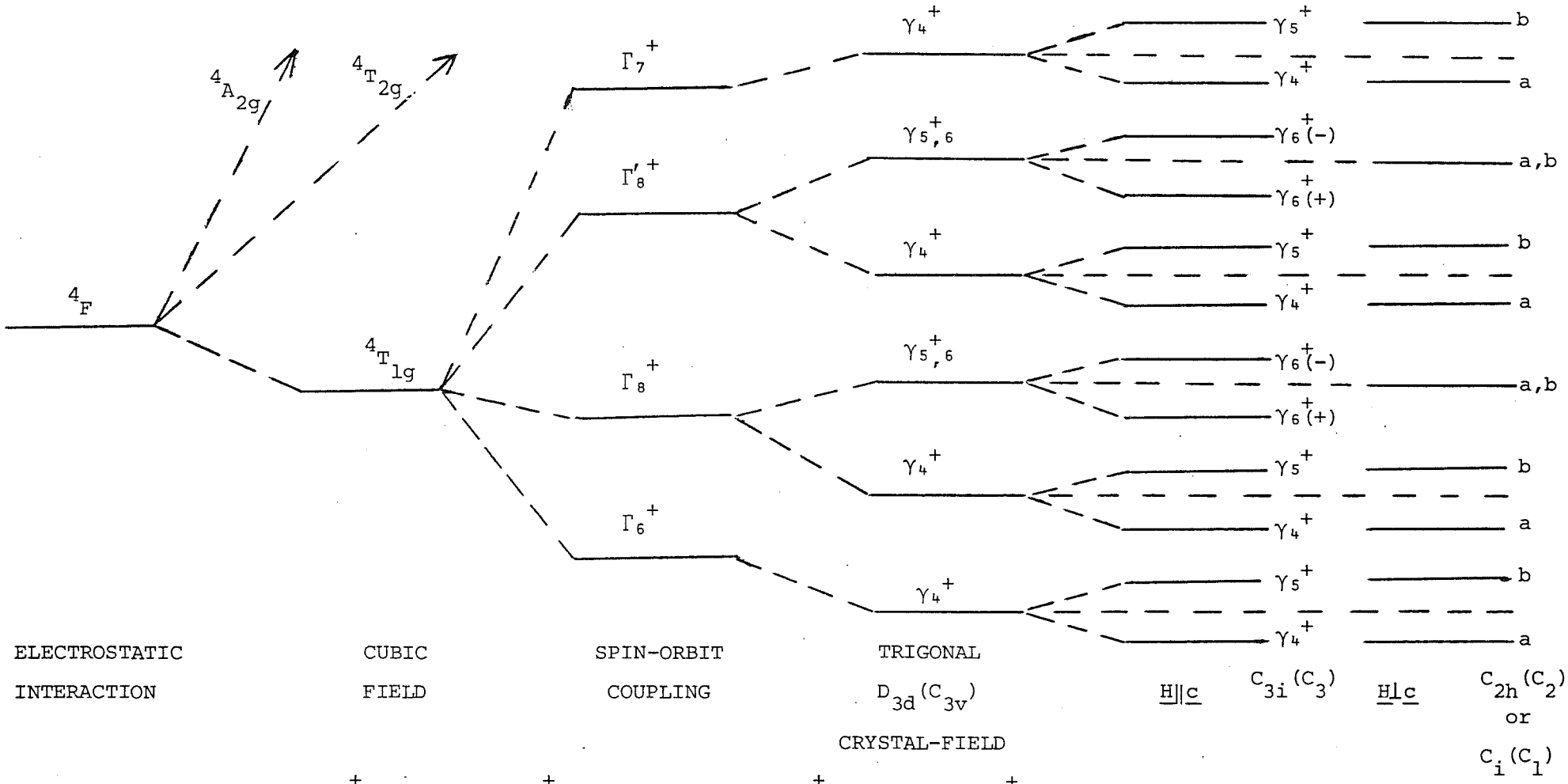

$a = \gamma_3^+ \; C_{2h}(C_2)$ or $\gamma_2^+(+) \; C_i(C_1)$ $\quad b = \gamma_4^+ \; C_{2h}(C_2)$ or $\gamma_2^+(-) \; C_i(C_1)$

The states labelled by symmetry groups without inversion symmetry have no parity labels.

Fig. 2-3: Schematic energy-level diagram of the Co^{2+} ion.

Transitions between these levels can occur in several ways, e.g., by infrared absorption and Raman scattering. The x,y and z components of the electric dipole and magnetic dipole operators for absorption of infrared radiation transform like the displacement vector $\underline{r}(r_i = x,y,z)$ and the rotation operator respectively. The symmetric Raman polarizability tensor $\alpha_{ij}(i,j = x,y,z)$ transforms like the $\underline{r}_i \cdot \underline{r}_j (r_i r_j = xy,xz,yz,x^2,y^2,z^2)$ operator. These operators transform as particular irreps of the appropriate cobalt ion site symmetry. Infrared absorption corresponding to a transition between an initial state i and a final state f is allowed if the direct product $\Gamma_o \times \Gamma_i$ contains Γ_f. Here Γ_i, Γ_f and Γ_o are respectively the irreps of the initial and final states and either the electric dipole or magnetic dipole operator in the appropriate symmetries.

A transition from the state i to the state f can give rise to a Raman line in the (ij) polarization spectrum (Sec.4.1) if Γ_f occurs in the reduction of $\Gamma_o \times \Gamma_i$ where Γ_o is the irrep of α_{ij}.

2.2.2. The Hamiltonian interaction terms and their associated parameters.

For an analysis of the Raman and infrared data, the strong-field energy matrices calculated by Johnstone[9] for the case of Co^{2+} ions in $CdCl_2$-type crystals were used. In this coupling scheme, the cubic field which is first considered, splits the d orbitals into e_g and t_{2g} orbitals. The seven d electrons are placed into these orbitals to give rise to configurations $t_{2g}^p e_g^q$ where $p + q = 7$. The energy levels for a $3d^7$ configuration are complementary to those for a $3d^3$ configuration because of the equivalence of three electrons with three holes in a d^n configuration. In these two configurations, the crystal field and spin-orbit interactions have opposite signs.

The interelectronic repulsion term of equation (2.1) will split the $3d^3(3d^7)$ configuration into a number of terms labelled by the cubic field irreps χ_r. Such terms, designated by $^{2s+1}\chi_r$ arise from the four

possible configurations $t_{eg}^{m} e_{g}^{n} (m + n = 3)$ for the $3d^3$ configuration. The effects of spin-orbit coupling and the trigonal crystal field are then calculated for these terms. The final wavefunctions maybe written as

$$|t_{2g}^{m} e_{g}^{n}, \alpha, {}^{2s+1}\chi_r, \Gamma_i^{+}, \gamma_t^{+}, \ell\rangle$$

where ℓ identifies the basis functions of the trigonal double group and α is an additional label to distinguish wavefunctions when there is more than one with the same group theoretical labels in any configuration. Here α is taken as the irrep of states of the parent $t_{2g}^{m} e_{g}^{n-1}$ configuration.

All the matrix elements of the cubic field potential for these strong-field wavefunctions are necessarily diagonal and can be expressed in terms of the single parameter Dq as follows

$$\langle t_{2g}^{m} e_{g}^{n} | V_c | t_{2g}^{m} e_{g}^{n} \rangle = n\ 10\ Dq \quad . \tag{2.5}$$

The energy matrices of the electrostatic and spin-orbit interactions have been calculated in the strong-field scheme for the $3d^3$ configuration by Sugano[10] and Schroeder[11] respectively. The electrostatic interaction has non-zero matrix elements only between levels belonging to the same ${}^{2s+1}\chi_r$ terms and can be expressed in terms of two Racah parameters B and C. The spin-orbit interaction $V(1T_1)$ is characterized by two parameters ζ and ζ' defined in terms of the one-electron reduced matrix elements of $V(1T_1)$ as follows:

$$\begin{aligned} 3i\zeta &= \langle t_2 || V(1T_1) || t_2 \rangle \\ -3\sqrt{2}i\zeta' &= \langle t_2 || V(1T_1) || e \rangle \quad . \end{aligned} \tag{2.6}$$

The trigonal field matrices have been calculated by Johnstone and Zdansky[9] using the strong-field approach. With the trigonal (z) axis directed along the [111] direction of the crystal the potential due to a field of D_{3d} symmetry can be expressed by[12]

$$V_T = A_2\{xy + yz + xz\} + A_4\{yz(r^2 - 7x^2) + xz(r^2 - 7y^2) + xy(r^2 - 7z^2)\} \quad . \tag{2.7}$$

The above crystal field transforms as the cubic representation T_2 and has one-electron matrix elements which are nonvanishing only between two t_{2g} and between the t_{2g} and e_g orbitals. The trigonal field can be expressed in terms of the one-electron reduced matrix elements as follows:

$$V = \frac{1}{\sqrt{2}} \langle t_2 || V(T_2) || t_2 \rangle \tag{2.8}$$

$$V' = \frac{1}{\sqrt{6}} \langle t_2 || V(T_2) || e \rangle \quad .$$

The effect of a magnetic field on the cobalt ion levels can be evaluated from the matrix elements of the Zeeman operator $k\underline{L} + 2\underline{S}$ between the strong-field wavefunctions, where k is an orbital reduction factor. This operator transforms as the cubic T_1 representation of the octahedral group and its matrix elements are characterized by two orbital reduction parameters K and K′ defined as

$$\begin{aligned} \sqrt{6}\, i\, K &= \langle t_2 || \mathcal{H}_z(T_1) || t_2 \rangle \\ -2\sqrt{3}\, i\, K' &= \langle t_2 || \mathcal{H}_z(T_1) || e \rangle \end{aligned} \tag{2.9}$$

where $\langle t_2 || \mathcal{H}_z(T_1) || t_2 \rangle$ and $\langle t_2 || \mathcal{H}_z(T_1) || e \rangle$ are the one-electron reduced matrix elements of the Zeeman interaction $\mathcal{H}_z(T_1)$. These parameters are related to the spin-orbit parameters ζ and ζ' by

$$K = \zeta/\zeta_o \quad \text{and} \quad K' = \zeta'/\zeta_o \tag{2.10}$$

where ζ_o is the free-ion spin-orbit coupling parameter.

CHAPTER III

EXPERIMENTAL TECHNIQUES

3.1 THE CRYSTALS

3.1.1 Crystal Growth

All crystals examined were prepared from high-quality anhydrous powders. These powders were dehydrated in a vacuum oven, maintained at 100°C, over a period of several days.

Single crystals were grown from the melt using the well established technique described by Rollerson[13]. In this the starting material, placed in a quartz tube, is purified by gradual heating of the charge to 50°C above its melting point under a stream of dry hydrogen-chloride or -bromide gas as appropriate. This removes traces of hydroxides and moisture. An ampoule is then lowered through a Bridgman tubular furnace with a temperature gradient of 50°C per cm. The lowering rate for most cases is 1mm per hour except for $CsCoCl_3$ where it is 0.5mm per hour.

Not all of the crystals were refined using commercially available hydrogen chloride gas from cylinders. $KCdCl_3$ grew better from powders purified by hydrogen chloride gas generated by the action of concentrated sulphuric acid on concentrated hydrochloric acid. Phosgene gas was used to purify $CsCoCl_3$ and some of the $CsCdCl_3$ starting materials as suggested by Trutia and Lebl[14]. Any poisonous phosgene gas in excess of the safety level could be detected by a change in colour from yellow to deep orange of the phosgene indicator papers used. These were prepared by soaking filter papers in an alcoholic solution containing 10% mixture of equal parts of p-dimethyl aminobenzaldehyde and diphenylamine and then dried[15].

Crystal boules of $CsCdCl_3$, $CsMgCl_3$ and $KCdCl_3$ obtained in this

manner are optically clear while $CsCoCl_3$ has a green blue colour. Cobalt-doped crystals grown are blue and transparent. The $CsCdCl_3$:Co crystals show an appreciable concentration gradient with the portions of the crystals nearest the tapered tip having the least cobalt ion concentration. Attempts to determine the cobalt concentration of these crystals by spectrophotometric means were thwarted by their insolubility in pure and acidified water. The $KCdCl_3$:Co crystals suffer from cracks. The Fe^{2+} doped $CdCl_2$ and $CdBr_2$ crystals appear brownish.

3.1.2 Orientation and polishing of crystal specimens.

Except for $CsCdCl_3$ all the crystals examined were hygroscopic and were stored and handled in a glove-box maintained at 15% humidity.

$CsCdCl_3$ exhibits no cleavage and the direction of its crystallographic axis was determined with the aid of a polarizing microscope. The microscope's objective lens of magnification 40X was used in conjunction with an ocular of magnification 10X. Orientation of $CsCdCl_3$ was done as follows. A chunk of crystal, placed on the microscope stage, was rotated until an isogyre cross[16] appeared within the field of view. The final alignment was achieved when the centre of the isogyre cross did not shift from the centre of the cross hairs during rotation of the stage. The crystal axis was then parallel to the axis of the microscope. The specimen was then ground to required size and thickness with silicon carbide powder. A final polish using a tin oxide-methanol paste on a rotating baize-covered lap gave a high-lustre finish.

The $\underline{c}$ axes of $CsMgCl_3$ and $CsCoCl_3$ lie in their $[11\bar{2}0]$ cleavage planes. This greatly facilitates polarization infrared experiments. However for axial infrared and Zeeman-Raman ($\underline{H} \| \underline{c}$) experiments, the direction of the $\underline{c}$ axis had to be located. The required direction

is parallel to the intersection of any two cleavage planes. This fact however cannot be utilized for small crystals. Alternatively the Beckman spectrophotometer (Sec. 3.3.1) can be employed in locating the crystal axis. This was done by rotating a polarizer until the π or σ spectrum of a cleaved sample was obtained and then noting the corresponding orientations of both the polarizer and the sample. For the π and σ spectra the c axis is respectively parallel and perpendicular to the polarizer's axis.

$CdBr_2$ and $CdCl_2$ cleave along planes perpendicular to their c axes. These crystals together with $CsMgCl_3$ and $CsCoCl_3$ were polished in the glove-box using emery paper. The procedure which involved mounting of the crystals onto a polishing-jig is described in detail by Johnstone[9].

Of all the crystals studied, $KCdCl_3$ proved to be the most difficult to orientate as it is hygroscopic and has no obvious cleavage planes. Determination of its c axis with a polarizing microscope was not feasible as the microscope could not fit into the glove-box. Hence no polarization studies of this crystal was attempted.

3.2 RAMAN MEASUREMENTS

3.2.1 Conventional Raman

A Spectra-Physics model 171 15-watt argon-ion laser served as the excitation source in the Raman scattering experiments. The laser has its light stabilized to an intensity fluctuation of less than 0.5%. Apart from the laser, the Raman system used is that set up by Lockwood[17] and Christie[18]. A Jarrell-Ash model 25-103 one-metre double monochromator is used to disperse the scattered light and the spectrometer output is detected by an EMI 6255 SA photomultiplier which is thermoelectrically cooled to $-25^{\circ}C$. Photon counting techniques

are used and the output pulses from the photomultiplier are amplified and height-discriminated by a pulse rate detector. A ratemeter then time-averages the resultant pulses to give a d.c. voltage proportional to the pulse rate received which is then displayed on a chart recorder.

The principal laser lines used were the 4765, 4880 and 5145 Å lines, the maximum power outputs of which are 3, 7 and 6W respectively. However power outputs of up to only 3W were required. Narrow band-interference filters were placed in the incident beam path to remove spurious plasma lines which are listed by Loader[19].

For polarization studies, a Spectra-Physics model 310 polarization rotator was attached to the front of the laser. The rotator can alter the plane of polarization of the incident beam to any desired angle. The scattered radiation was analysed using either a polaroid sheet or a Nicol prism. The latter has slightly better polarizing qualities while the former does not defocus the beam as much.

Spectra were recorded using the conventional right-angled scattering geometry in which the laser light is incident on the bottom face of the crystal and scattered light at 90^{o} to this is collected from a vertical surface by the spectrometer optics. This arrangement however proved to be unsuitable for highly absorbing crystals such as $CsCoCl_3$. For these crystals the surface scattering technique provided an alternative method. In this method the laser light is incident on one face of the crystal at grazing angle while the scattered radiation off the same face is still observed at 90^{o} to the incident beam.

Raman measurements at cryogenic temperatures were carried out with an Andonian optical dewar. The dewar body comprises an inner liquid helium reservoir, an outer liquid nitrogen jacket and a heat exchange space. Depending on the temperature required, the inner reservoir could either be filled with liquid-nitrogen or -helium. When the latter was used, the outer jacket was filled with liquid

nitrogen. The exchange space was then pressurized with nitrogen or helium gas as appropriate. At one atmospheric pressure these gases condensed to liquid at the bottom of the exchange space. Crystals were mounted onto a copper block attached to the bottom of this exchange space and were cooled by the condensed gas through thermal contact. A copper-constantan thermocouple attached to the copper block recorded a temperature of $15^{o}K$ when liquid helium was used. Owing to heating by the laser beam the crystal temperature was as high as $25^{o}K$.

Two different sample holders were made for the two scattering arrangements. For the conventional 90^{o} geometry, the sample holder used had a vertical face against which the crystals are clamped. Crystals used in this arrangement are required to have one horizontal and two parallel vertical faces. The sample was mounted with the bottom horizontal face receiving the laser beam, and one of the vertical faces facing the spectrometer's collection optics. These faces were either cleaved or polished as appropriate for the crystals studied.

A sample holder with a face inclined at 30^{o} was used in the surface scattering technique. Specimens attached onto this face were examined with the laser beam incident from below on a crystal surface and the light scattered horizontally off the same surface was analysed.

3.2.2 Zeeman-Raman

Zeeman-Raman measurements were obtained using a British Oxygen Company (B.O.C.) 6-tesla split-solenoid superconducting magnet. The field homogeneity is better than 1% over a 15mm diameter spherical volume. The solenoid is mounted with its bore horizontal and four slots in its equatorial plane gave both vertical and horizontal access to its centre. These slots permitted the use of the 90^{o} scattering

geometry. The magnet was used in conjunction with a B.O.C. cryostat which has a liquid air vessel surrounding its inner helium reservoir (Fig.3-1). This cryostat together with the rest of the Raman system is pictorially depicted in Fig.3-2. The reservoir has sapphire windows and the outer vessel quartz windows. The solenoid, held by three support rods, was positioned so that its ports faced one pair of windows while its vertical slots faced a second pair set at right angles to that of the first.

A stainless steel rod with several recesses cut along its lower portion served as the sample holder. Several specimens were each glued onto a recess using GE 7031 varnish. The sample rod passed through the solenoid's horizontal slots and the specimen of interest was positioned at the centre of the solenoid.

Overnight cooling of the magnet assembly and cryostat was necessary to ensure efficient use of liquid helium. It was found that gradual cooling of $CsMgCl_3$ and $CsCdCl_3$ crystals was essential to prevent them from cracking. So these were also cooled overnight. This was done by closing the container and pressurizing it with pure helium gas which served a twofold purpose. It acted as a heat conducting medium as well as preventing the hygroscopic crystals from moisture contamination.

Thirty litres of liquid helium were expended for a typical Zeeman experiment giving a spectral run of about five hours. Problems with bubbling of the liquid helium causing fluctuating light intensity were resolved by pumping the liquid helium to its superfluid state ($\sim 2^{o}K$). Once this was attained the magnet was energised using a B.O.C. model DPS 60/72A power supply.

A periscope-like arrangement of two prisms was needed to raise the horizontal laser beam to meet the specimen positioned at the centre of the magnet. The scattered radiation, which passed down the

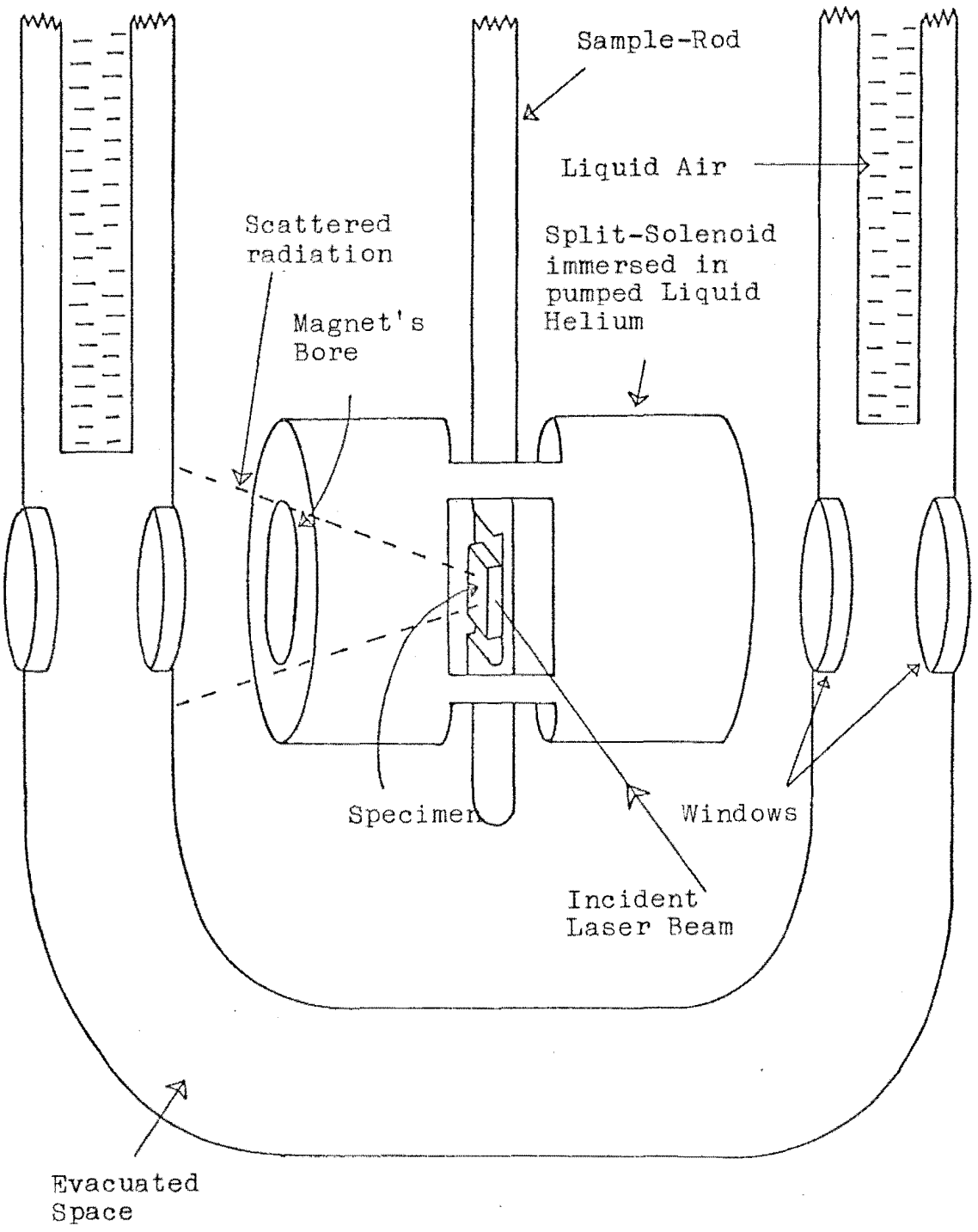

Fig. 3-1: Cross-section of the B.O.C. cryostat exposing the superconducting 6-tesla magnet.

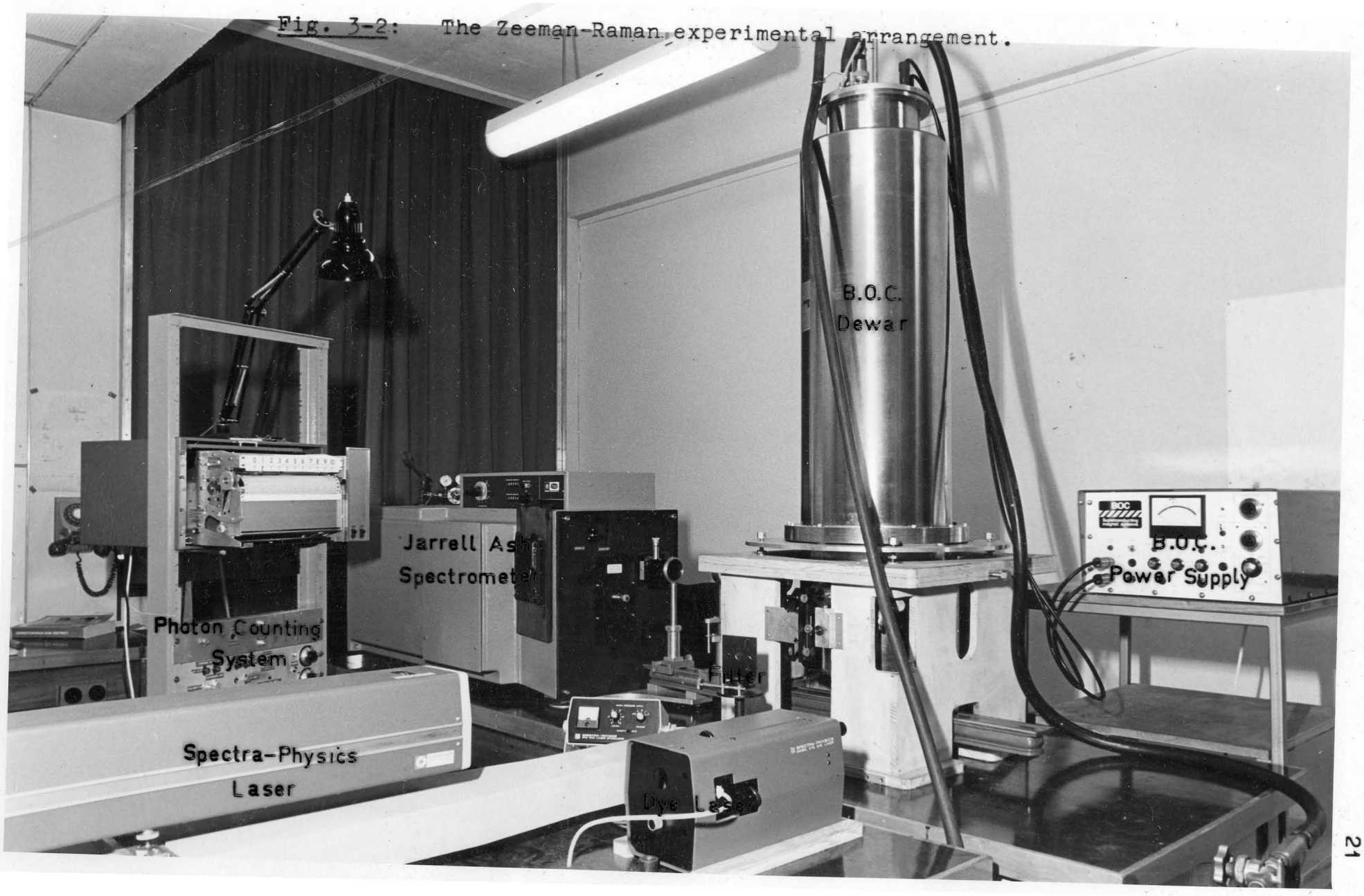

Fig. 3-2: The Zeeman-Raman experimental arrangement.

solenoid's bore, was focussed onto the spectrometer slit by a suitable lens system.

Whereas the slit is vertical, the brightest portion of the specimen's image is horizontal due to the horizontal illumination. Owing to this and the small size of the solenoid's windows and the need for the radiation to pass through a total of four windows and two prisms, the signal-to-noise ratio achieved in this Zeeman arrangement was a factor of 15 inferior to the conventional arrangement.

3.3 INFRARED MEASUREMENTS

3.3.1 Conventional Infrared

Infrared studies were performed using a Beckman IR12 spectrophotometer with a frequency range of 200 - 4000 cm^{-1}. A Nernst glower acts as the infrared source and the detector is an evacuated thermocouple. The instrument has a maximum resolution of 0.25 cm^{-1} at 923 cm^{-1}. It was continuously purged with dry air to minimise absorption bands due to atmospheric water vapour. As the sizes of the crystals studied were much smaller than the optical beam's cross-sectional dimensions, a Beckman 46286 beam condenser was employed. By reducing the cross-sectional size of the beam incident on the specimen to 1 x 5mm, a high intensity of light transmission could be obtained. Polarization studies were performed with a Beckman 24473 silver chloride polarizer.

Crystals were mounted onto a copper sample holder attached to the tip of the inner can of a conventional cold-finger dewar. For low temperature studies, the inner can was filled with the required refrigerant. Good thermal contact was achieved by having an indium foil sandwiched between the sample and its holder. The lowest temperature attained was estimated at 15^{o}K. Transmission down to 300 cm^{-1} was ensured by the use of cesium bromide windows.

3.3.2 Zeeman-Infrared

The field for the Zeeman-infrared experiments was generated by a 4-tesla Oxford Instrument solenoidal superconducting magnet. Fig. 3-3 shows the magnet assembly which is housed in a stainless steel dewar constructed in the department. The actual magnet itself is situated near the bottom of the helium reservoir which has a capacity of five litres. An 8-litre liquid air jacket surrounds the upper half of the helium can. The lower portion of the can is surrounded by a copper radiation shield which is in contact with the liquid air jacket. Along the bore of the magnet is a tight-fitting stainless steel tube whose ends are soldered onto the walls of the helium can. A copper ring, brazed onto the central portion of the inside of this tube, acts as a sample-holder mount.

Preparation for a Zeeman experiment was done in the following manner. The specimen was clamped onto a detachable copper sample-holder which was then screwed into the copper ring using a tubular key. The cylindrical tail-piece, equipped with two cesium bromide windows, was then screwed onto the bottom flange of the dewar. After evacuating the dewar to below 30μ Hg, the outer jacket was filled with liquid air. Liquid helium was transferred from a storage can to the reservoir via a transfer tube. Cooling of the crystal was by thermal contact through the stainless steel tube and the sample-holder. Three Allen Bradley resistors each located at the top, centre and bottom of a stainless steel tube, inserted in the reservoir, acted as liquid helium level indicators. The bottom of this tube rested on top of the magnet. A B.O.C. PS 60/72 A power supply was employed to energise the magnet which was operated in the persistent current mode. The field was homogeneous to 1% over a 1cm diameter spherical volume.

Owing to the size of the magnet the dewar's tail-piece occupied most of the sample compartment of the Beckman instrument. This meant

Fig. 3-3: Zeeman-infrared superconducting magnet dewar.

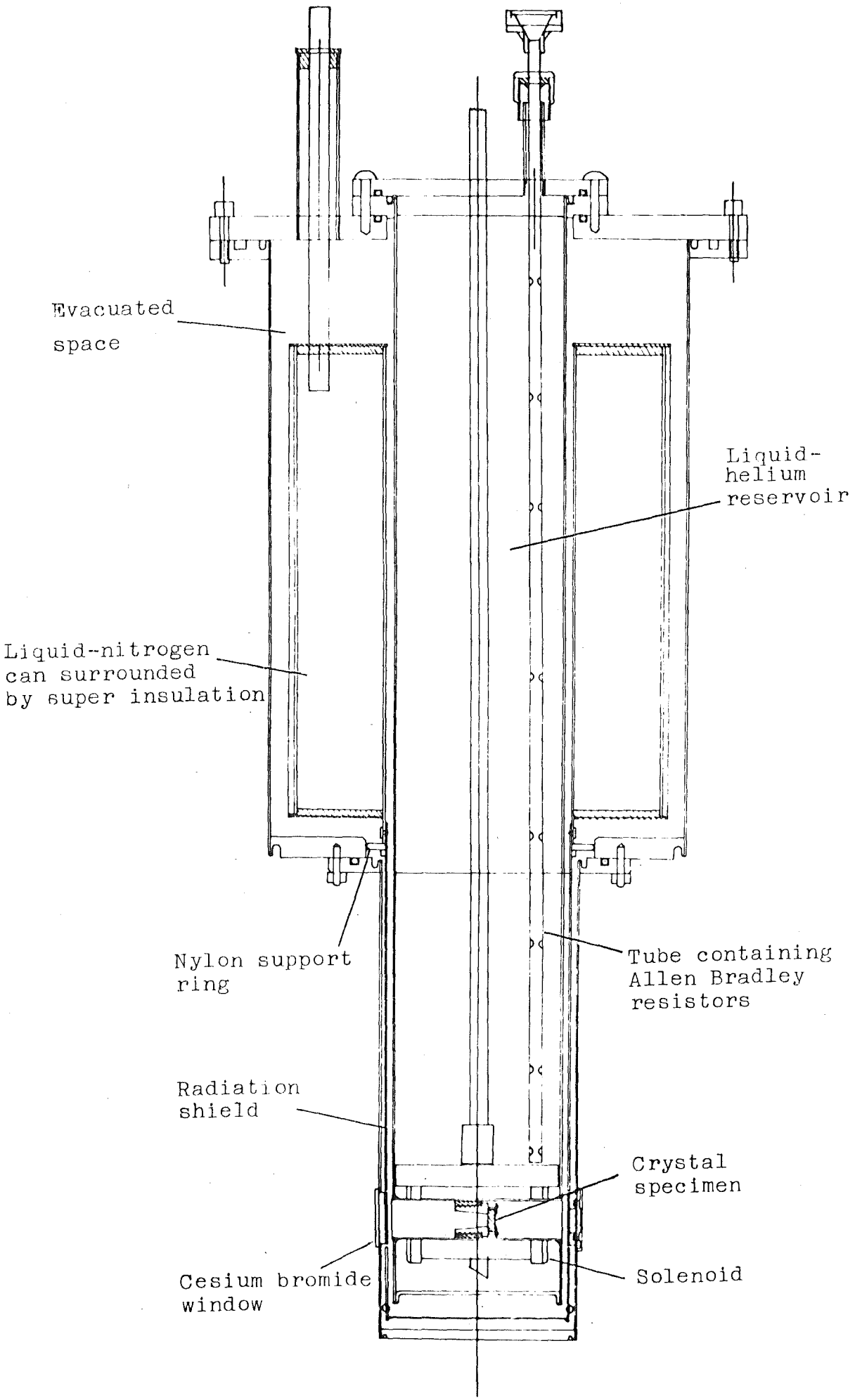

that the Beckman beam condenser could not be used for the Zeeman-infrared scans. Omission of the beam condenser resulted in an intensity loss of 50%. To compensate for this, wider slit widths and higher signal gains were needed.

Unlike the 6-tesla Raman magnet, the 4-tesla one is not of the split-solenoid type. Because of this limitation, Zeeman-infrared measurements could only be done with the field directed along the radiation beam.

3.4 OPTICAL MEASUREMENTS

Optical absorption spectra were recorded with a model 1700, 75cm focal length f6.8 Czerny Turner spectrometer manufactured by Spex Industries Inc. The spectrometer is capable of a 0.1Å resolution. Crystals were mounted in the same Andonian dewar as that used in the Raman experiments. Light from a 100 W quartz-iodine lamp was focussed on the sample, the transmitted radiation in turn being focussed on the slit of the spectrometer. The resulting output from an E.M.I. type 9558 QB photomultiplier tube was amplified and displayed by a chart recorder.

CHAPTER IV

RAMAN SCATTERING STUDIES

4.1 INTRODUCTION

Since its discovery the Raman effect has been a useful technique for studying vibrational and rotational transitions in molecules and solids. However thirty-five years were to elapse before the first electronic Raman effect in solids was reported[20]. Like ordinary lattice Raman scattering, electronic Raman scattering is a weak process and hence requires a powerful exciting source. Research in this field is greatly facilitated by the laser which had its advent in 1960.

Raman scattering is a two-photon process and is therefore weaker than optical absorption which involves only one photon. Despite this, Raman scattering has several advantages. First the Raman operator has even parity whereas the electric dipole operator for optical absorption is odd. Intraconfigurational transitions connect states of the same parity and as such are allowed by Raman scattering while forbidden in electric dipole processes. This allows direct observation of electronic transitions by Raman scattering, while in electric dipole absorptions, the spectra are plagued by electric dipole allowed vibronic sidebands. A second advantage is that Raman scattering involves optical wavelengths while optical absorptions due to low-lying electronic levels are in the infrared where vibrational absorptions of the host crystal frequently obscure electronic absorptions. Thirdly the laser radiation is monochromatic, collimated and polarized. This allows ready determination of the polarization properties of Raman transitions.

The notation shown on the Raman spectra such as a(ij)b is that adopted by Damen et.al.[21], where a and b indicate the directions of incident and scattered photons and i and j are their respective directions of electric vectors. (a,b,i,j = X,Y,Z and the convention

that the c axis be chosen as the cartesian Z axis is followed). Right-angled scattering of uniaxial crystals gives rise to nine possible polarization configurations viz., (XX),(XY),(XZ),(YX),(YY),(YZ),(ZX),(ZY) and (ZZ).

The Raman work done in this thesis comprises two parts, the first of which involves conventional Raman spectroscopy and served as a preliminary to the Zeeman-Raman work. The zero-field and Zeeman investigations are described in Chapters IV and V respectively.

In this work the Raman scattering from single crystals of $CsCoCl_3$ and cobalt-doped crystals of $CsMgCl_3$, $CsCdCl_3$ and $KCdCl_3$ were investigated. The experimental results of scattering by both phonons and Co^{2+} ions in these crystals are presented. The electronic transitions of interest are between the levels of the $^4T_{1g}(^4F)$ cubic field ground term of the Co^{2+} ion.

Sec. 4.2 gives a general description of the recorded spectra while spectra for each crystal are singly discussed in Sec. 4.3. The principal part of this work is centred on the $CsMgCl_3$ and $CsCdCl_3$ systems.

Kardontchik et.al.[22], have reported the polarized Raman spectra of Co^{2+} ion impurities in $CsMgCl_3$. They observed three of the five transitions between the low-lying electronic levels. Their observations are confirmed and extended to include the detection of the two remaining electronic transitions.

Raman scattering results on $CsCdCl_3$:Co, $KCdCl_3$:Co and $CsCoCl_3$ are original and are presented for the first time. An in-depth study of the scattering from $CsCdCl_3$:Co was done. As described in Sec.2.1, the Co^{2+} ions in $CsCdCl_3$ occupy two non-equivalent cation sites. One would therefore expect two sets of electronic lines. However as will be shown the spectra observed are principally due to Co^{2+} ions in the C_{3v} sites thus simplifying the interpretation of these spectra. Only three transitions to the highest levels were observed for the Co^{2+} ions

in these C_{3v} sites. Polarization studies were carried out to establish the group symmetry of these electronic lines.

Once the observed transitions had been assigned the Raman work was extended to cover the effects of an external magnetic field on these transitions. Both the $CsMgCl_3$:Co and $CsCdCl_3$:Co systems were investigated by Zeeman-Raman studies which are described in the following chapter.

4.2 GENERAL

An argon-ion laser provides an ideal excitation source for the blue cobalt-doped double chloride crystals studied in this work. The 4765 and 4880Å radiation give optimum electronic Raman scattering for these crystals while the 5145Å radiation was found to be less satisfactory. This is because these crystals absorbed the latter line much more and its frequency is well removed from any electronic level of Co^{2+} ion that could give resonant enhancement. Moreover the scattering efficiency is proportional to the fourth power of the excitation frequency. Raman spectra were recorded at liquid-nitrogen and -helium temperatures from the excitation frequency up to a Stokes shift of 1500 cm^{-1}.

Intense sharp lines are a characteristic feature of the spectra in the region from 0 to 300 cm^{-1}. These are due to the first-order scattering by phonons of the crystals. Second-order phonon scattering lines were observed for the Raman scattering of $CsCdCl_3$. They are weaker than the first-order scattering and for the case of $CsCdCl_3$ have energies above 300 cm^{-1}. For Co^{2+} doped crystals, the high energy portions of their spectra beyond 800 cm^{-1}, exhibit lines that are weaker and broader than the first-order phonon scattering and with intensities linearly dependent on the cobalt ion concentrations. Scattering from corresponding crystals doped with $FeCl_2$ do not reproduce these lines.

These lines are attributed to the highest three electronic transitions of the Co^{2+} ion within the $^4T_{1g}(^4F)$ cubic field manifold.

Raman lines due to the lowest two electronic transitions occur among those of the first- and second-order phonon scattering. As these lines are relatively weak they can be masked by the more intense phonon lines as was found for the case of $CdCl_2$:Co by Christie et.al.[29]. The electronic lines can be differentiated from the phonon lines by a comparison with spectra of corresponding Fe^{2+} doped crystals. The transition to the $\gamma_4^+(\Gamma_8^+)$ state of $CsMgCl_3$:Co was identified in this manner.

Fluorescence lines were encountered only in the scattering from $CsMgCl_3$:Co. Unlike Raman lines, fluorescence lines have the same absolute frequencies irrespective of the excitation frequency.

For $CsMgCl_3$:Co and $CsCdCl_3$:Co, the strongest two electronic lines are those due to transitions from the $\gamma_4^+(\Gamma_6^+)$ ground state to the $\gamma_4^+(\Gamma_8'^+)$ and $\gamma_{5,6}^+(\Gamma_8'^+)$ upper levels. As shown by Christie[18] the scattering efficiency of the $\gamma_4^+ \rightarrow \gamma_{5,6}^+$ transition is zero in the (ZZ) polarization. This has been verified for the case of $CsMgCl_3$:Co by Kardotchik et.al.[22]. Kiel and Porto[23] have shown that the polarization selection rules are identical for the D_{3d} and C_{3v} symmetries. Hence the $\gamma_4 \rightarrow \gamma_{5,6}$ transition of the Co^{2+} ions in the C_{3v} sites of $CsCdCl_3$ should also be absent in the (ZZ) polarization. In Sec.4.3 a comparison of the (ZZ) and (ZY) spectral intensities was made to distinguish the $\gamma_4(\Gamma_8')$ and $\gamma_{5,6}(\Gamma_8')$ lines of these Co^{2+} ions. The identification of the observed electronic lines by polarization was borne out by the electronic Zeeman-Raman studies described in the following chapter.

4.3 RESULTS

4.3.1 $CsCdCl_3$:Co

Raman studies of pure and Co^{2+} doped $CsCdCl_3$ crystals were made at liquid nitrogen and liquid helium temperatures. The nominal $CsCoCl_3$ impurity content ranged from 5 to 10 mole %.

Pure $CsCdCl_3$ crystals cooled to 80 and 15^{o}K were investigated by Raman scattering using the 4765, 4880 and 5145Å radiation. These proved to be equally efficient for the colourless crystals. A set of the 15^{o}K spectra of six independent polarization configurations of a $CsCdCl_3$ crystal is displayed in Fig. 4-1. Table 4-1 lists the frequencies and line widths of the lines detected. Transitions were observed within the 40-250 and 300-650 cm^{-1} regions. The former region contains ten lines of varying intensities, the strongest of which is at 248.7 cm^{-1}. Some of the weaker lines are absent in certain polarization configurations. The relative intensities of the 115.2 and 127.7 cm^{-1} lines in (ZZ) contrasts sharply with that of the other polarizations in that the former line is stronger than the latter only in (ZZ). This fact was utilized as a check on the crystal orientation for the many (ZZ) polarized spectral runs done.

Bands lying in the next region are generally weaker and broader than the lower-energy lines. A total of six of these bands were recorded, with the band shifted by 602 cm^{-1} and having a line width of 35 cm^{-1} being the broadest. For a comparison of intensities, they are shown together with the lower-energy lines in the randomly polarized spectrum of Fig. 4-2.

In the spectra of cobalt-doped crystals, four additional lines, whose frequencies are listed in Table 4-2, were observed. Figs. 4-3 and 4-4 show the four independent polarized components of the 15^{o}K $CsCdCl_3$:Co 5 mole % spectrum exhibiting these four lines which peak at 873, 897, 947 and 1070 cm^{-1}. The 873 and 947 cm^{-1} lines are the

Fig. 4-1: First-order Raman spectra of undoped $CsCdCl_3$ recorded at 15°K.

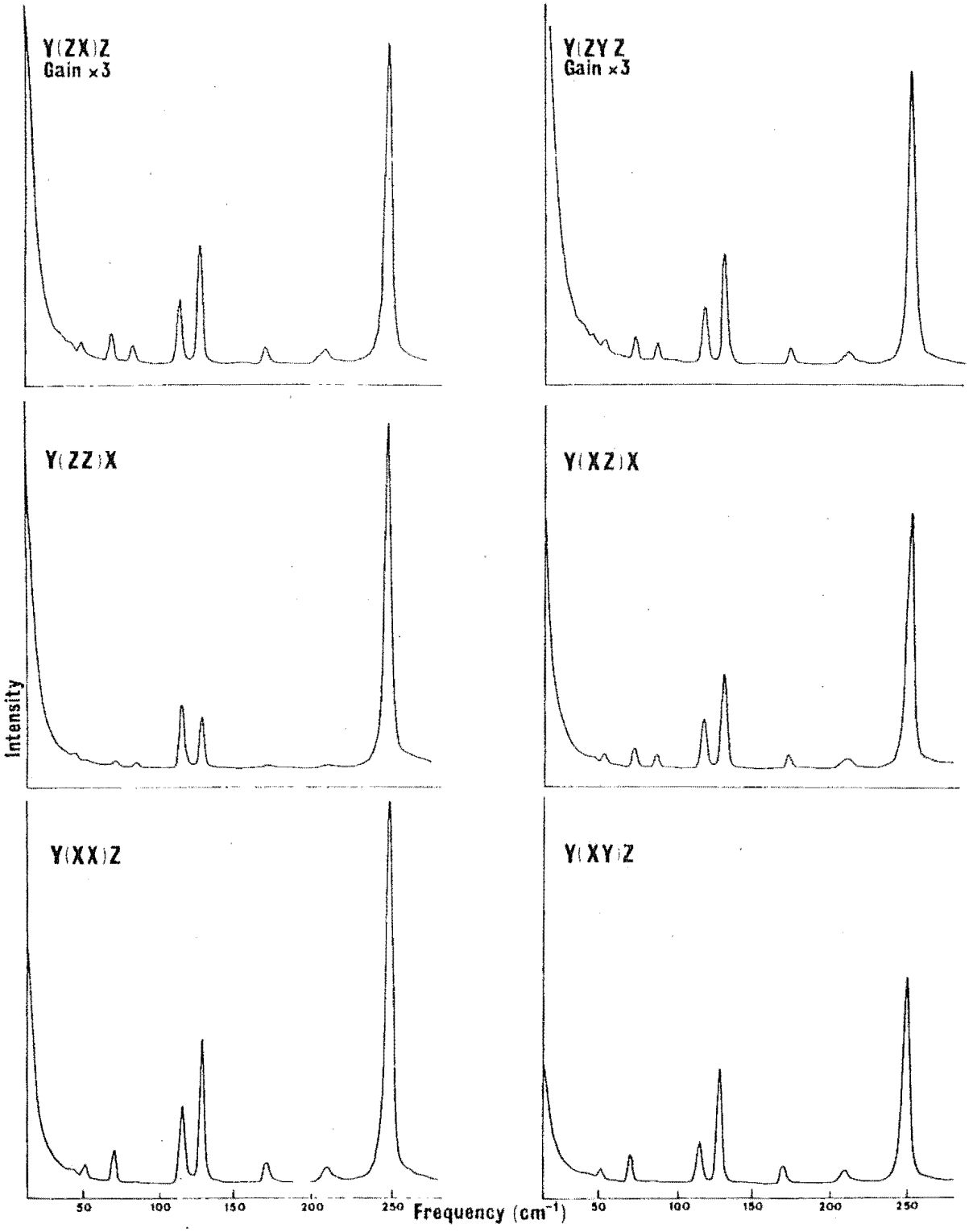

Fig. 4-2: Raman spectrum of undoped $CsCdCl_3$ recorded at $15^{o}K$.

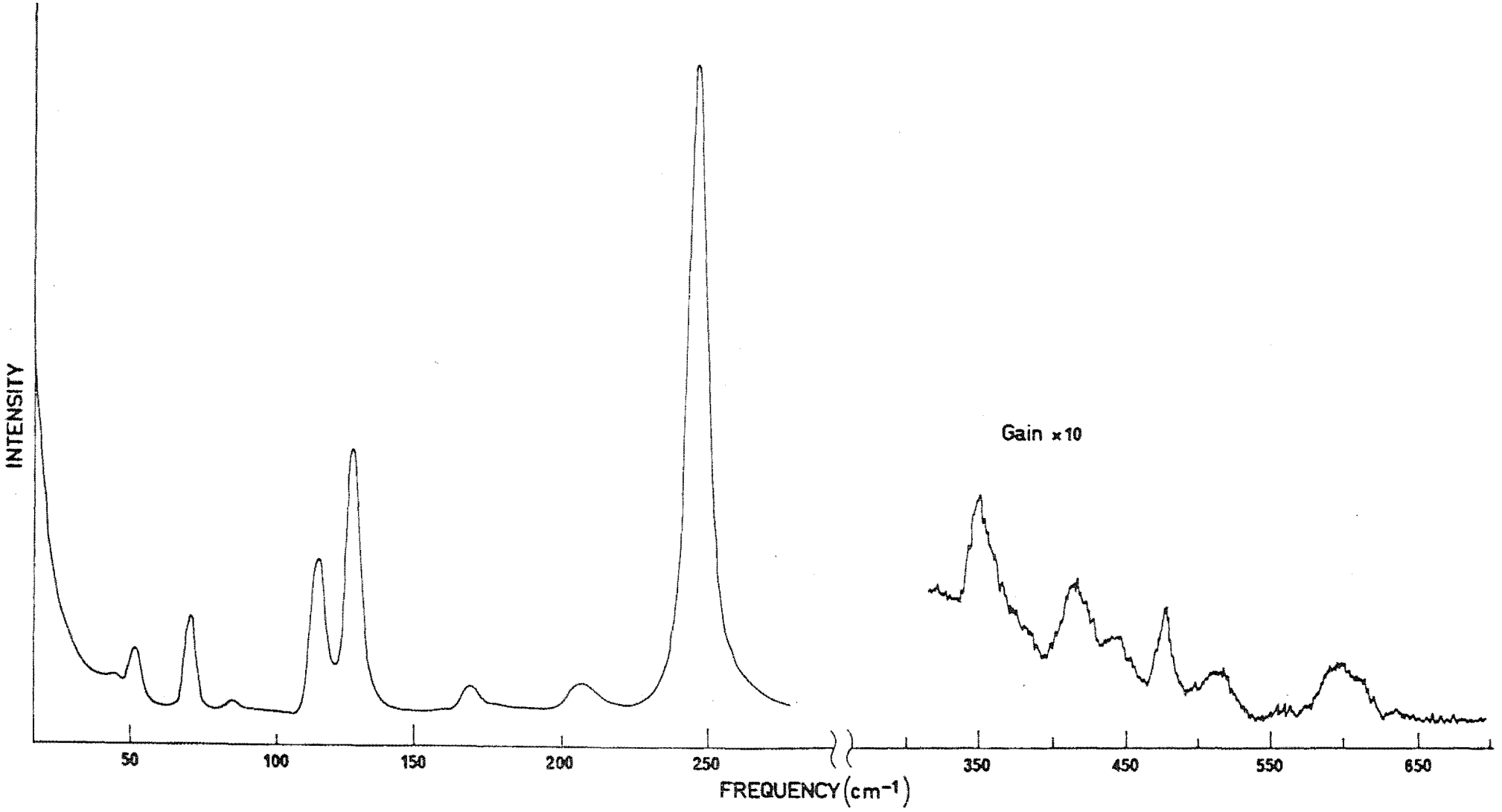

TABLE 4-1: Frequencies and linewidths of first and second order phonon scattering lines of $CsCdCl_3$ and $CsMgCl_3$ at 15°K. All measurements are in cm^{-1}.

$CsCdCl_3$

First order spectrum

Freq.	Width
46 ± 2	-
52 ± 1	-
71 ± 1	3
85 ± 1	4
115.2 ± 0.5	3.7
127.7 ± 0.5	3.8
156 ± 2	-
170 ± 1	4
208 ± 1	7
248 ± 0.5	5.0

Second order spectrum

Freq.	Width
351 ± 2	17
418 ± 2	22
447 ± 3	-
479 ± 2	15
510 ± 3	-
602 ± 4	35

$CsMgCl_3$

First order spectrum

Freq.	Width
55.5 ± 0.5	3
129.0 ± 0.5	4.5
190.0 ± 0.5	4.0
257.0 ± 0.5	5.0

TABLE 4-2: Experimental and computed[a] frequencies and assignments of the zero-field electronic levels of the $^4T_{1g}(^4F)$ ground term of the Co^{2+} ion. All measurements (in cm^{-1}) were taken at 15^oK.

Assignment[b]	$CsMgCl_3$:Co			$CsCdCl_3$:Co(2)		
	Frequency		Width	Frequency		Width
	Compt.	Expt.		Compt.	Expt.	
$\gamma_4^+(\Gamma_7^+)$	1378.1	1380±2	8	1070.0	1070±4	15
$\gamma_{5,6}^+(\Gamma_8'^+)$	1263.7	1264±1	7	946.1	947±1	8
$\gamma_4^+(\Gamma_8'^+)$	823.1	823±1	5	871.1	873±1	7
$\gamma_{5,6}^+(\Gamma_8^+)$	466.6	472±4	15	395.5	-	-
$\gamma_4^+(\Gamma_8^+)$	231.9	234±2	5	291.1	-	-
$\Gamma_8'^+$ of Co(1) in $CsCdCl_3$	-	-	-	-	897±2	7
Cobalt cluster line of $CsMgCl_3$	-	848±2	-	-	-	-

a: The frequencies were computed using the following parameters (in cm^{-1})

	Dq	B	C	ζ	V	V'
$CsMgCl_3$:Co	-678.0	790.0	3320.0	-498.8	130.6	545.3
$CsCdCl_3$:Co(2)	-674.0	790.0	3320.0	-522.5	327.4	-71.2

b: The assignments for the Co(2) ion for $CsCdCl_3$ have no parity labels.

Fig. 4-3: 15°K polarized Raman spectra of $CsCdCl_3$:Co 5 mole %

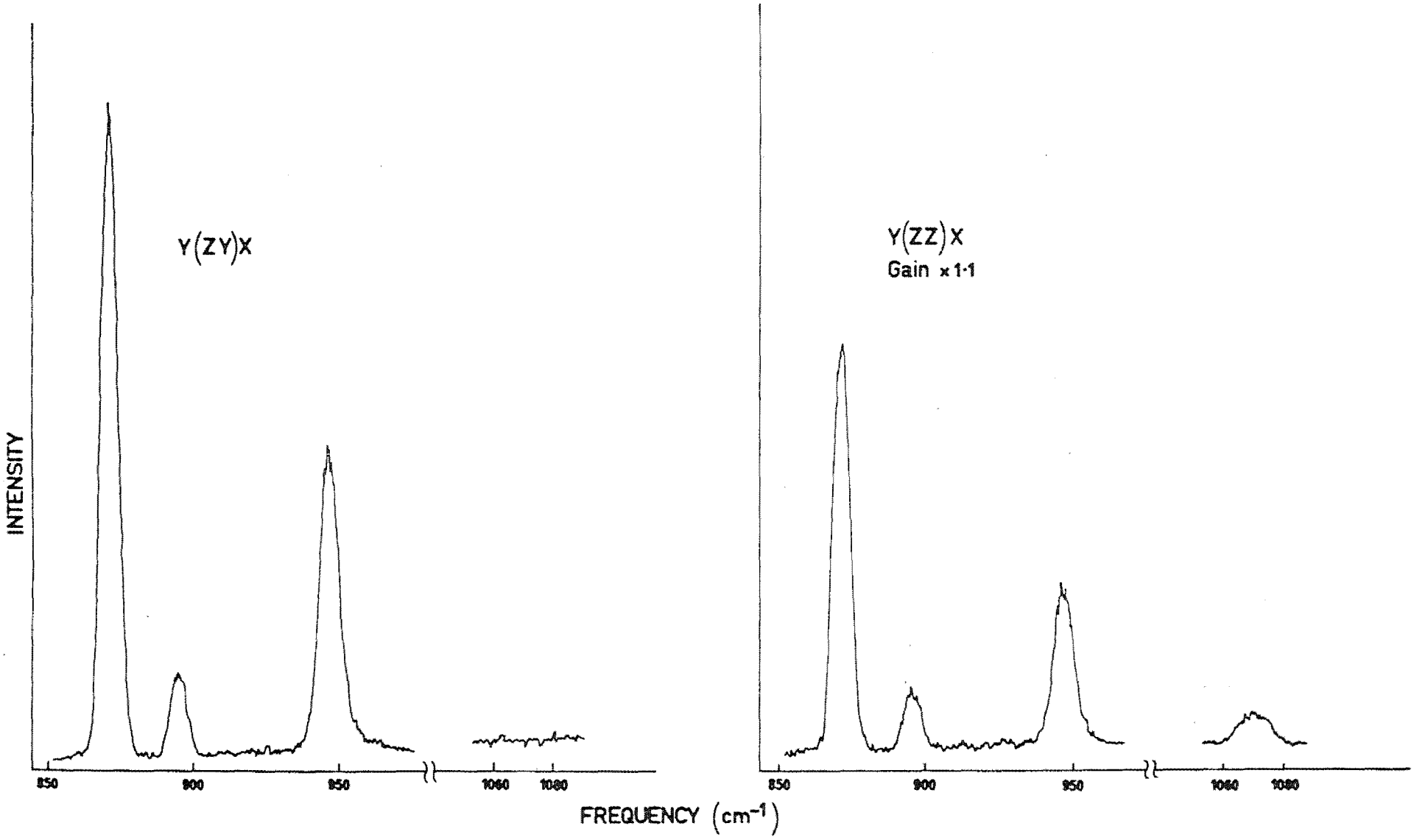

Fig. 4-4: $15^{\circ}K$ polarized Raman spectra of $CsCdCl_3$:Co 5 mole %

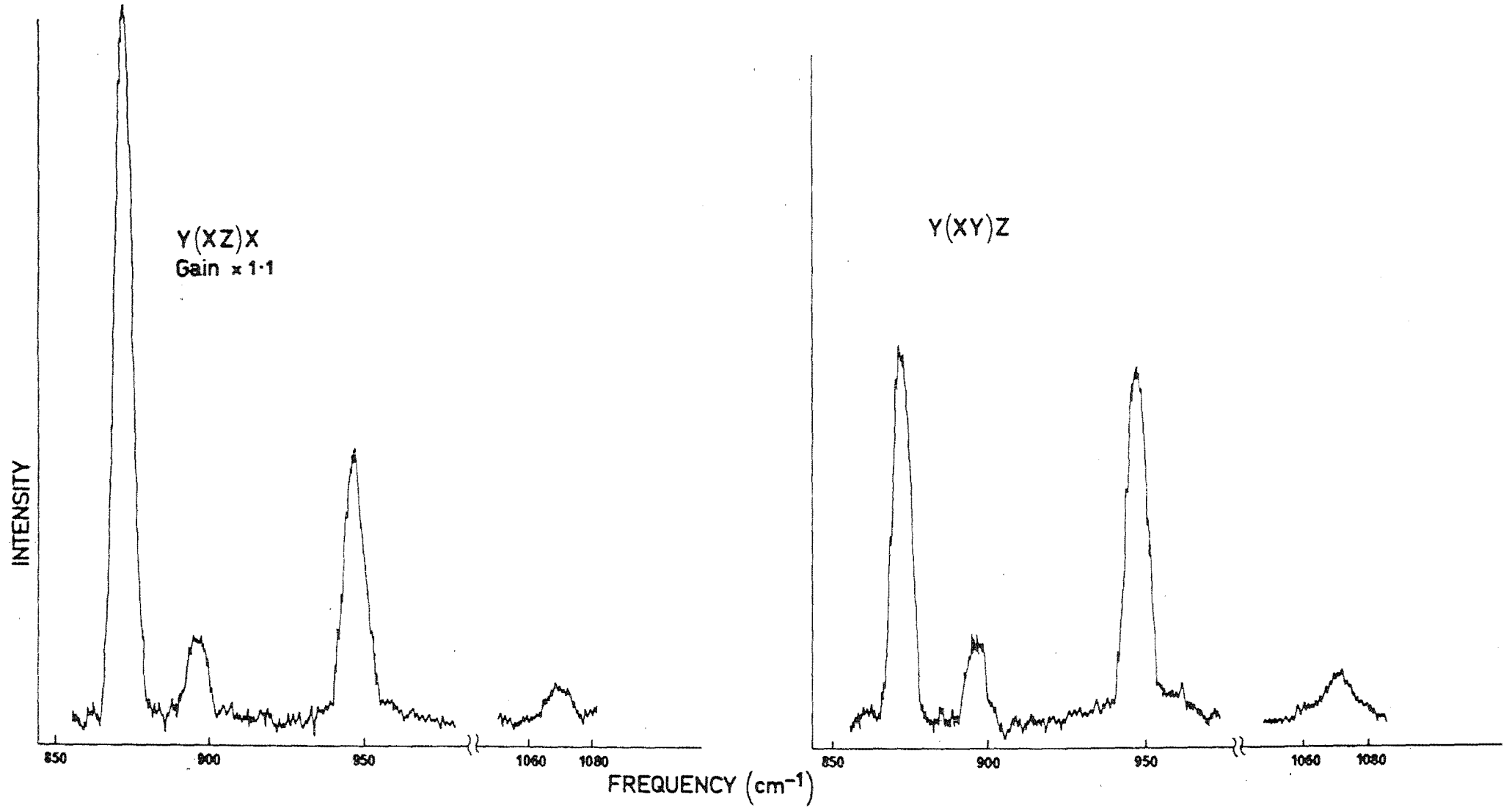

strongest and it is only in the (XY) configuration that they have roughly equal intensities. The intensity of the 897 cm^{-1} line shows little variation in all the four polarization configurations of the spectrum. In contrast the 1070 cm^{-1} line is more sensitive to polarization and is absent in the (ZY) configuration.

Apart from an intensity increase, increasing the Co^{2+} ion concentration to 10% does not alter the features of the spectrum. The frequencies of the transitions obtained by scattering from the pure host crystals are inappreciably affected by the introduction of Co^{2+} ion impurities.

4.3.2 $CsMgCl_3$:Co

$CsMgCl_3$ crystals containing 3 and 5 weight % of $CoCl_2$ were investigated by Raman scattering using the 4727, 4765 and 4880Å radiation. Figs. 4-5 and 4-6 display the arbitrarily polarized 15°K spectra of $CsMgCl_3$:Co 5 wt. % while Tables 4-1 and 4-2 summarize the results obtained.

Lines shifted by 55.5, 129.0, 190.0, 234 and 257.0 cm^{-1} can be seen in the liquid helium spectrum. Except for the 234 cm^{-1} line they are intense and sharp with line widths ranging from 3 to 5 cm^{-1}. The 129.0 cm^{-1} line has an asymmetric profile due to a side band located on its high energy side. At liquid nitrogen temperatures, the weak 234 cm^{-1} line is obscured by the wings of the intense 257.0 cm^{-1} line.

Fig. 4-6 shows five lines of widely varying intensities in the middle and high energy portions of the spectrum. These lines occur at 472, 823, 848, 1264 and 1380 cm^{-1} with the 823 and 1264 cm^{-1} ones being the strongest. Among these the narrowest is the 823 cm^{-1} line while the broadest is the 472 cm^{-1} band with respective widths of 5 and 16 cm^{-1}. All these five lines together with the one at 234 cm^{-1} have intensities that increased with increasing Co^{2+} ion

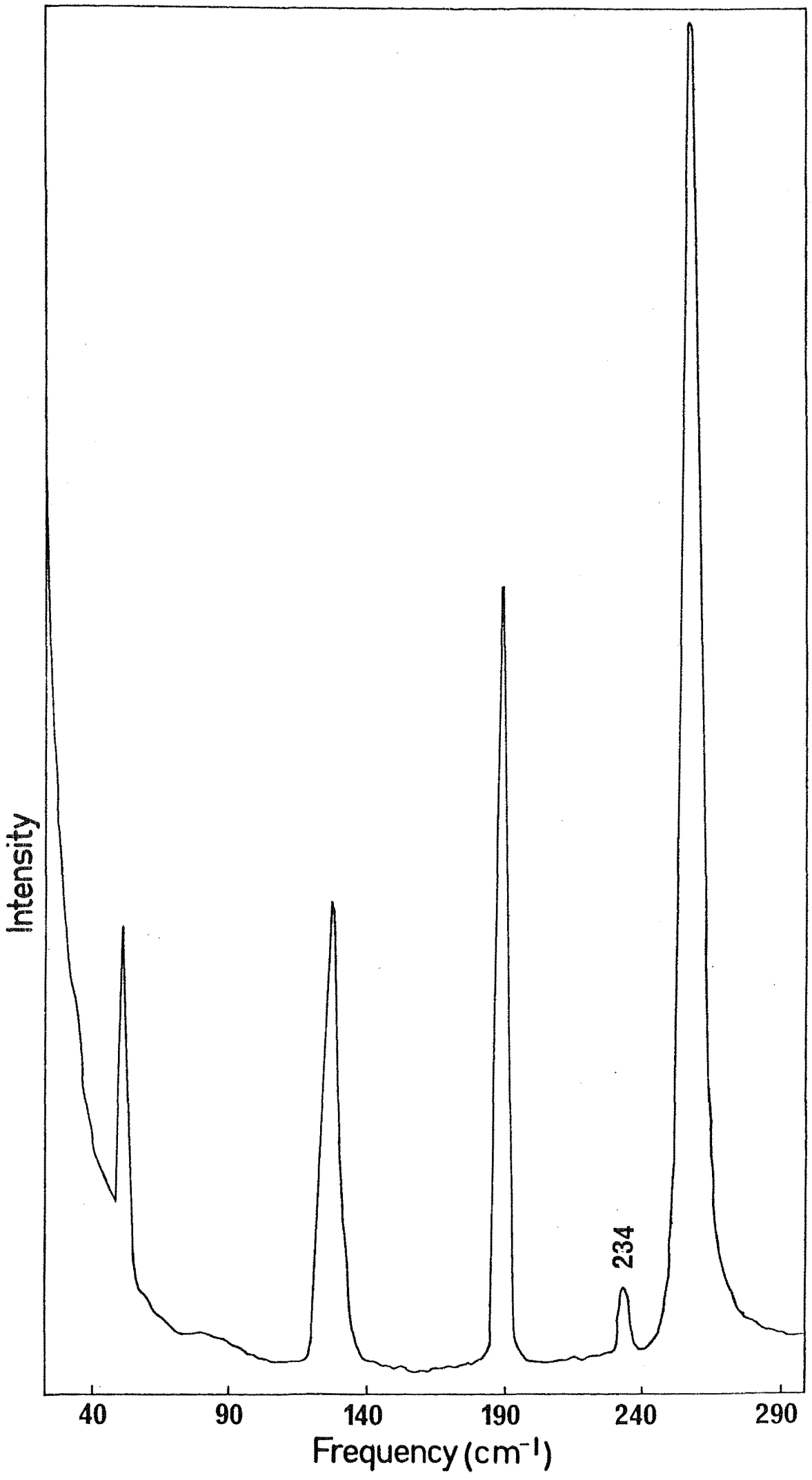

Fig. 4-5: Raman spectrum of $CsMgCl_3$:Co 5 wt. % measured at 15°K

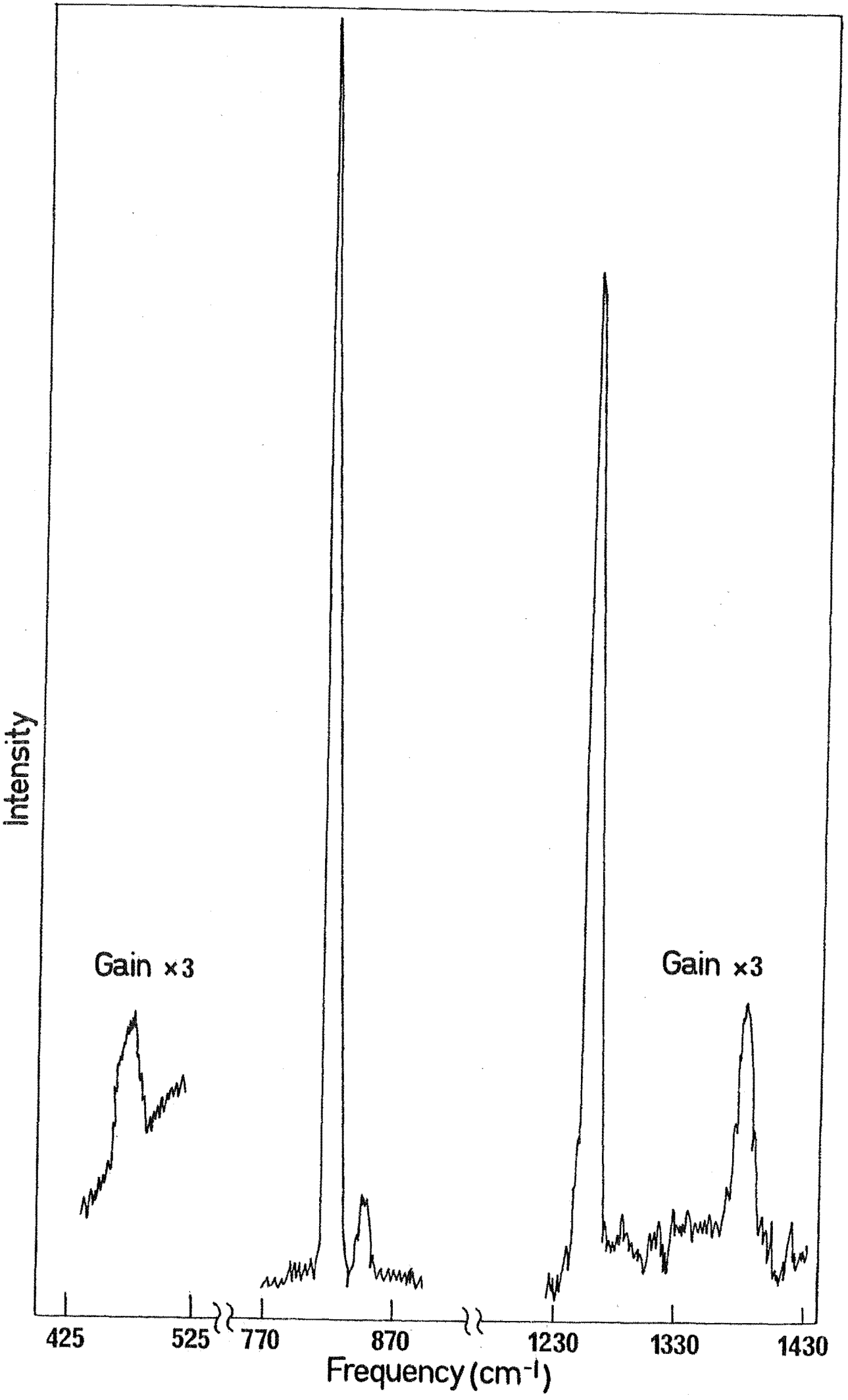

Fig. 4-6: Raman spectrum of $CsMgCl_3$:Co 5 wt. % measured at 15°K

concentration. Spectra obtained by scattering from Fe^{2+} doped crystals do not contain them. However the lines shifted by 55.5, 129.0, 190.0 and 257.0 cm^{-1} remained in these spectra.

One fluorescence line was encountered at the absolute frequency of 19,798 ± 2 cm^{-1} using the 4880Å excitation radiation. This line was not reproduced by scattering from Fe^{2+} doped crystals.

4.4 ANALYSIS OF THE RAMAN SPECTRA

Raman lines produced by scattering from pure host crystals are due to the phonon modes of the crystals themselves. The lines, whose frequencies are listed in Table 4-1, appear in the scattering spectra of pure $CsCdCl_3$ and $CsMgCl_3$ and are therefore ascribed to vibrational modes.

$CsMgCl_3$ has two formula molecules per unit cell and so possesses 27 optical phonon modes. Five Raman-active and five infrared- active modes are predicted from a factor-group analysis based on the $CsMgCl_3$ structure. Of the Raman-active modes, which are given by the representation

$$\Gamma = A_{1g} + E_{1g} + 3E_{2g} \ , \qquad (4\text{-}1)$$

four are internal modes of vibration associated with chains of $[MgCl_6]^{4-}$ octahedra while one (E_{2g}) is a translatory lattice mode. The infrared-active modes, given by the representation

$$\Gamma = 2A_{2u} + 3E_{1u} \ , \qquad (4\text{-}2)$$

consist of three internal modes and two translatory lattice modes ($A_{2u} + E_{1u}$). Chadwick et.al.[24], have detected lines at 54, 133, 183 and 264 cm^{-1} in the polarized Raman spectrum of $CsCoCl_3$ and identified them as E_{2g},E_{1g},E_{2g} and A_{1g} modes respectively.

$CsMgCl_3$ is isomorphous with $CsCoCl_3$ and the frequencies of its Raman lines are close to those of $CsCoCl_3$. On the basis of this, the 55.5, 129.0, 190.0 and 257.0 cm^{-1} Raman lines are tentatively assigned as the E_{2g},E_{1g},E_{2g} and A_{1g} modes of $CsMgCl_3$. Polarization studies are needed to confirm the species assignment of these lines.

As $CsCdCl_3$ has six formula molecules per unit cell, the number of optical phonon modes permitted is 87. Owing to the large number of possible modes and the complicated ion arrangement of this crystal, no attempt was made to determine the symmetry species of the observed phonon lines of $CsCdCl_3$.

The Raman lines whose frequencies appear in Table 4-2 are attributed to electronic transitions of the Co^{2+} ion for the following reasons. Firstly they are not present in the Raman scattering spectra of corresponding Fe^{2+} doped crystals and secondly their intensities correlate with the Co^{2+} concentration. Their electronic nature is confirmed by their Zeeman shifts observed in the Zeeman-Raman experiments (Chapter V). Analyses of the electronic Raman results are considered separately for the two double chlorides below.

4.4.1 $CsCdCl_3$:Co

As stated in Sec.2.1, the Cd^{2+} ions in $CsCdCl_3$ occupy two distinct types of sites having D_{3d} and C_{3v} symmetries with the ratio of Cd(1) to Cd(2) sites being 1:2. However several workers studying the E.P.R. spectra of transition metal ions in these crystals have found that these impurity ions do not occupy the two possible cadmium sites in this ratio. Chang et.al.[1], discovered that V^{2+} and Ni^{2+} ions substitute almost exclusively in one of the two cadmium sites. While they could not positively identify this site they did suggest it to be the smaller D_{3d} site. McPherson and Chang[25] found that the Mn^{2+} ions show little

discrimination in the occupation of either site and that the ratio of the two kinds of Mn^{2+} sites is 3:7. On the other hand Graham and White[26] found that Cu^{2+} ions have a preference for the larger C_{3v} sites.

Cobalt ions have been examined by EPR by Edgar[27] using concentrations of 0.1%. He found that these ions occurred in sites in the ratio 1:10 and suggested that the C_{3v} sites have the higher occupancy. In the $CsCdCl_3$ crystals studied in this thesis, Co^{2+} ion concentrations of up to 10 mole % were used. So although the relative Co^{2+} ion occupancy of the two sites can be different from Edgar's EPR ratio it is expected that the Co^{2+} ions substitute into both sites.

Four electronic lines shifted by 873, 897, 947 and 1070 cm^{-1} were observed for $CsCdCl_3$:Co. They are transitions due to both Co(1) and Co(2) ions. Reference to the infrared absorption results of Chapter VI was made in order to sort out the two different types of cobalt transitions. As the C_{3v} site lacks inversion symmetry, electric dipole transitions of cobalt ions in these sites are not forbidden. The infrared absorption data reveal that the 873 and 947 cm^{-1} lines are electric dipole in nature and are therefore attributed to cobalt ions in the C_{3v} sites.

As the 897 cm^{-1} line does not appear in the infrared spectra, it was ascribed to cobalt ions in the D_{3d} sites. These sites possess inversion symmetry and pure electronic transitions would only be magnetic dipole allowed and hence weak. The 897 cm^{-1} line also has a weak scattering in comparison with the 893 and 947 cm^{-1} lines, consistent with the 1:10 ratio of the Co(1) and Co(2) sites found by Edgar[27]. Furthermore the 897 cm^{-1} line was found to be rather insensitive to polarization, consistent with the nearly perfect octahedral D_{3d} site (Sec. 2.1).

The polarized spectrum of Fig. 4-3 shows that the (ZZ) spectral intensities of the 947 and 873 cm^{-1} lines are reduced by 60% and 35%

respectively. The $\gamma_{5,6}$ line has, in principle, a zero scattering in the (ZZ) polarization (Sec.4.2). The 947 and 873 cm^{-1} lines are therefore assigned as transitions from the $\gamma_4(\Gamma_6)$ ground state to the $\gamma_{5,6}(\Gamma'_8)$ and $\gamma_4(\Gamma'_8)$ excited states respectively of the Co(2) ion. The former line does not have a zero intensity in the (ZZ) polarization due to insufficient crystal quality such as the possible wandering of the c axis within the crystal[28]. Any slight misalignment of the crystal would also contribute to the observed depolarization. $CsCdCl_3$ grown from purification by phosgene gas instead of the usual hydrogen chloride gas were no better in quality and similar polarization results were obtained. No improvement to the polarization results was found using the back scattering technique.

The highest energy line at 1070 cm^{-1} is assigned to the $\gamma_4(\Gamma_7)$ level of the Co(2) ion. Transitions to the lowest two levels $\gamma_{5,6}(\Gamma_8)$ and $\gamma_4(\Gamma_8)$ predicted to lie at 395.5 and 291.1 cm^{-1} were not detected because of their weak intensities and also because they occurred among the host lattice phonon lines.

4.4.2 $CsMgCl_3$:Co

The complete set of five transitions within the $^4T_{1g}$ ground term of cobalt ions in $CsMgCl_3$ as well as an additional line at 848 cm^{-1} were observed. Three of these lines at 234, 823 and 1264 cm^{-1} are in agreement with those reported by Kardontchik et.al.[22], who assigned them as the $\gamma_4^+(\Gamma_8^+)$, $\gamma_4^+(\Gamma_8'^+)$ and $\gamma_{5,6}^+(\Gamma_8'^+)$ states respectively. The infrared absorption measurements described in Sec.6.4 confirm the symmetry assignments of the 823 and 1264 cm^{-1} lines.

The other two lines, first reported here, at 472 and 1380 cm^{-1} are assigned to the remaining transitions within the $^4T_{1g}$ ground term.

Although polarization Raman studies were not possible on these weak lines the Zeeman-infrared results reported in Chapter VII show that the 1380 cm^{-1} line is due to the $\gamma_4^+(\Gamma_6^+) \rightarrow \gamma_4^+(\Gamma_7^+)$ transition. The remaining line at 472 cm^{-1} is assigned as a $\gamma_4^+(\Gamma_6^+) \rightarrow \gamma_{5,6}^+(\Gamma_8^+)$ transition.

The additional line at 848 cm^{-1} is absent from the infrared absorption spectra and is unassigned. It could arise from clusters of at least two cobalt ions.

4.5 CRYSTAL FIELD FITTING OF EXPERIMENTAL DATA

All the single ion electronic transitions observed are between the six spin-orbit and trigonal crystal field levels of the $^4T_{1g}(^4F)$ cubic field ground manifold. These levels can be determined by the crystal field theory in terms of the spin-orbit parameters ζ and ζ' and the trigonal field parameters v and v' and are also indirectly dependent on the values of the cubic field parameter Dq and the electrostatic parameters B and C. Since ζ and ζ' are frequently closely equal as was found for $CdCl_2$-type crystals[29], for the analysis ζ was set equal to ζ' and the energy fit was thus made using only three independent parameters v,v' and ζ. With three parameters only, systems for which more than two electronic transitions are known can be analysed.

The Co(1) system of $CsCdCl_3$ for which only one transition was detected could not therefore be analysed.

A preliminary fitting was performed for both the cobalt ions in the C_{3v} sites of $CsCdCl_3$ and in the D_{3d} sites of $CsMgCl_3$ using the crystal field parameters obtained by Edgar[27] using a superposition crystal field model developed by Newman[30]. In this the crystal field is described in terms of the B_q^k crystal field parameters and the tensor operators C_q^k as

$$V_{CF} = \sum_{i=1} \{[B_o^2 C_o^2 + (B_o^4 + \sqrt{\frac{7}{10}} B_3^4) C_o^4] - \sqrt{\frac{7}{10}} B_3^4 [C_o^4 - \sqrt{\frac{10}{7}} (C_{-3}^4 - C_3^4)]\} \tag{4.3}$$

where the first and second parts are the trigonal and cubic components of the crystal field. The summation is over three holes in the 3d shell.

In the superposition model, the B_q^k parameters are expressed in terms of the intrinsic parameters $\bar{B}_q^k$ and the angular positions (θ_j, ϕ_j) of the j ligands relative to the central ion by

$$B_q^k = \sum_j \bar{B}^k \; C_q^k(\theta_j, \phi_j) \tag{4.4}$$

where the relevant coordination factors C_q^k are

$$\begin{aligned} C_o^2 &= (3\cos^2\theta - 1)/2 \\ C_o^4 &= (35\cos^4\theta - 30\cos^2\theta + 3)/8 \\ C_3^4 &= 35\cos\theta \sin^3\theta \cos 3\phi \\ C_{-3}^4 &= 35\cos\theta \sin^3\theta \sin 3\phi \end{aligned} \tag{4.5}$$

The angular positions of the ligands for the Cd(2) and Mg cation sites of $CsCdCl_3$ and $CsMgCl_3$ are given by Edgar[27]. Using these angular positions and the intrinsic parameters $\bar{B}^2$ and $\bar{B}^4$ values of $CdCl_2$ he calculated the parameters B_o^2, B_o^4 and B_3^4 for the crystal fields due to the ligands for the above double chlorides. The crystal fields due to the more distant ions were estimated on a point charge model and the crystal field parameters for the total crystal field experienced by the Co^{2+} ion in the two systems are given below in units of cm^{-1}.

	B_o^2	B_o^4	B_3^4
$CsCdCl_3$:Co(2)	90	9781	-11135
$CsMgCl_3$:Co	-716	10678	-10839

These B_q^k parameters are related to the strong field parameters Dq, v and v' by

$$Dq = \left(\frac{7}{3}\sqrt{\frac{7}{5}} + \frac{28}{3}\sqrt{\frac{5}{7}}\right)^{-1} \{B_3^4 + \sqrt{\frac{10}{7}}\, B_o^4 - \left(\frac{2}{3}\sqrt{\frac{7}{10}} + \frac{4}{3}\sqrt{\frac{10}{7}}\right) B_o^2\}$$

$$v = B_o^2 + 2\sqrt{2}\, v' \qquad (4.6)$$

$$v' = \frac{1}{14}\left(\frac{4}{3} v + 2\sqrt{2}\, v' - B_o^4\right)$$

These are corrected relations from those of Edgar who gave $B_o^2 = v - \sqrt{2}\, v'$ instead of $B_o^2 = v - 2\sqrt{2}\, v'$. Substitution of Edgar's parameter values into the above yielded respective Dq values of -678 and -674 cm^{-1} for $CsMgCl_3$:Co and $CsCdCl_3$:Co(2). For both systems the parameters B and C were set at the respective values of 790 and 3320 cm^{-1} determined for $CdCl_2$:Co by Robson[31].

The total crystal field is a sum of superposition model contributions from the nearest-neighbour ligands and the point charge model contributions from the more distant ions. The B_o^2 values for these are comparable and are of opposite sign for both $CsMgCl_3$:Co and $CsCdCl_3$:Co(2). Hence for the initial crystal fitting the only parameters varied are the second-order axial parameter B_o^2 and the spin-orbit parameter $\zeta(=\zeta')$. A fit to within 2 cm^{-1} was obtained. A least-squares routine then varied all three parameters ζ, v and v' until agreement to within experimental accuracy was obtained. Their final values are listed in Table 4-2 together with the energy level fits. Both $CsMgCl_3$:Co and $CsCdCl_3$:Co(2) have the Γ_8^+ doublet levels inverted with respect to the case of $CdCl_2$:Co for which v = 57, v' = -345, ζ = -512 and ζ' = -513 cm^{-1} (Ref.29).

The coordination sphere of the cobalt ion is elongated along the [111] cubic axis for the double chlorides while for the case of $CdCl_2$ it is compressed in the [111] cubic axis. This gives quite different ratios of the v and v' parameter values in all three crystals which is sufficient to give an altered energy level scheme for $CdCl_2$ as compared to the double chlorides.

The final values of B_o^2 and B_o^4 obtained from the least-squares fit are 529 and 9671 cm^{-1} for $CsCdCl_3$:Co(2) and -1412 and 11,208 cm^{-1} for $CsMgCl_3$:Co. While the B_o^4 values are in good agreement with those estimated by Edgar, the B_o^2 values differ rather significantly from his values of 90 and -716 cm^{-1} for $CsCdCl_3$:Co(2) and $CsMgCl_3$:Co respectively. Substitution of these final B_o^2 and B_o^4 values into equation 4.4 yield intrinsic parameters $\bar{B}^2$ and $\bar{B}^4$ values of -799 and -4014 cm^{-1} for $CsCdCl_3$:Co(2) and -12559 and -4271 cm^{-1} for $CsMgCl_3$:Co. In his calculation of the crystal fields for cobalt ions in the two double chlorides, Edgar assumed their values of the intrinsic parameters $\bar{B}^2$ and $\bar{B}^4$ to be the same as those of $CdCl_2$:Co which are -11000 and -4060 cm^{-1}. While this assumption is reasonable for the case of $CsMgCl_3$:Co, it is shown by the data here to be not justifiable for the case of $CsCdCl_3$:Co(2).

The final values of the crystal field parameters, which are listed in Table 4-2, were used to evaluate the energies of the electronic states of the cobalt ion and their associated g values in both 0 and 40 kG fields using two computer programs Oscstrengths/120 and Oscstrengths/3942 listed in the appendix. The former program incorporates the entire 120-dimension energy matrix and is used for $\underline{H} \perp \underline{c}$. In the other program used for $\underline{H} \parallel \underline{c}$, the 120-dimension energy matrix is factorized into two 39-dimension $\gamma_4^+(-\frac{1}{2})$ and $\gamma_4^+(+\frac{1}{2})$ block matrices and a 42-dimension $\gamma_{5,6}^+$ matrix. This factorization was done because the Z component of the Zeeman operator, appropriate for $\underline{H} \parallel \underline{c}$, only connects states labelled by the same irreps. The computed frequencies and g values of the low-lying electronic levels of cobalt ions in $CsCdCl_3$ and $CsMgCl_3$ are listed in Tables 4-2 and 4-3 respectively.

TABLE 4-3: Computed g values of the Co^{2+} ion in $CsMgCl_3$ and $CsCdCl_3$ at 0 and 40kG fields.

State	0 kG		40 kG			
			H∥c		H⊥c	
	$g_{\|}$	$g_{\perp}$	$g_{\|}$	$g_{\perp}$	$g_{\|}$	$g_{\perp}$
$\gamma_4^+(\Gamma_7^+)$	2.02	3.12	2.02	3.12	2.02	3.12
$\gamma_{5,6}^+(\Gamma'^+_8)$	5.21	0.0	6.06	0.0	6.05	0.0
$\gamma_4^+(\Gamma'^+_8)$	3.13	0.10	3.13	0.10	3.13	0.10
$\gamma_{5,6}^+(\Gamma_8^+)$	0.18	0.0	0.52	0.0	0.49	0.0
$\gamma_4^+(\Gamma_8^+)$	3.56	1.34	3.56	1.34	3.56	1.34
$\gamma_4^+(\Gamma_6^+)$	7.81	2.17	7.80	2.17	7.81	2.17
	$CsCdCl_3$:Co(2)					
$\gamma_4(\Gamma_7)$	1.19	2.05	1.19	2.05		
$\gamma_{5,6}(\Gamma_8)$	3.65	0.0	3.89	0.0		
$\gamma_4(\Gamma_8)$	2.93	0.48	2.93	0.48		
$\gamma_{5,6}(\Gamma_8)$	2.31	0.0	2.42	0.0		
$\gamma_4(\Gamma_8)$	0.64	2.48	0.64	2.48		
$\gamma_4(\Gamma_6)$	5.36	3.97	5.36	3.97		

CHAPTER V

ZEEMAN-RAMAN

5.1 INTRODUCTION

As stated in Sec. 2.2 the electronic states of the cobalt ion are split in the presence of a magnetic field. The magnetic splitting factors of these states can be obtained by a Raman study of the transitions between the split electronic components of these states. An electronic Zeeman-Raman investigation of cobalt ions in $CsMgCl_3$ and $CsCdCl_3$ was made as a sequel to the Raman work described in the preceding chapter. The two strongest lines due to the $\gamma_4^+(\Gamma_6^+) \rightarrow \gamma_4^+(\Gamma_8'^+)$ and $\gamma_4^+(\Gamma_6^+) \rightarrow \gamma_{5,6}^+(\Gamma_8'^+)$ transitions are sufficiently intense and narrow for Zeeman-Raman measurements to be feasible. They are also well isolated from neighbouring lines which might interfere with any resulting Zeeman splittings or shifts.

The static magnetic field was generated by a 60 kG superconducting magnet which, together with the specimens, was immersed in pumped liquid helium at $2^{\circ}K$. Spectral scans were done at two crystal orientations viz., with the c axis directed along and at right angles to the magnetic field. These orientations will be referred to as $H \| c$ and $H \perp c$ respectively Because of the restricted optical access of the Zeeman-Raman system, the detection system was operated at its maximum sensitivity.

None of the electronic Raman lines examined exhibited any detectable splitting. In case the split components of a given electronic line could have been partially superimposed on each other, a polarizer was inserted in the scattered beam in an attempt to separate them. However no effect on the frequencies of the electronic Zeeman-Raman lines was found when the polarizer was present.

An account of the Zeeman-Raman spectra of cobalt ions in $CsCdCl_3$

and $CsMgCl_3$ is presented in Sec. 5.2. The analysis of the experimental data is given in Sec. 5.3.

5.2 DESCRIPTION OF THE ZEEMAN-RAMAN SPECTRA

5.2.1 $CsCdCl_3$:Co

The 4765 and 4880Å laser lines were used to excite $CsCdCl_3$ crystals containing a nominal molar doping of 5% $CsCoCl_3$. Laser output of up to 2.5W was used with the spectral slit widths ranging from 1.5 to 2.5 cm^{-1}. Spectra were recorded at magnetic field strenghts of 20, 40 and 60 kG and typical spectra are displayed in Fig. 5-1. None of the electronic lines examined showed any splittings nor signs of broadening. The variations in the line widths detected for any one electronic level at different field strengths are of the order of the experimental uncertainties. Nevertheless the peaks of the electronic lines moved up to higher frequencies when the magnetic field was applied. The shifts were found to be proportional to the magnitude of the applied field.

The Zeeman data for the $\gamma_4(\Gamma_8')$ and $\gamma_{5,6}(\Gamma_8')$ lines of the Co(2) ions together with the $\Gamma_8'^+$ doublet of Co(1) ions for both $\underline{H}\|\underline{c}$ and $\underline{H}\perp\underline{c}$ are summarized in Table 5-1. The notation ΔE_n which appears in the table denotes the displacements observed, in cm^{-1}, of the electronic Raman lines from their zero-field positions.

At maximum field the $\gamma_4(\Gamma_8')$ and $\gamma_{5,6}(\Gamma_8')$ lines shifted by 4.7 and 5.2 cm^{-1} for $\underline{H}\perp\underline{c}$ while for the $\underline{H}\|\underline{c}$ orientation the respective shifts were 3.2 and 2.4 cm^{-1}. For a 60 kG field directed perpendicular to the $\underline{c}$ axis, a shift of 2.8 cm^{-1} was recorded for the $\Gamma_8'^+$ doublet of the Co(1) ion.

Fig. 5-1: Electronic Zeeman-Raman spectra of Co^{2+} ions in $CsMgCl_3$ and $CsCdCl_3$ recorded at $2^{o}K$.

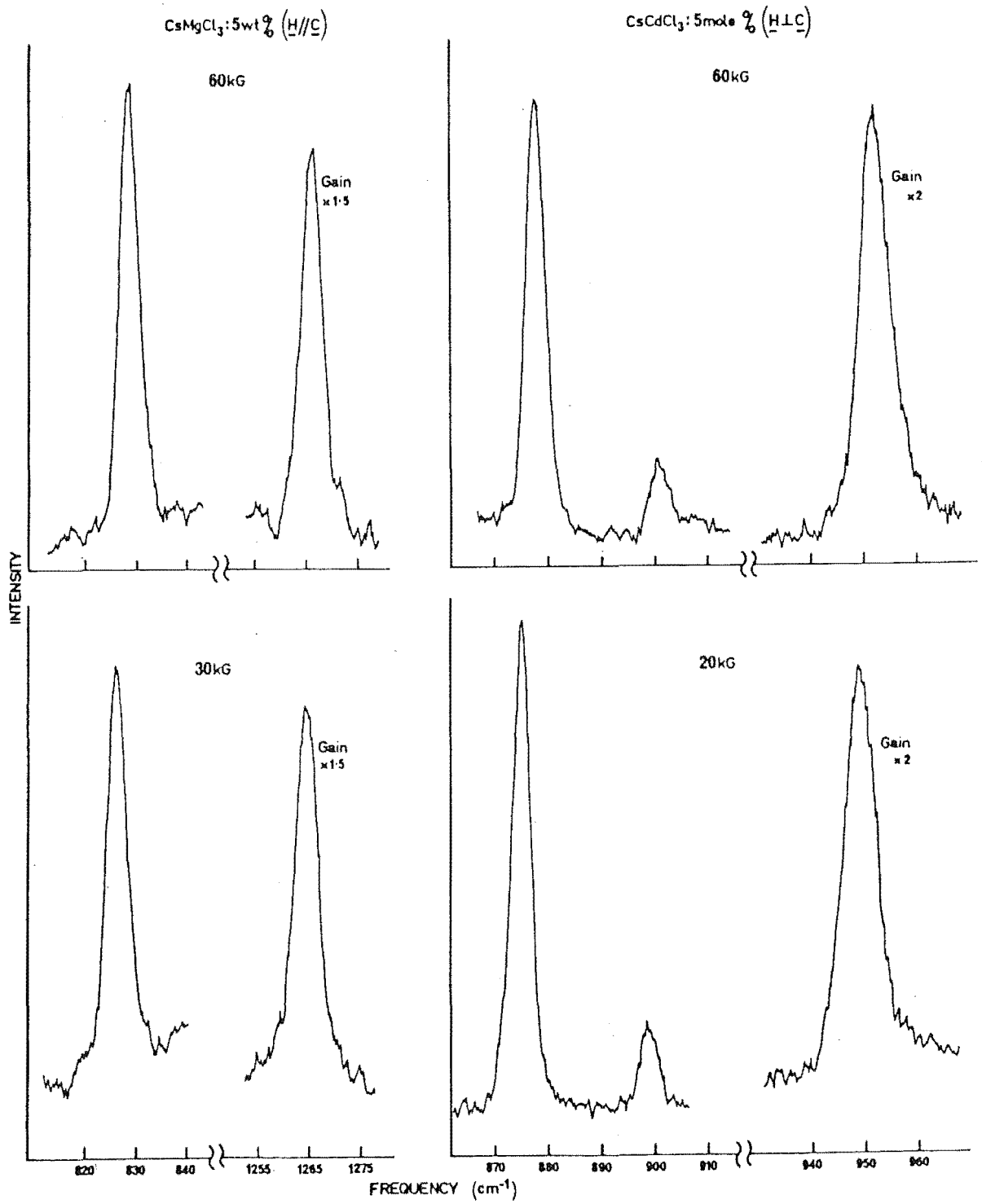

TABLE 5-1: Zeeman-Raman data on $CsCdCl_3$:Co(2) and $CsMgCl_3$:Co at $2^{o}K$. The symbols ΔE_n and w denote the shifts of the Raman lines from the zero field positions and the corresponding linewidths in cm^{-1} respectively. Each value of ΔE_n and w has an experimental uncertainty of $\pm 0.4\ cm^{-1}$.

		$CsCdCl_3$				$CsMgCl_3$					
H(kG)		20		40		60		30		60	
		w	ΔE_n	w	ΔE_n	w	ΔE_n	w	ΔE_n	w	ΔE_n
H⊥c	$\Upsilon_{5,6}^{+}(\Gamma_8'^{+})$	6.8	1.5	6.3	3.4	6.5	5.2			5.8	3.5
	$\Upsilon_4^{+}(\Gamma_8'^{+})$	4.0	1.4	4.0	3.1	4.4	4.7			5.4	3.1
	$\Gamma_8'^{+a}$	4.3	0.5	4.0	2.0	4.2	2.8				
H∥c	$\Upsilon_{5,6}^{+}(\Gamma_8'^{+})$	4.7	0.8	4.4	1.5	4.5	2.4	5.1	1.2	5.3	2.3
	$\Upsilon_4^{+}(\Gamma_8'^{+})$	3.4	0.8	3.3	1.9	3.2	3.2	4.6	3.1	4.3	6.0

a: $\Gamma_8'^{+}$ state of Co(1) in $CsCdCl_3$.

5.2.2 $CsMgCl_3$:Co

Electronic Zeeman-Raman spectra of $CsMgCl_3$ crystals containing 2.5 and 5.0% by weight of $CoCl_2$ were obtained using the 4765Å laser line and the same spectrometer settings as for $CsCdCl_3$:Co. The behaviour of the $\gamma_4^+(\Gamma_8'^+)$ and $\gamma_{5,6}^+(\Gamma_8'^+)$ electronic lines were studied at various magnetic field strengths. Portions of the spectra are shown in Fig.5-1 while Table 5-1 lists the experimental results.

As for $CsCdCl_3$:Co, no splittings or broadening of the electronic lines were detected. Again the only effect of the magnetic field was the shifting of the lines to higher frequencies. On application of a 60 kG field, the $\gamma_4^+(\Gamma_8'^+)$ and $\gamma_{5,6}^+(\Gamma_8'^+)$ lines were seen to shift by 3.1 and 3.5 cm^{-1} for $\underline{H} \perp \underline{c}$ while corresponding shifts of 6.0 and 2.3 cm^{-1} were recorded for $\underline{H} \parallel \underline{c}$.

5.3 ANALYSIS OF THE ZEEMAN-RAMAN SPECTRA

Although no visual splitting of the electronic Raman levels occurred the magnetic splitting factors of these levels (g) can still be extracted from the Zeeman data as will be shown below. When the magnetic field is applied all the electronic Raman lines shifted to higher frequencies. These shifts are proportional to the magnitude of the applied field indicating that magnetic field interaction between adjacent electronic states is negligible.

In an external magnetic field both the initial and final electronic states of a given transition are split into two components. For the ground state the upper component is depopulated at $2^{o}K$ and hence all the Zeeman-Raman transitions originate from the lower component. In general there should be one transition to each of the two components of the split excited state. However only one of these was observed for

each zero-field excited state.

The $g_\perp$ values for the $\gamma_4^+(\Gamma_8'^+)$ state of $CsMgCl_3$:Co and $CsCdCl_3$:Co(2) are less than 0.5 and its Zeeman components could not be resolved. The $g_\perp$ value of the $\gamma_{5,6}^+(\Gamma_8'^+)$ state is zero. Hence only one transition to each of these states was observed for $\underline{H} \perp \underline{c}$. This contrasts with the case of $MgCl_2$:Co where a splitting of 5 cm^{-1} was recorded at 60kG for the $\gamma_4^+(\Gamma_8'^+)$ state consistent with its relatively large predicted $g_\perp$ value of 1.86[32]. Despite their large $g_\parallel$ values (Table 4-3), no splittings of the $\gamma_4^+(\Gamma_8'^+)$ and $\gamma_{5,6}^+(\Gamma_8'^+)$ lines were detected in the $\underline{H} \parallel \underline{c}$ spectra. This is ascribed to the weak intensities of their absent Zeeman components.

The frequencies of all possible electronic transitions can be calculated in the following manner. The shifts of the ground and excited states from their zero-field positions are first evaluated from the EPR[27],[33] and computed g values respectively (Table 4-3). By adding or subtracting these shifts from the experimental zero-field transition frequencies, the Zeeman transition frequencies can thus be obtained. Zeeman-infrared studies of $CsMgCl_3$:Co and $CsCdCl_3$:Co yielded more complete results and hence the Zeeman levels were assigned using these Zeeman-infrared results (Chapter VII). Using the Zeeman-infrared energy level schemes, the observed electronic Zeeman-Raman transitions were matched to appropriate energy level separations. Figs. 5-2 and 5-3 which summarize the experimental and calculated frequencies of the electronic Zeeman-Raman transitions together with their assignments, show that the two sets of transition frequencies are in good agreement.

In general the observed shift ΔE_n of a Zeeman line from its zero-field frequency is the difference in the shift ΔE_o of the ground state up or down in energy and the shift ΔE of the excited state up or down in energy. This is mathematically expressed as

$$\Delta E_n = \Delta E_o \pm \Delta E \quad . \tag{5.1}$$

Fig.5-2: Zeeman energy-level diagram illustrating Raman transitions observed for $CsCdCl_3$:Co(2) 5 mole % at $2^{o}K$. Figures in parentheses denote the observed frequencies in cm^{-1}.

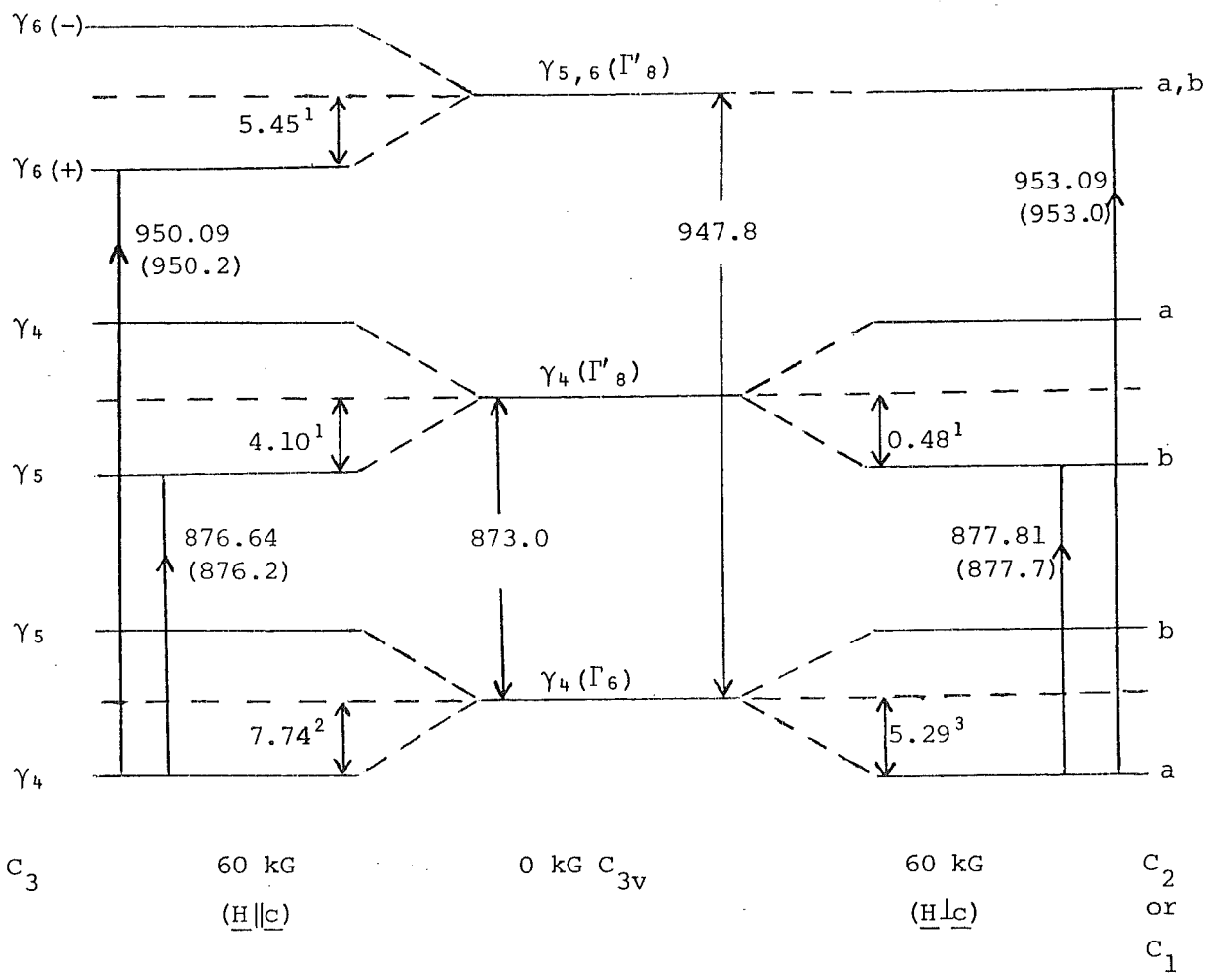

a = $\gamma_3(C_2)$ or $\gamma_2(+)(C_1)$ b = $\gamma_4(C_2)$ or $\gamma_2(-)(C_1)$

1 : Shifts calculated from computed g values of Table 4-3.

2,3 : Shifts calculated from EPR g values of 5.53 and 3.78 respectively.

Fig. 5-3: Zeeman energy-level diagram illustrating Raman transitions observed for $CsMgCl_3$:Co 2.5 and 5.0 wt. % at $2^{o}K$. Figures in parentheses denote the observed frequencies in cm^{-1}.

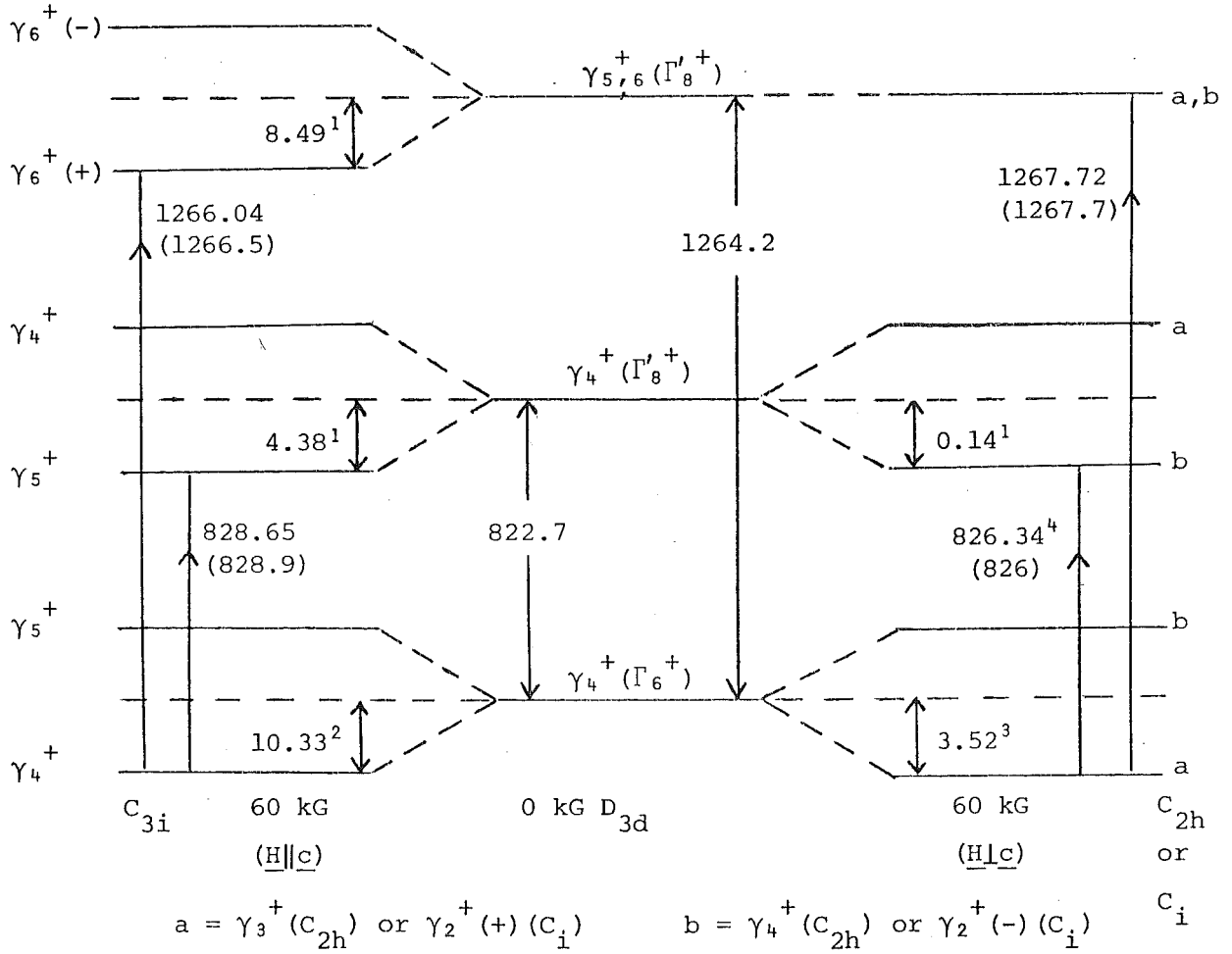

1 : Shifts calculated from computed g values of Table 4-3.

2,3 : Shifts calculated from EPR g values of 7.37 and 2.51 respectively.

4 : An unambiguous assignment cannot be made as the observed transition might have also terminated on the upper component a.

TABLE 5-2: Comparison of Zeeman-Raman experimental and computed g values of Co^{2+} at 60 kG.

Electronic state	$g_{\parallel}$ Expt.	Compt.	$g_{\perp}$ Expt.	Compt.
$CsMgCl_3$:Co				
$\gamma_{5,6}^{+}(\Gamma_8'^{+})$	5.73±0.28	6.06	0.01±0.28	0.00
$\gamma_4^{+}(\Gamma_8'^{+})$	3.08±0.28	3.13	0.30±0.28	0.10
$\gamma_4^{+}(\Gamma_6^{+})$	7.37[a]	7.80	2.51[a]	2.17
$CsCdCl_3$:Co(2)				
$\gamma_{5,6}(\Gamma_8')$	3.82±0.28	3.89	0.07±0.28	0.00
$\gamma_4(\Gamma_8')$	3.24±0.28	2.93	0.42±0.28	0.48
$\gamma_4(\Gamma_6)$	5.53[b]	5.36	3.78[b]	3.97

a: EPR values of Rinneberg and Hartmann[33]

b: EPR values of Edgar[27]

Now the energy shift ΔE_i in cm^{-1} of an electronic state i is related to its magnetic splitting factor g_i by

$$\Delta E_i = \frac{\beta H}{2} g_i \qquad (5.2)$$

where β(=0.04668 cm^{-1}/kG) is the Bohr magneton and H is the applied magnetic field in kG. The excited state magnetic splitting factor is thus given by

$$g = \pm \left[g_o - \frac{2}{\beta H} \Delta E_n \right] . \qquad (5.3)$$

Reference to Figs.5-2 and 5-3 shows that the electronic Zeeman-Raman transitions terminate on the lower split components of the excited states and hence the positive sign of equation (5.3) applies for this case. Thus the g values for the excited states can be evaluated from the

ground state g values, known from EPR measurements, and the net shifts of the electronic Zeeman-Raman lines. The resulting g values are listed in Table 5-2 and are in good agreement with those computed from the crystal field model.

CHAPTER VI

INFRARED ABSORPTION STUDIES

6.1 INTRODUCTION

In this chapter the axial and polarized infrared spectra of cobaltous ions doped in the double chlorides $CsMgCl_3$ and $CsCdCl_3$ are presented and discussed. The electronic transitions observed are between the spin-orbit and trigonal cyrstal field levels of the $^4T_{1g}(^4F)$ cubic field ground manifold of the cobaltous ion (Sec. 2.2). An analysis of the experimental results of Raman scattering from the two systems has been given in the previous chapter. The absorption spectra recorded comprise both pure electronic and vibronic bands, whereas the Raman spectra due to cobalt ions consist only of electronic transitions.

In both the double chlorides the cobalt ions are located in sites of trigonal symmetry. While these sites are centrosymmetric (D_{3d}) in $CsMgCl_3$, the majority of cobalt ions in $CsCdCl_3$ are in an environment lacking inversion symmetry (C_{3v}) - Sec. 4.4. Owing to this difference in site symmetry the single cobalt ion electronic transitions occur through different mechanisms for the two crystals. In $CsMgCl_3$:Co, electric dipole electronic transitions within the $^4T_{1g}$ cubic field term are strictly forbidden while magnetic dipole electronic transitions are allowed. The electronic lines of $CsMgCl_3$:Co are usually weaker than those of $CsCdCl_3$:Co(2) where the electronic transitions are principally electric dipole in character.

Both sharp and broad electric dipole polarized vibronic bands form part of the features of the spectra. Lattice phonon frequencies of the host crystals were obtained from analyses of these vibronic bands. The pure electronic and vibronic transitions are individually discussed below for each crystal.

6.2 GENERAL DESCRIPTION OF THE SPECTRA

The axial and polarized spectra of $CsMgCl_3$ and $CsCdCl_3$ containing cobalt ions were measured from 400-1700 cm^{-1}. Within this energy region the pure host crystals are transparent down to their reststrahlen absorption band edges which occur at 600 and 450 cm^{-1} for $CsMgCl_3$ and $CsCdCl_3$ respectively. Extra bands and lines occur in the spectra of cobalt-doped crystals. These bands and lines have intensities that are dependent on the cobalt ion concentration and are absent in spectra of Fe^{2+}-doped crystals. They are attributed to either no-phonon electronic transitions of the cobalt ions or vibronic transitions associated with these electronic transitions. The electronic infrared lines were identified by the coincidence of their frequencies, to within $\pm$ 2 cm^{-1}, with those of electronic transitions of cobalt ions observed in the Raman spectra of the same crystals. For the case of $CsMgCl_3$:Co, polarization studies can distinguish the electronic from the vibronic transitions as the former are magnetic dipole allowed while the latter are electric dipole in nature.

Sets of vibronic bands occur at definite energy separations from each of their parent electronic lines. These energy separations, or vibronic intervals, give the frequencies of peaks in the phonon density of states for the host crystals. Some of these frequencies match those of the $\underline{k} = 0$ optical phonons found by Raman scattering.

The spectra of $CsMgCl_3$:Co are characterized by strong vibronic bands relative to the electronic lines, while those of $CsCdCl_3$:Co have the electronic lines as their dominant feature. The spectra recorded for these two systems are described in the following section.

6.3 RESULTS

6.3.1 $CsMgCl_3$:Co

Infrared spectra of $CsMgCl_3$ doped with 0 to 2.5% by weight of $CoCl_2$ were recorded at liquid nitrogen and liquid helium temperatures. Figs. 6-1, 6-2 and 6-3 depict the main spectral features of these crystals while the associated spectral data are listed in Tables 6-1 and 6-2.

Axial Spectra

These have the c axis of the crystal along the direction of propagation of the incident radiation.

With the exception of a broad band centred at 1415 cm^{-1}, strong narrow lines are the main characteristics of the 80°K axial spectrum in the 700-1700 cm^{-1} region. The six most intense lines have peaks at 943.0, 1042.0, 1051.5, 1264.0, 1476.0 and 1592.0 cm^{-1} with the 1264.0 cm^{-1} line being the strongest. As with all the spectra recorded, the spectrum in Fig. 6-1 shows in addition, water vapour absorption lines in the 1300-1700 cm^{-1} region. These can be distinguished from the absorption lines due to the crystals by their known frequencies and by their independence of the crystals' temperature.

As can be seen from Figs. 6-2 and 6-3 the lines became sharper and shifted to lower frequencies when the crystals were cooled to 15°K. At this temperature, the 1262 cm^{-1} assumed an asymmetrical shape due to a side-band at 1256 cm^{-1}. The 1148 cm^{-1} line present in the 80°K spectrum vanished. Several weak lines at 80°K became more pronounced, among them are the 822.0, 843.0 and 1379.0 cm^{-1} lines.

Polarized Spectra

These are of two types. The π polarization spectra have the E vector of the incident radiation along the crystal c axis and the

Fig. 6-1: Axial and polarized infrared spectra of $CsMgCl_3$:Co 2.5 wt. % measured at $80^{\circ}K$

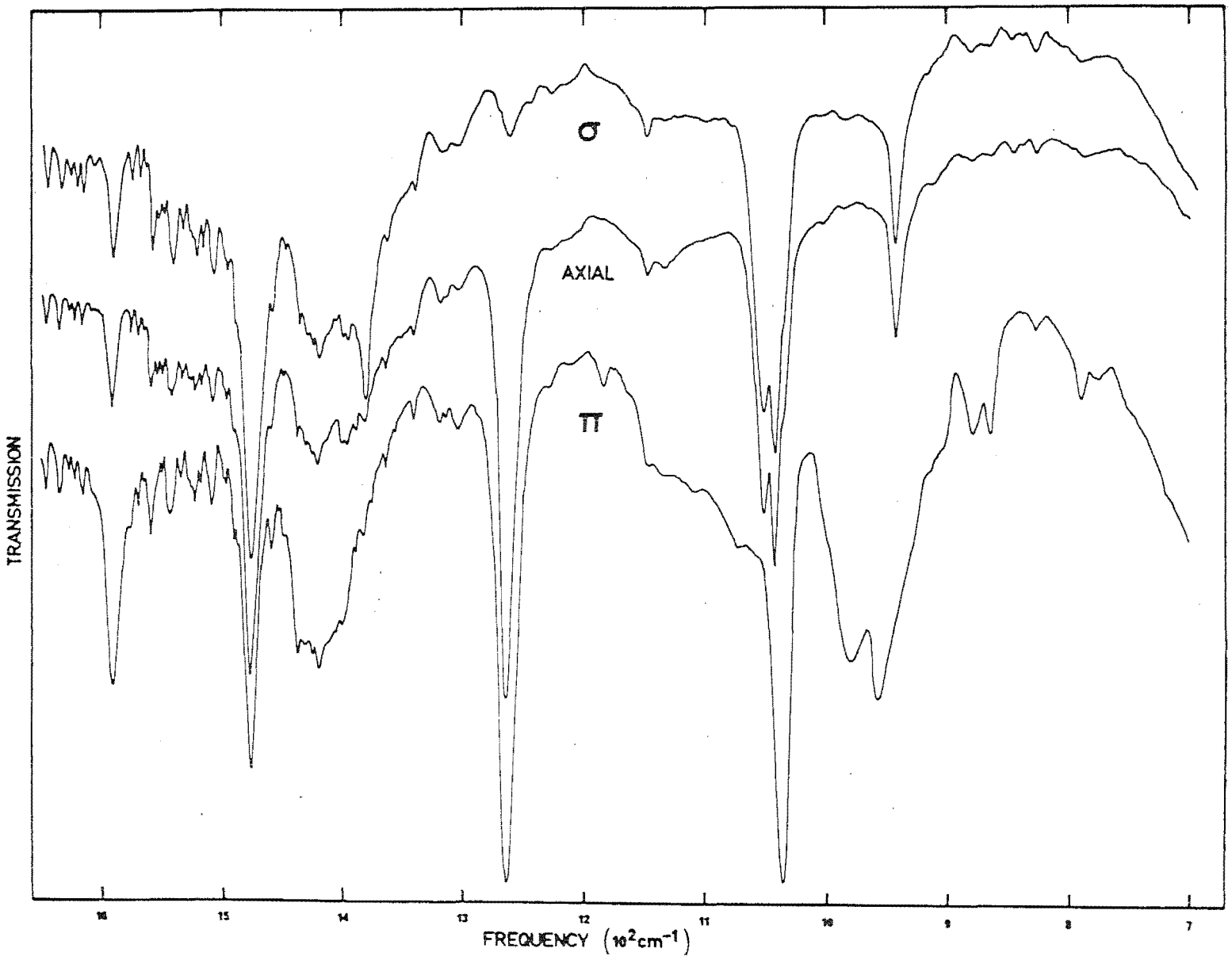

Fig. 6-2: Axial and polarized infrared spectra of $CsMgCl_3$:Co 2.5 wt. % measured at $15^{o}K$

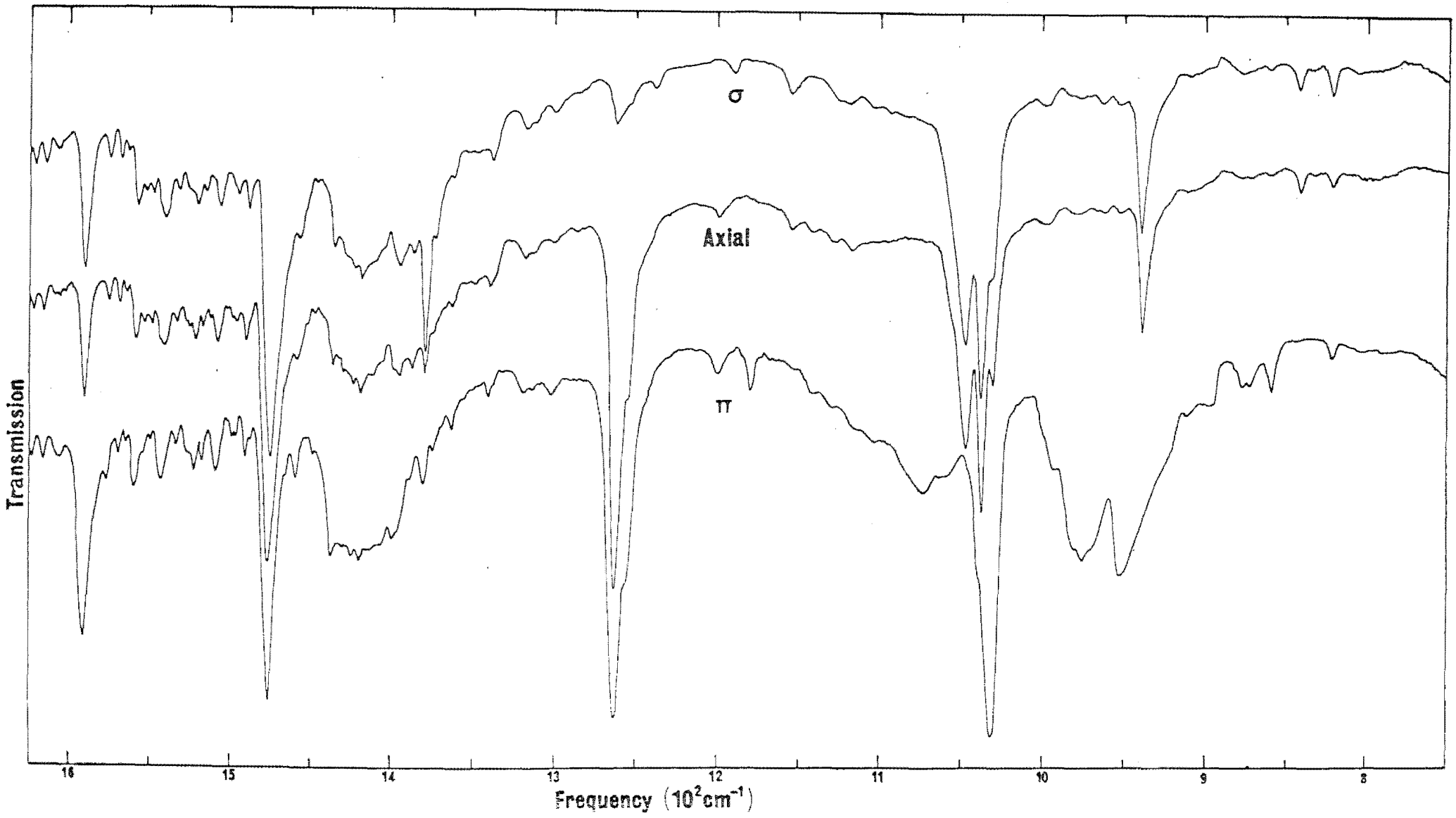

Fig. 6-3: Polarized infrared spectra of $CsMgCl_3$:Co 1.0 wt. % measured at 15°K

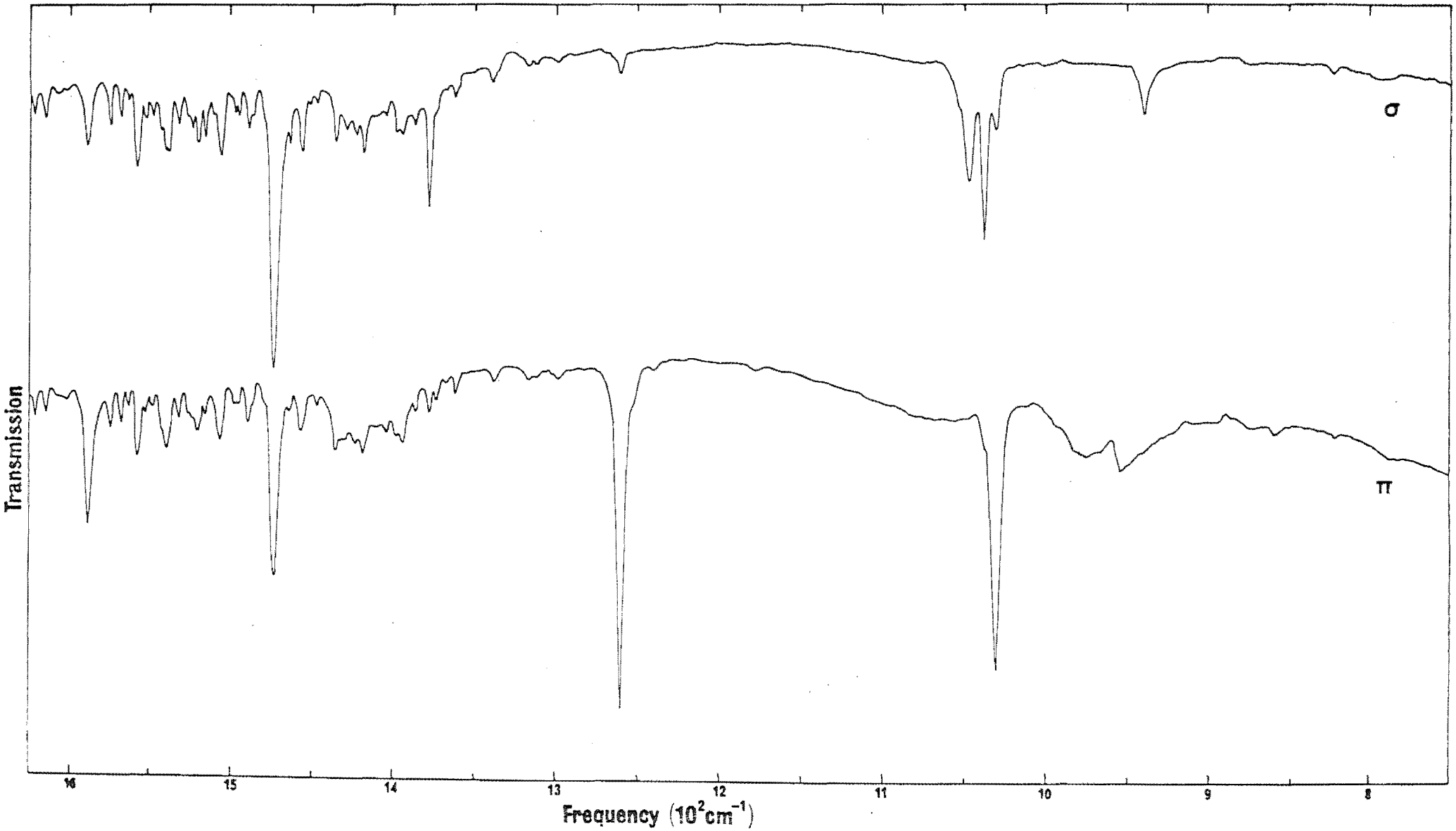

TABLE 6-1: Infrared data of $CsMgCl_3$:Co 2.0wt.% measured at 80°K. All measurements are in cm^{-1}.

Axial		σ		π	
Frequency	Width	Frequency	Width	Frequency	Width
-	-	-	-	773 ±2	-
789 ±2	-	789 ±2	-	788 ±1	9
826 ±1	7	826 ±1	8	826 ±1	7
846 ±1	-	846 ±1	-	-	-
-	-	-	-	863 ±1	24
-	-	-	-	878 ±1	
943.0±0.8	10	943.0±0.8	10	-	-
-	-	-	-	956 ±2	64
-	-	-	-	980 ±3	
-	-	-	-	1034.5±0.5	7
1042.0±0.7	24	1042.0±0.7	23	-	-
1051.5±0.7		1051.5±0.7		-	-
1148 ±1	-	1148 ±1	-	-	-
-	-	-	-	1184 ±1	-
1264.0±0.5	7	1264 ±1	13	1264.0±0.5	7
-	-	1380.5±0.7	6	-	-
1415 ±8	66	1415 ±8	65	1415 ±8	53
1476.0±0.7	9	1476.0±0.7	8	1476.0±0.7	8
1591.0±0.7	8	1591.5±0.7	8	1591.5±0.7	8

TABLE 6-2: Infrared data on $CsMgCl_3$:Co 2.0wt.% measured at 15°K

Axial			σ			π		
Freq(cm^{-1})	Width(cm^{-1})	Int(cm^{-2})	Freq(cm^{-1})	Width(cm^{-1})	Int(cm^{-2})	Freq(cm^{-1})	Width(cm^{-1})	Int(cm^{-2})
822.0±0.7	4	0.2	822.0±0.7	6	0.5	822.0±0.7	4	0.2
843.0±0.7	5.5	0.3	843.0±0.7	5	0.3	860.0±0.7	6	0.8
-			-			873 ±1	10	
-			-			878 ±1		
941.0±0.5	6.5	3.1	941.0±0.5	7	3.7	898 ±1		
-			-			953 ±1	58	
-			-			977 ±2		
-			-			995 ±1		
1000.0±1			1000.0±1			1032.3±0.5	4.0	8.6
1039.1±0.5	22		1039.1+0.5	21		1061 ±2	103	
1048.2±0.7			1048.2±0.7			1074 ±2		
1118 ±1			1123 ±3			1118 ±1		
1130 ±2			-			1130 ±2		
1143 ±2			-			1143 ±2		
1155 ±1			1155 ±1	8	0.5	1179 ±1	5	0.6
1200 ±1	9	0.5	1192 ±1	4	0.2	1200 ±1	10	0.8
1241 ±1			1241 ±1			1241 ±1		
1256 ±1			-			1256 ±1		
1262.5±0.5	2.9[a]	8.3[a]	1263 ±1	5	0.5	1262.5±0.5	4.4	18.8
1379.0±0.7	3	0.5	1379.0±0.5	4.0	3.8	1379.0±0.7	3	0.5
1390 ±5	68		1390 ±5	51		1415 ±8	67	
1420 ±5			1420 ±5			-		
1474.6±0.5	4.2[a]	5.6[a]	1474.6±0.5	3.8	15.4	1474.6±0.5	4.5	11.2
1591.0±0.5	4.8	2.5	1591.0±0.5	5.8	3.3	1591.0±0.5	6.5	7.6

a: Data obtained from $CsMgCl_3$:1.0wt.%Co.

σ polarization spectra have the E vector of the incident radiation normal to the crystal c axis.

In general, the 80°K spectrum (Fig. 6-1) resembles that of the axial. The differences in the intensities of the 1380 and 1264 cm^{-1} lines are the main dissimilarity of the two spectra. In the σ spectrum, the former line has a greater intensity while the latter line is weaker. In Fig. 6-1 there are absorption lines in the π spectrum which are not present in the other two. These include the two pairs of lines at (773;788) and (863;878) cm^{-1} which are located symmetrically on the opposite sides of the 826 cm^{-1} line with their separations from it being 37 and 52 cm^{-1}. Among the lines which are only present in the π spectrum are the strong, narrow line at 1034.5 cm^{-1}, the broader lines at 956 and 980 cm^{-1} and a weak line at 1184 cm^{-1}. The 1591.5 cm^{-1} line gains in intensity in going from the axial to the π spectrum while the reverse is the case for the 1476 cm^{-1} line.

On cooling to 15°K, the lines narrowed and shifted to lower frequencies. Several additional weak structures not observed at 80°K now appeared. These include the 1123, 1155, 1192 cm^{-1} lines in the σ spectrum and the 1118, 1130, 1143, 1179 and 1200 cm^{-1} lines in the π spectrum. In contrast the 1148, 1184 and the (773;788) cm^{-1} lines of the 80°K spectra have now disappeared. The 1262.5 cm^{-1} line in the π spectrum has an asymmetric profile due to a weak shoulder at 1256 cm^{-1}. A weak side-band appeared on the 1039.0 cm^{-1} line of the σ spectrum. Reference to Figs. 6-2 and 6-3 shows that it is in fact the remnant of the intense π-polarized 1032.3 cm^{-1} line. The intensity of this line gives an indication of the degree of misalignment of the crystal c axis with the infrared radiation.

The 848 cm^{-1} line, observed by Raman scattering, does not appear in any of the infrared spectra.

6.3.2 $CsCdCl_3$:Co

An investigation of $CsCdCl_3$ crystals containing nominal concentrations of 0 to 10 molar % of $CsCoCl_3$ was carried out at liquid nitrogen and liquid helium temperatures. The spectra obtained were found to be similar for the different cobalt ion concentrations.

Axial Spectra

Low temperature axial spectra are shown in Figs. 6-4 and 6-5 while Tables 6-3 and 6-4 list the frequencies and intensities of the absorption bands observed.

Two intense, sharp lines of frequencies 876.0 and 950.5 cm^{-1} are the dominant features of the 80°K spectrum. The other bands observed are much weaker and only one weak band was seen between the two major lines. Except for the 670 cm^{-1} line due to atmospheric carbon dioxide, no absorption was observed in the region below the 876.0 cm^{-1} line down to the absorption edge of the host lattice at 450 cm^{-1}. In the high energy portion of the spectrum lie two broad bands centered at 1070 and 1165 cm^{-1} and two narrower bands at 1030 and 1110 cm^{-1}.

When the crystals were cooled to 15°K, the bands revealed some fine structure while the lines became sharper and shifted to lower frequencies. The two main lines have peaks at new frequencies of 871.2 and 946.1 cm^{-1}. The 1030 cm^{-1} band was resolved into two narrower lines of frequencies 1024.6 and 1030.0 cm^{-1} while the 1110 cm^{-1} band sharpened and shifted to 1105.5 cm^{-1}. The broad band has fine structure with peaks at 1054, 1060, 1066 and 1075 cm^{-1}. Additional new absorptions were also observed. Among them are bands centred at 1134 and 1225 cm^{-1} and a sharp but weak satellite line at 878.5 cm^{-1}

Polarized Spectra

The results of infrared polarization studies are presented in

Fig. 6-4: $80^{\circ}K$ axial infrared spectrum of $CsCdCl_3$:Co 5 mole %

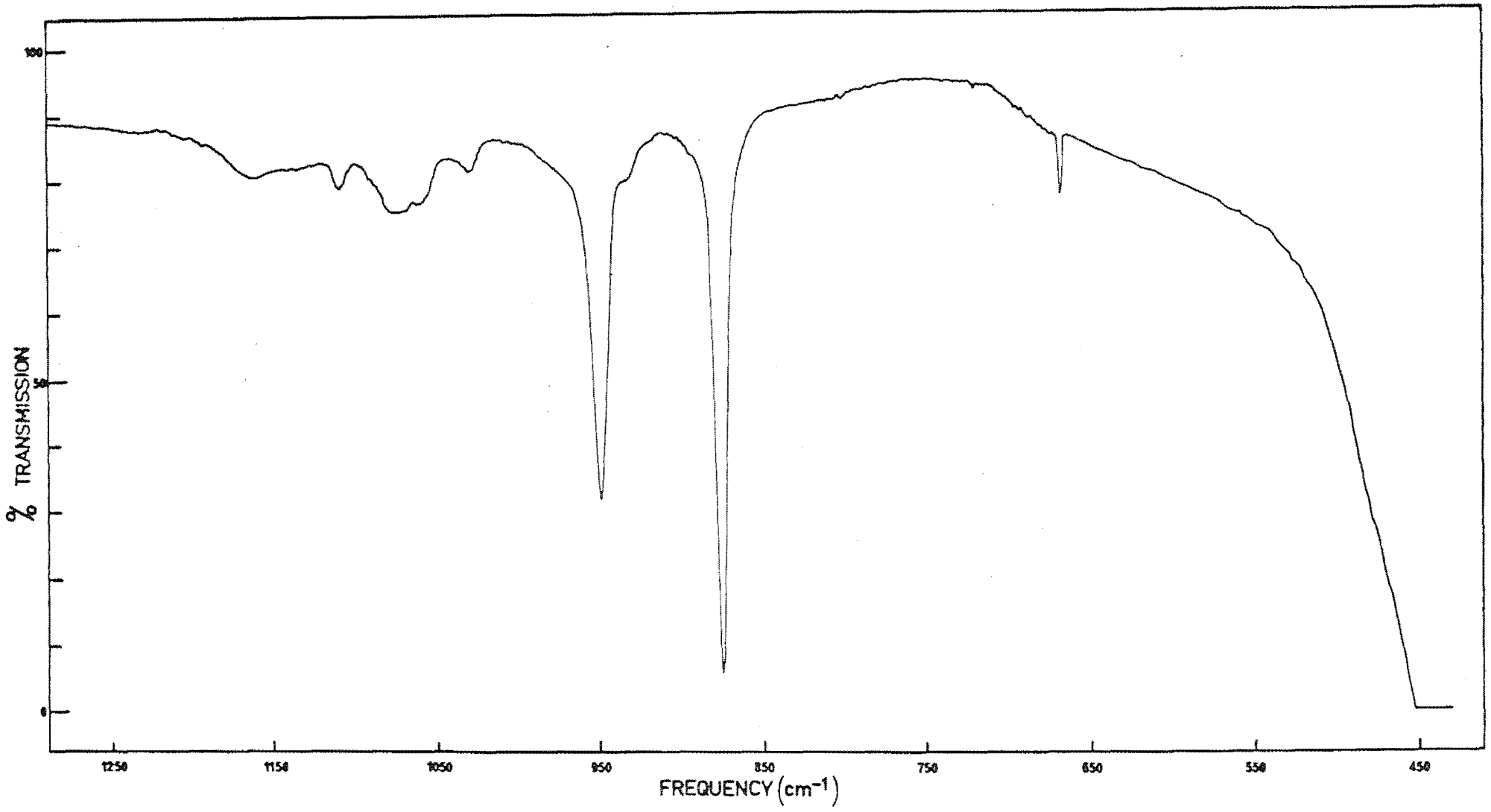

Fig. 6-5: $15^{\circ}K$ axial and polarized infrared spectra of $CsCdCl_3$:Co 5 mole %

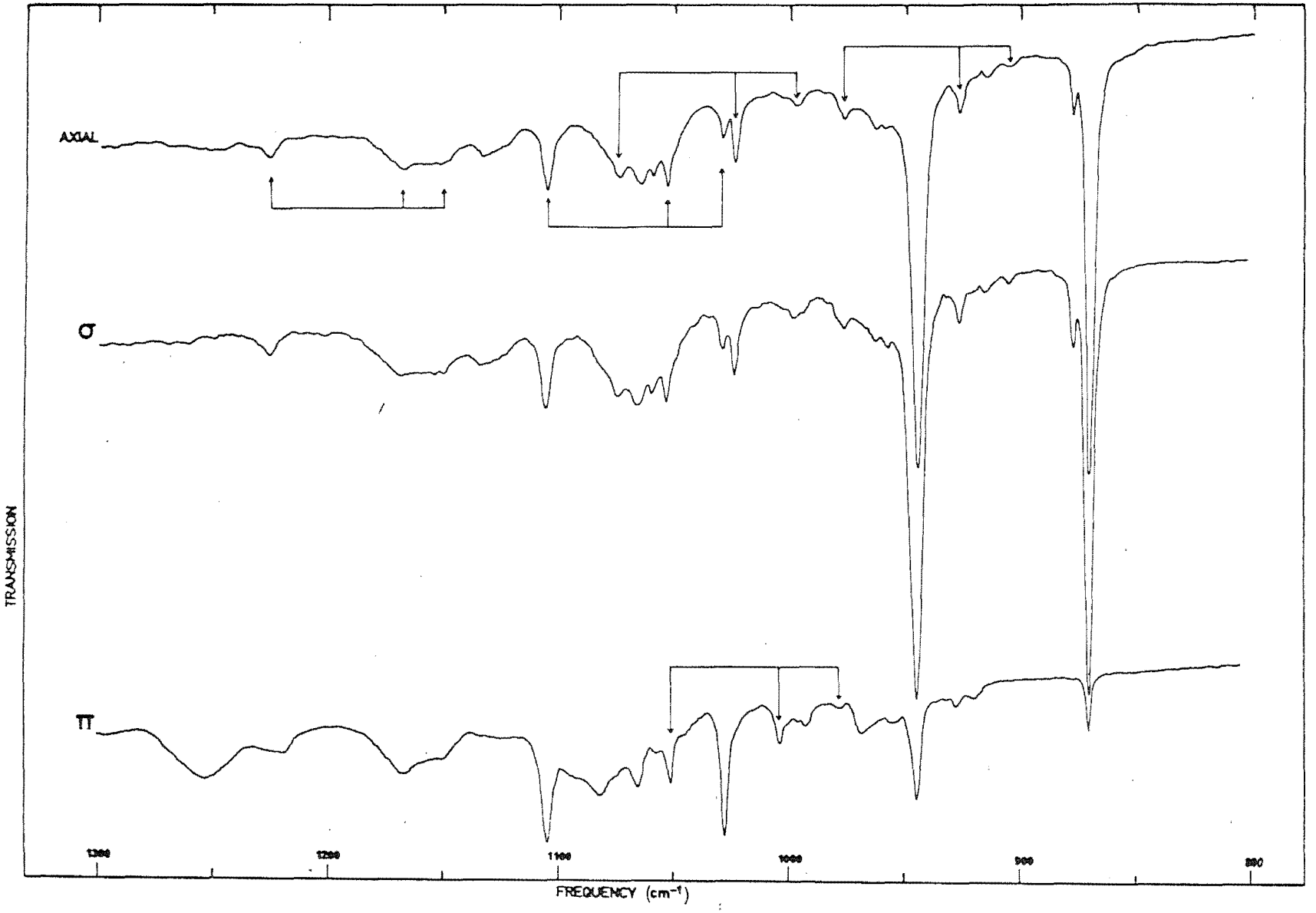

TABLE 6-3: $80^{\circ}K$ infrared data on $CsCdCl_3$ crystals containing nominal concentrations of 5mole% of $CsCoCl_3$.

Axial			σ		π		
Freq.[a] (cm^{-1})	Width (cm^{-1})	Int.[b] (cm^{-2})	Width (cm^{-1})	Int. (cm^{-2})	Freq. (cm^{-1})	Width (cm^{-1})	Int. (cm^{-2})
876.2±0.5	4.0	7.5	3.8	6.0	877±1	7	0.4
932 ±3	-		-	-			
950.5±0.5	8.3	5.6	8.0	5.4	951±1	10	1.0
1031 ±2	-	-	-	-	1035±2	9	1.0
1058 ±3	-	-	-	-			
1075 ±5	-	-	-	-	1080±5	-	-
1111 ±2	-	-	-	-	1111±2	-	-
1165 ±7	-	-	-	-			

a: The frequencies are for both the Axial and σ spectra.

b: Int = Width(cm^{-1}) x Peak Absorbance for 1 cm thickness.

TABLE 6-4: Infrared data on $CsCdCl_3$:Co 5 mole % measured at 15°K.

Axial			σ		π		
Freq.(cm^{-1})	Width(cm^{-1})	Int(cm^{-2})	Width(cm^{-1})	Int(cm^{-2})	Freq.(cm^{-1})	Width(cm^{-1})	Int.(cm^{-2})
871.2±0.4	1.5	6.0	2.1	5.2	871.2±0.5	2.2	0.3
878.3±0.5			-		-		
905 ±1			-		-		
916 ±1			-		922 ±1		
928.0±0.5			-		928 ±1		
946.1±0.4	3.1	5.4	2.7	7.1	946.1±0.5	4.0	1.0
958 ±1			-		958 ±1		
964 ±1			-		970 ±1		
978 ±1			-		980 ±1		
999 ±2			-		995 ±1		
1024.6±0.5	3.5	0.6	3.5	0.6	1006.0±0.7		
1030 ±1			-		1029.5±0.5	3.5	1.3
1054 ±0.5	32		33		1052.0±0.6		
1060 ±1					-		
1066 ±1					1066.0±0.7		
1075 ±1					1082 ±2		
1105.5±0.5	4.0	0.8	4.8	0.9	1105.5±0.5	5.3	1.8
1133 ±3			-		-		
1150 ±3	36		36		1150 ±3	32	
1168 ±3					1168 ±3		
1225 ±2			-		1225 ±3		
-			-		1255 ±3	28	

Fig. 6-5 with Tables 6-3 and 6-4 containing the experimental data. The figure shows that the σ spectrum is similar to the axial one, whereas the π spectrum differs from the axial spectrum. The two strongest lines that appear in both the axial and σ spectra are noticeably reduced in intensity in the π spectrum. The 1029.5 and 1105.5 cm^{-1} lines increase in intensity in going from the axial to the π spectrum. Additional lines at 922, 970, 980, 1006, 1052, 1082 cm^{-1} and a broad band centred at 1255 cm^{-1} also appear in the π spectrum.

6.4 ANALYSIS OF THE INFRARED SPECTRA

6.4.1 $CsMgCl_3$:Co

Electronic Transitions

In Sec. 4.4 the complete set of five electronic transitions of single cobalt ions detected by Raman scattering was given. Of these only the highest three electronic lines were observed by infrared absorption. The remaining two transitions are obscured by the intense reststrahlen absorption band of the $CsMgCl_3$ crystal. The coincidence of the axial and π spectra of the three electronic lines observed shows their magnetic dipole character[34].

Selection rules for the magnetic dipole transitions of a cobalt ion in the D_{3d} site of $CsMgCl_3$ can be derived as follows. All the electronic transitions of interest originate from a $\gamma_4^+(\Gamma_6^+)$ ground state and terminate on excited states of either $\gamma_4^+(\Gamma_7^+$ or $\Gamma_8'^+)$ or $\gamma_{5,6}^+(\Gamma_8'^+)$ symmetry (Sec. 2.2). The z and (x,y) components of the magnetic dipole operator transform as the γ_2^+ and γ_3^+ irreps, respectively, of the D_{3d} double group. From the following direct products

$$\gamma_4^+ \times \gamma_2^+ = \gamma_4^+$$
$$\gamma_4^+ \times \gamma_3^+ = \gamma_4^+ + (\gamma_5^+ + \gamma_6^+) \qquad (6.1)$$

it is evident that electronic transitions to the $\gamma_{5,6}^{+}$ states are absent in the σ spectrum (Sec. 2.2). Because the 1262.5 cm^{-1} line has only a remnant absorption in the σ spectrum, it is identified as the transition to the $\gamma_{5,6}^{+}(\Gamma_8'^{+})$ state. The 822.0 and 1379.0 cm^{-1} lines appear in both the σ and π spectra and are therefore assigned as transitions to the $\gamma_4^{+}(\Gamma_8'^{+})$ and $\gamma_4^{+}(\Gamma_7^{+})$ levels respectively.

The crystal field theory, described in Chapter II, can be used to calculate the intensities of these electronic transitions as follows.

The oscillator strength, f, of a magnetic dipole transition between two electronic states $|g\rangle$ and $|e\rangle$ is given by[35]

$$f = 1.21 \times 10^{-10}\, n\nu \left| \langle g | L_i + 2S_i | e \rangle \right|^2 \qquad (6.2)$$

where n is the refractive index of the crystal at transition frequency ν (cm^{-1}) and L_i and S_i are the components of the orbital and spin angular momenta respectively. The matrix elements of $(L_z + 2S_z)$ and $(L_x + 2S_x)$ may be obtained by evaluating these operators between the six levels of the $^4T_{1g}$ cubic field ground term. These levels are characterized by the eigenvectors of the twelve lowest levels of the full 120 dimension free-ion and crystal field matrices of the $3d^3$ configuration.

Experimentally the oscillator strength f, of a Gaussian line can be evaluated by using the following relation[36]

$$f = \frac{0.87 \times 10^{17}}{N} \left(\frac{n}{n^2+2}\right)^2 \mu_{ab} V_{ab} \qquad (6.3)$$

where N is the number of absorbing ions/cm^3, n is the refractive index of the crystal, μ_{ab} is the peak absorbance of the line in cm^{-1} and V_{ab} is the width of the line in eV. A Lorentzian line of the same peak absorbance and width has an oscillator strength a factor of approximately 1.5 greater. In order to calculate N, the actual concentration of cobalt ions in the crystals used has to be known. A

check on the nominal doping was done by comparing the peak absorbance of the $^4T_{1g}(^4P)$ bands for a solution containing a known weight of the doped crystals with that for a $CsCoCl_3$ solution of known concentration. In general the nominal dopings were close to that measured in this way. The value of the refractive index, n, for $CsMgCl_3$ was taken to be 1.7 as for $MgCl_2$ [32].

Table 6-5 gives a comparison of the experimental and computed oscillator strengths of the three electronic transitions observed. The reasonable agreement between the two sets of values confirms the assignment of these transitions and their magnetic dipole origin.

Besides the single cobalt ion lines observed, absorption due to cobalt ion pairs and clusters also appear in the spectra. The intensities of the lines due to cobalt ion pairs have a quadratic dependence on the cobalt ion concentration, while that due to more complex clusters have a more rapidly varying dependence. The intensities of the lines at 843 and 1256 cm^{-1} show a greater than linear dependence on the cobalt ion concentration. They are therefore attributed to clusters of at least two cobalt ions. These two lines seen at concentrations of 1.5% and above are not present in the spectra of $CsMgCl_3$:Co 1 wt. % shown in Fig. 6-3.

Vibronic Transitions

The vibronic bands have a wide range of widths and intensities. Their frequencies are listed in Table 6-6 together with those of their electronic parent lines and the corresponding vibronic intervals.

In $CsMgCl_3$:Co, odd vibrations can couple to the even electronic wavefunctions giving rise to electric dipole polarized vibronic transitions. This is substantiated by the coincidence of the axial and σ polarised traces of the vibronic bands observed. Some of these bands such as those at 860 and 1032.3 cm^{-1} appear only in the π spectrum.

TABLE 6-5: Computed and experimental oscillator strengths for assigned IR transitions in $CsMgCl_3$:Co 2% at 15°K

Assignment	Experimental Frequency (cm^{-1})	Oscillator Strength (10^{-10}) σ Expt.	σ Compt.	π Expt.	π Compt.
$\gamma_4^+(\Gamma_7^+)$	1379.0	155	892	20	75
$\gamma_{5,6}^+(\Gamma_8'^+)$	1262.5	21	0	868	5834
$\gamma_4^+(\Gamma_8'^+)$	822.0	20.9	30.7	6.9	3.9
$\gamma_{5,6}^+(\Gamma_8^+)$	-	-	0	-	2305
$\gamma_4^+(\Gamma_8^+)$	-	-	2927		3301

TABLE 6-6: Analysis of vibronic bands of $CsMgCl_3$:Co 2.0wt.% to give frequencies (cm^{-1}) of peaks in the phonon density of states.

Temp.	Electronic Parent	Vibronic	Vibronic Interval
	826 ±1	788 ±1	-38 ±2
		863 ±1	37 ±2
		773 ±2	-53 ±3[a]
80°K		878 ±1	52 ±2[a]
	1264.0±0.5	1148 ±1	-116 ±2
		1380.5±0.7	116.5±1.2
	822.0±0.7	860.0±0.7	38.0±1.4
		873 ±1	51 ±2[a]
		941.0±0.5	119.0±1.2
		953 ±1	131 ±2[a]
		977 ±2	155 ±3
15°K		1032.3±0.5	210.3±1.2
		1039.1±0.5	217.1±1.2
		1048.2±0.7	226.2±1.4
	1262.5±0.5	1379.0±0.5	116.4±1.0
		1390 ±5	128 ±6[a]
		1420 ±5	158 ±6
		1474.6±0.5	212.1±1.0
	1379.0±0.5	1591.0±0.5	212.0±1.0

a: cf. Raman phonon lines of Table 4-1.

Of particular interest are the two pairs of lines (773;788) cm^{-1} and (863;878) cm^{-1} located symmetrically about the $\gamma_4^+(\Gamma_8'^+)$ electronic line of the 80°K spectrum of Fig. 6-1. The former two lines are difference lines while the latter two lines are the summation lines. Vibronic difference lines are temperature dependent and have vanishing intensities at low temperatures due to depopulation of the vibronic levels above the ground state. They are known as hot bands for this reason. The (773;788) cm^{-1} pair and the 1148 cm^{-1} lines are examples of hot bands as they disappear at liquid helium temperatures. The corresponding summation line for the 1148 cm^{-1} line happens to coincide with the $\gamma_4^+(\Gamma_7^+)$ electronic line at 1379.0 cm^{-1} which is principally magnetic dipole polarized.

Reference to Table 6-6 shows that only one complete set of three vibronic lines, corresponding to a vibronic interval of 211 cm^{-1}, was identified for the three electronic transitions observed. The intensities of the vibronic bands in any one set, associated with the $\gamma_4^+(\Gamma_8'^+)$, $\gamma_{5,6}^+(\Gamma_8'^+)$ and $\gamma_4^+(\Gamma_7^+)$ levels have decreasing magnitudes in the order listed. The number of the identified vibronic bands associated with the $\gamma_{5,6}^+(\Gamma_8'^+)$ and $\gamma_4^+(\Gamma_7^+)$ electronic parents is in each case less than that associated with the $\gamma_4^+(\Gamma_8'^+)$ level. The non-observation of the missing vibronic bands could be due to their weak intensity or their masking by water vapour absorption lines.

The vibronic intervals are attributed to peaks in the phonon density of states for $CsMgCl_3$. Of the seven vibronic intervals identified only two have frequencies corresponding to the $\underline{k} = 0$ Raman phonons.

A check on the assignment of the vibronic bands to particular electronic parent lines can be made by studying their behaviour under an applied magnetic field. Such studies will be described in the following chapter.

6.4.2 $CsCdCl_3$:Co

Electronic Transitions

An assignment of the single cobalt ion transitions due to the Raman scattering of $CsCdCl_3$:Co was made earlier in Sec. 4.4. Of the total of four electronic Raman lines observed, three were attributed to Co(2) ions while the remaining line at 897 cm^{-1} was identified as the unresolved $\Gamma_8'^{+}$ doublet of the Co(1) ion.

The infrared lines at 871.2 and 946.1 cm^{-1} match the frequencies of the 873 and 947 cm^{-1} Raman lines and are therefore assigned as the trigonal crystal field split components of the Γ_8' doublet of the Co(2) ions. These ions are in C_{3v} sites and hence electric dipole transitons between levels of the $^4T_{1g}(^4F)$ cubic field term are allowed. This assignment is consistent with the coincidence of the axial and σ spectra of these electronic lines[34].

States in the $3d^6 4p$ configuration are admixed with those of the same symmetry representations in the $3d^7$ configuration by the odd terms of the trigonal C_{3v} crystal field. Some odd character is thus gained by the γ_4 and $\gamma_{5,6}$ states, of interest, of the Co(2) ions. The z and (x,y) components of the electric dipole transition operator transform as the respective γ_2 and γ_3 irreps of the C_{3v} double group. The direct product representations

$$\gamma_4 \times \gamma_2 = \gamma_4$$
$$\gamma_4 \times \gamma_3 = \gamma_4 + (\gamma_5 + \gamma_6) \qquad (6.4)$$

show that (Sec. 2-2) the absorption intensity for the $\gamma_4 \rightarrow \gamma_{5,6}$ transitions is zero in the π spectrum as $\gamma_4 \times \gamma_2$ does not contain $\gamma_{5,6}$. This selection rule can be utilized to identify the trigonal crystal field component γ_4 and $\gamma_{5,6}$ states of the Γ_8' doublet. Reference to the π spectrum of Fig. 6-5 however reveals that the intensities of both

these electronic lines are greatly reduced and an unambiguous identification cannot be made. Zeeman-infrared studies carried out on these lines (Chapter VII) substantiated their labelling determined earlier from the results of the polarization Raman scattering experiments (Chapter IV). Due to a lack of information on the $3d^6 4p$ configuration of the cobalt ion, the electric dipole intensities of the electronic transitions of the Co(2) ion could not be calculated.

None of the other three electronic transitions of the Co(2) ion were observed. The lowest two electronic lines have predicted frequencies of 291 and 396 cm^{-1} and would lie under the intense reststrahlen band of the $CsCdCl_3$ host. In analogy to the case of $CdCl_2$:Co, it is likely that the $\gamma_4(\Gamma_7)$ state of Co(2) was not observed because of its weak intensity[37].

None of the electronic transitions of the Co(1) ion was detected. One of them has been found by Raman scattering to have a frequency of 897 cm^{-1}. It was attributed as the transition to the unsplit $\Gamma_8'^+$ doublet. The existence of this level can be inferred from the positions of its vibronic bands in the infrared spectra. Non-observation of any of the electronic lines of the Co(1) ions can be partially ascribed to their relatively low concentrations (Sec. 4.4) and partially to the necessarily weak magnetic dipole absorptions for these ions which are in D_{3d} sites.

Vibronic Transitions

The most striking feature in the axial and σ spectra is the two electronic lines. It is only in the π spectrum that the vibronic bands have intensities comparable to those of the electronic transitions. The electric dipole nature of the vibrationally induced bands is shown by the matching of the axial with the σ spectrum. Some of these bands can only be accounted for by the existence of the electronic transition

TABLE 6-7: Analysis of vibronic bands in $CsCdCl_3$:Co 5 mole % to give frequencies (cm^{-1}) of peaks in the phonon density of states at 15°K.

Electronic parent	Vibronic	Vibronic Interval
Co(2)		
871.2±0.4	905 ±1	34 ±1
	980 ±1[a]	109 ±1
	999 ±1	128 ±1[c]
	1029.5±0.5	158.3±0.9[c]
	1150 ±3	279 ±3
946.2±0.4	978 ±1	32 ±1
	1052.0±0.6[a]	105.8±1.0
	1075 ±1	129 ±1[c]
	1105.5±0.5	159.4±0.9[c]
	1225 ±2	279 ±2
Co(1)		
897 ±2[b]	928 ±0.5	31 ±3
	1006.0±0.7[a]	109 ±3
	1024.6±0.5	128 ±3[c]
	1054.0±0.5	157 ±3[c]
	1168 ±3	271 ±5

a: Appear only in π spectrum.

b: Raman data (Table 4-2); not seen in the infrared spectra.

c: cf. Raman phonon lines of Table 4-1.

to the $\Gamma_8'^+$ doublet of the Co(1) ion. Sets of three vibronic bands associated with the three electronic parent levels were found and are indicated by arrows in Fig. 6-5. In any one set the vibronic band associated with the $\gamma_4(\Gamma_8')$ level of the Co(2) ion is the weakest while the other two bands have comparable intensities. The strongest set corresponds to an energy separation of 158 cm^{-1}.

The results are presented in Table 6-7. Two of the vibronic intervals coincide with two of the $\underline{k} = 0$ Raman phonons listed in Table 4-1.

CHAPTER VII

ZEEMAN-INFRARED STUDIES.

7.1 INTRODUCTION

Although Zeeman-optical results of cobalt ions have been reported[38], no such studies in the infrared region have appeared in the literature. In the preceding chapter, the electronic and vibronic lines of $CsMgCl_3$:Co and $CsCdCl_3$:Co were often found to be sharp and well isolated from each other. An obvious extension of the earlier infrared work is an investigation of these crystals under an applied magnetic field. Axial and polarized spectra of these crystals were recorded at magnetic field strengths of up to 40 kG. A discussion and analysis of the spectra obtained for $CsMgCl_3$:Co and $CsCdCl_3$:Co are individually presented in Sec. 7.3 and 7.4 respectively.

While only shifts were detected in the Zeeman-Raman spectra, the Zeeman-infrared experiments yielded both shifts and splittings of the electronic and vibronic lines. The Zeeman-infrared experimental arrangement has several advantages over that of the Zeeman-Raman. First, because the crystals examined are at a higher temperature in the former, the upper component of the zero-field ground state is not completely depopulated. Hence electronic Zeeman-infrared transitions that originate from this component are observable. Second, the Beckman IR12 spectrophotometer has a higher signal-to-noise ratio than the Raman system.

7.2 GENERAL

Crystals used in the Zeeman-infrared work were doped with less than 3 weight % of $CoCl_2$. This ensured that transitions due to clusters of cobalt ions and the inhomogeneous line broadening caused by neighbouring cobalt ions were both kept to a minimum. Specimens used had a mean thickness of 4.5 mm. As the field was generated by a superconducting

magnet, spectral runs were performed only at liquid helium temperatures with the crystal temperature estimated at 15°K (Sec. 3.3). All measurements were made at a slow scanning speed of 1.6 cm^{-1}/min., and an 8-second time constant. Owing to the simple solenoid magnet used, the applied field was always directed along the infrared radiation beam. This meant that only axial spectra could be measured when the field is directed along the crystal c axis ($\underline{H}\|\underline{c}$) while only σ and π polarization spectra could be recorded when the field is normal to the crystal c axis ($\underline{H}\perp\underline{c}$).

Zeeman-infrared measurements on the $\gamma_4^+(\Gamma_8'^+)$, $\gamma_{5,6}^+(\Gamma_8'^+)$ and $\gamma_4^+(\Gamma_7^+)$ levels of $CsMgCl_3$:Co and the $\gamma_4(\Gamma_8')$ and $\gamma_{5,6}(\Gamma_8')$ levels of $CsCdCl_3$:Co(2), together with their stronger vibronic bands were made. All the electronic lines examined split in the maximum field of 40 kG and these splittings are apparent in at least one of the spectra obtained. The biggest splitting observed was 17.2 cm^{-1} measured for the transition to the $\gamma_{5,6}(\Gamma_8')$ level of $CsCdCl_3$:Co(2) for $\underline{H}\|\underline{c}$. In contrast the transition to the $\gamma_{5,6}^+(\Gamma_8'^+)$ level of $CsMgCl_3$:Co only showed signs of an incipient splitting for $\underline{H}\|\underline{c}$ even at full field. The maximum number of resolved components detected for any one electronic line was three, and only occurred for the transition to the $\gamma_{5,6}(\Gamma_8')$ level of $CsCdCl_3$:Co(2). Upon subjecting the crystals to a 20 kG field, only two of the five electronic lines exhibited any apparent splittings. These are the transitions to the $\gamma_4^+(\Gamma_8'^+)$ and $\gamma_4^+(\Gamma_7^+)$ states of $CsMgCl_3$:Co. Marginal or zero shifts were recorded for the other electronic levels.

Experimental data from Zeeman-infrared studies can provide the g values of the excited electronic states. These studies can also help assign vibronic bands, as these have the same Zeeman pattern as their electronic parents. Impurity absorptions due to atmospheric water vapour and localized oxygen phonons, which plagued some of the spectra recorded, are unaffected by the magnetic field and so can readily be identified as such.

7.3 RESULTS

7.3.1 $CsMgCl_3$:Co

Zeeman measurements were made on $CsMgCl_3$ crystals doped with 1 to 2 weight % of $CoCl_2$. Portions of the axial and polarized spectra obtained are displayed in Figs. 7-1 to 7-7 while spectral data are listed in Tables 7-1 and 7-2. Fig. 6-2 shows that the electronic lines of $CsMgCl_3$:Co have greatly different strengths. While no difficulties were encountered in obtaining a strong line for the $\gamma_{5,6}^{+}(\Gamma_8'^{+})$ level for a 1% cobalt ion doping, the $\gamma_4^{+}(\Gamma_8'^{+})$ absorption proved to be too weak for a Zeeman study at this concentration even for the maximum crystal thickness of 5.5 cm. Hence the Zeeman effect on the $\gamma_4^{+}(\Gamma_8'^{+})$ level was measured using 2% cobalt ion concentrations, for which a sufficiently strong line due to this level was obtained.

Axial ($H \| c$) Spectra

At 20 kG, two of the zero-field electronic lines each split into two components. The $\gamma_4^{+}(\Gamma_8'^{+})$ line was marginally resolved into lines at 820 and 824 cm^{-1} as shown in Fig. 7-1. The $\gamma_4^{+}(\Gamma_7^{+})$ line split into two components of equal strength separated by 8.0 cm^{-1} (Fig. 7-6) while the $\gamma_{5,6}^{+}(\Gamma_8'^{+})$ line did not even shift (Fig. 7-4).

When the field was increased to its maximum strength of 40 kG, the $\gamma_4^{+}(\Gamma_8'^{+})$ line broadened and shifted up to 826 cm^{-1}. The 20 kG-resolved components of the $\gamma_4^{+}(\Gamma_7^{+})$ state were further pushed apart to 16.0 cm^{-1} at 40 kG, with the higher-energy component being twice as intense as the other. While no splitting or shift was observed for the $\gamma_{5,6}^{+}(\Gamma_8'^{+})$ state, it nevertheless broadened at 40 kG.

The 941.0, 1039.1, 1048.2, 1474.6 and 1591.0 cm^{-1} vibronic lines were selected for Zeeman studies because of their stronger and narrower profiles. The first three are associated with the $\gamma_4^{+}(\Gamma_8'^{+})$ electronic

Fig. 7-1: 15°K Zeeman-infrared spectra of $CsMgCl_3$:Co showing the $\gamma_4^+(\Gamma_8'^+)$ electronic line and its associated vibronic bands.

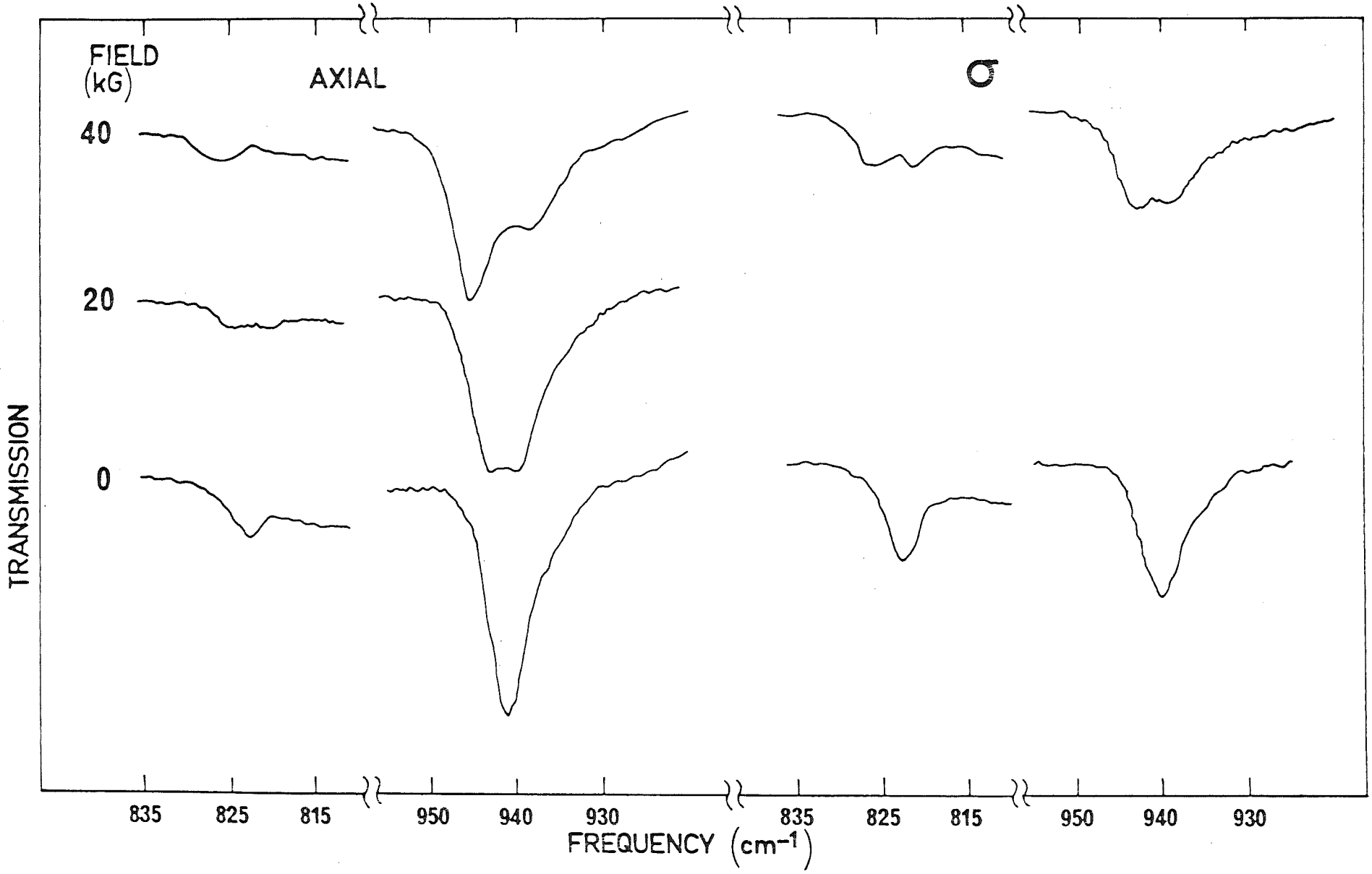

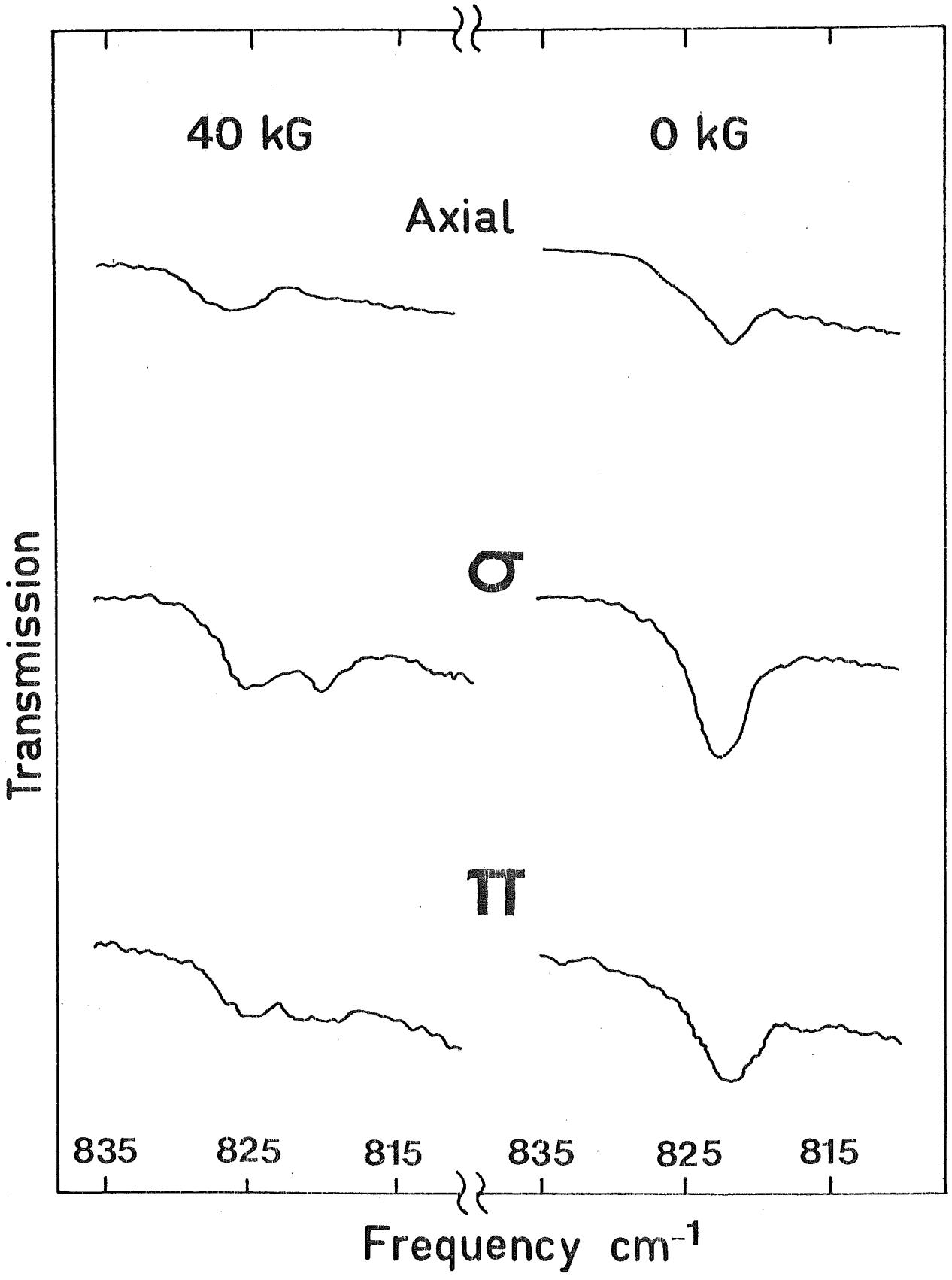

Fig. 7-2: Zeeman-infrared pattern of the $\gamma_4^+(\Gamma_8'^+)$ electronic state of $CsMgCl_3$:Co measured at 15°K.

Fig. 7-3: $15^{\circ}K$ Zeeman-infrared spectra of the vibronic bands associated with the $\gamma_4^+(\Gamma_8'^+)$ electronic level of $CsMgCl_3$:Co

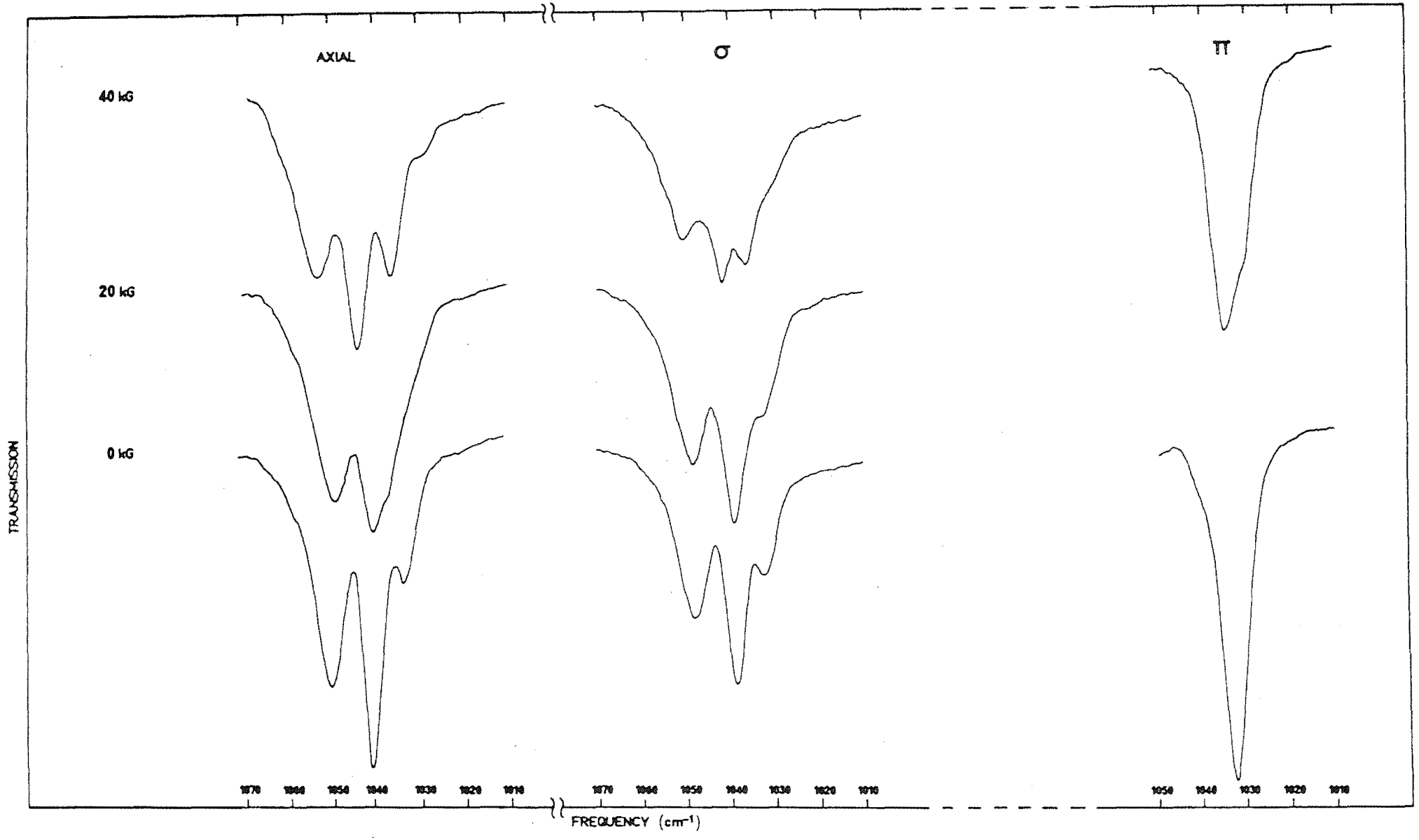

Fig. 7-4: $15^{\circ}K$ axial ($\underline{H} \parallel \underline{c}$) Zeeman-infrared spectra of the $\gamma_{5,6}^{+}(\Gamma_8'^{+})$ electronic state of $CsMgCl_3$:Co and its associated vibronic band

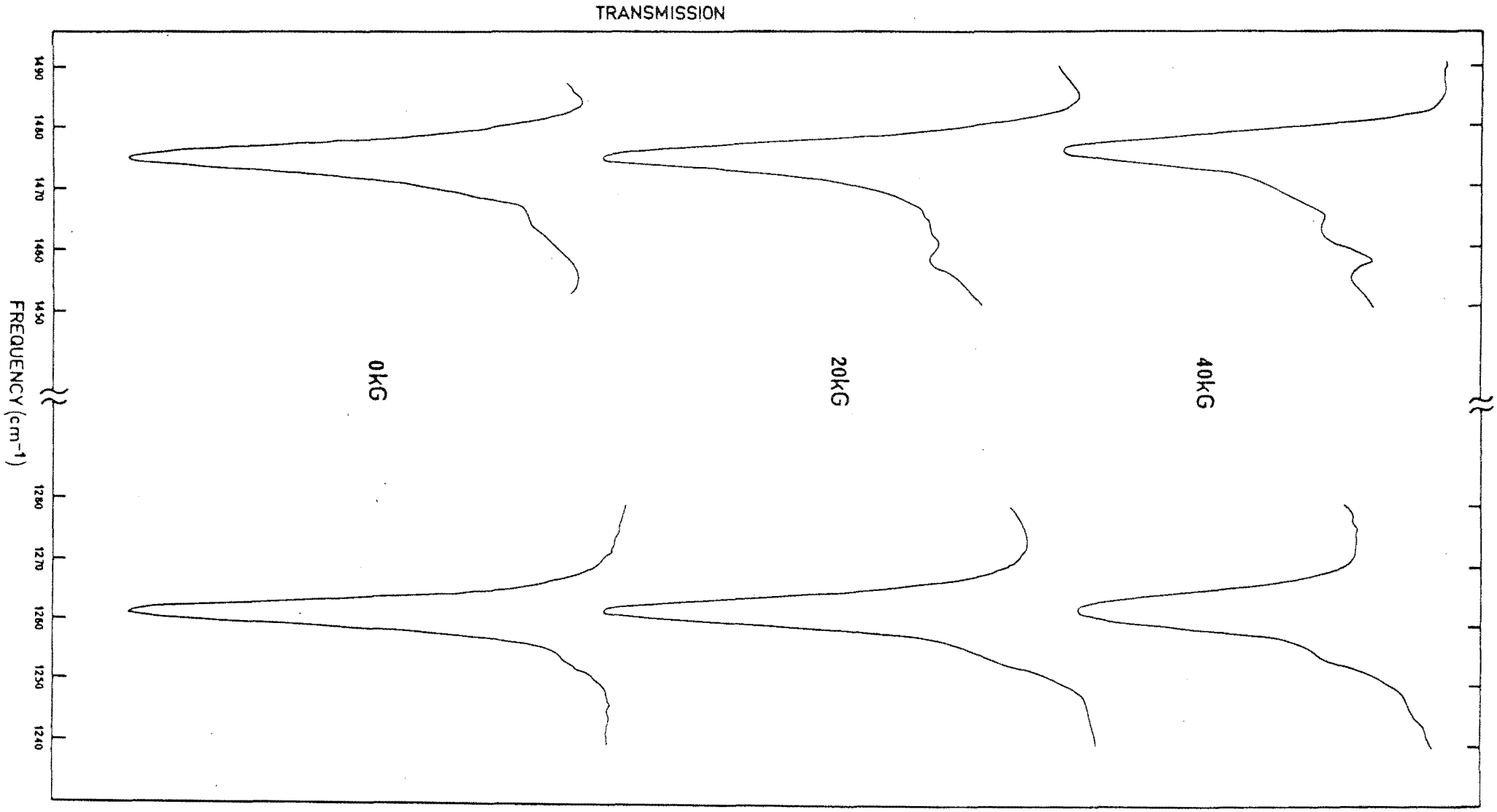

Fig. 7-5: $15^{o}K$ polarized ($\underline{H} \perp \underline{c}$) Zeeman-infrared spectra of the $\gamma_{5,6}^{+}(\Gamma_{8}'^{+})$ electronic state of $CsMgCl_3$:Co and its associated vibronic band

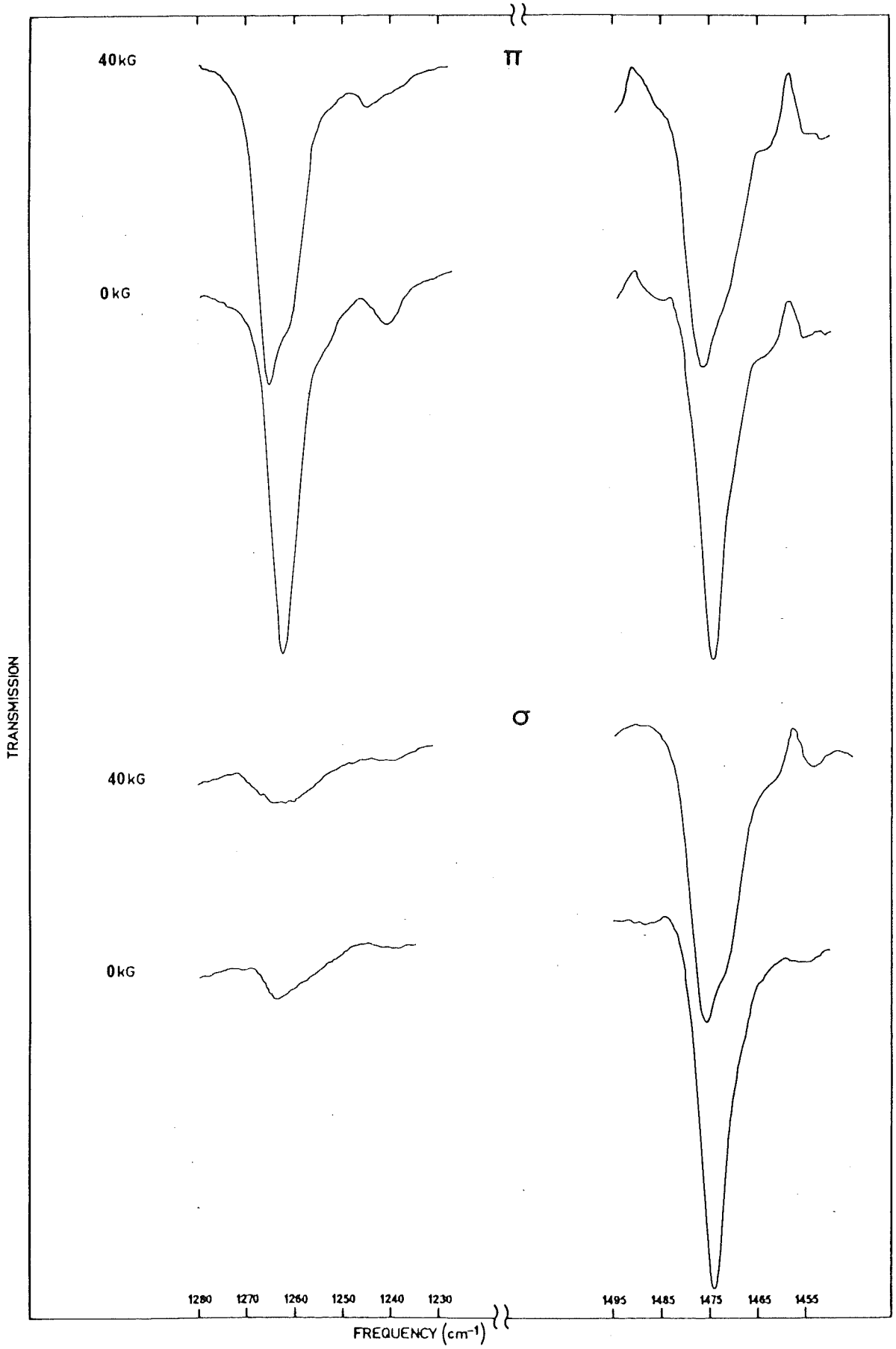

Fig. 7-6: 15^{o}K axial ($\underline{H} \parallel \underline{c}$) Zeeman-infrared spectra of the $\gamma_4^+(\Gamma_7^+)$ electronic state of $CsMgCl_3$:Co and its associated vibronic band

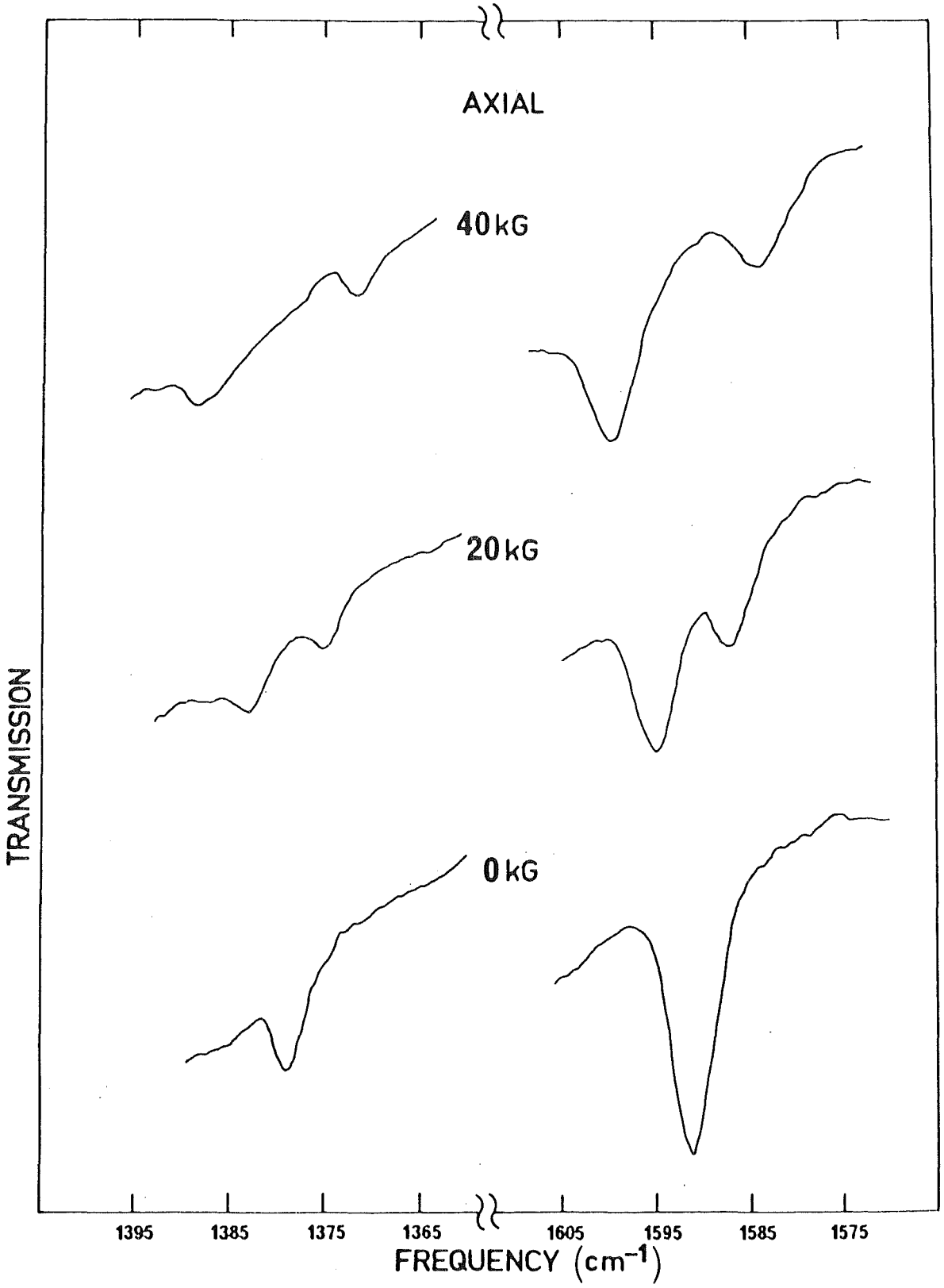

Fig. 7-7: 15°K polarized (H⊥c) Zeeman-infrared spectra of the $\gamma_4^+(\Gamma_7^+)$ electronic state of $CsMgCl_3$:Co and its associated vibronic band

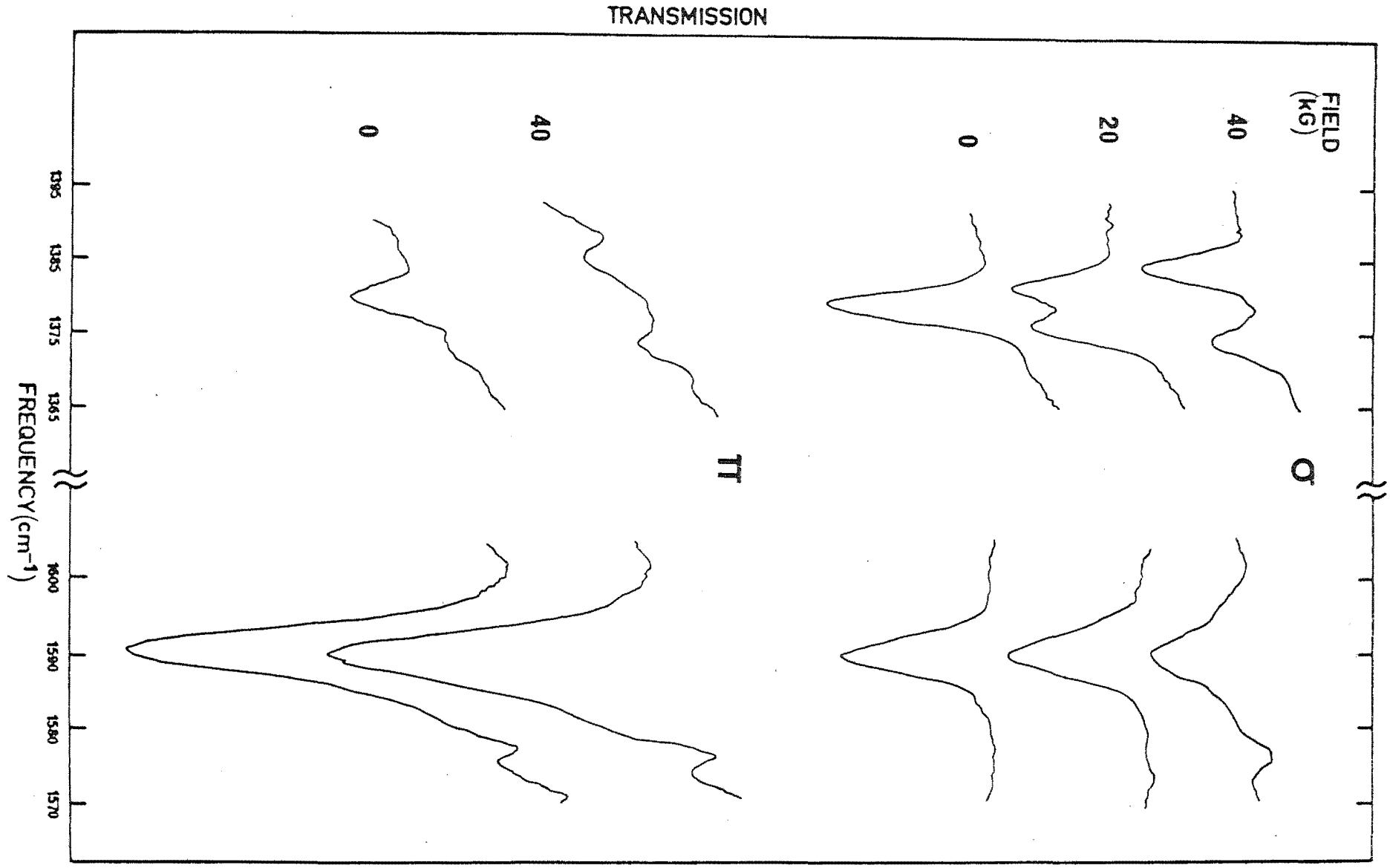

TABLE 7-1: Zeeman-infrared axial (H‖c) data on $CsMgCl_3$:Co 2.0wt.% at 15°K. The shifts are measured from the zero-field positions.

Frequency (cm^{-1})	20 kG Width (cm^{-1})	Shift (cm^{-1})
820 ±1	-	-2.0
824 ±1	-	2.0
939.5±0.8[a]	9	-1.5
943.0±0.8[a]		2.0
1037 ±1[a]	11	-2.1
1040.7±0.5[a]		1.6
1049.1±0.8[a]	8	0.9
1262.4±0.5*	3.7	-0.1
1375.5±0.5	2.5	-3.5
1383.5±0.8	3.8	4.5
1474.6±0.5[b,*]	4.4	0.0
1587.1±0.8[c]	5	-3.9
1594.9±0.5[c]	5	3.9
	40 kG	
826 ±1	4	4.0
938 ±1[a]	4.8	-3.0
945.0±0.5[a]		4.0
1029 ±1[a]	-	-3.3
1035.6±0.5[a]	4.4	-3.5
1043.1±0.5[a]	6.2	4.0
1052.0±0.8[a]	8	3.8
1263.0±0.8*	6.9	0.5
1371.5±0.5	3.5	-7.5
1387.5±0.8	4.5	8.5
1475.5±0.5[b,*]	5.7	0.9
1583.5±0.8[c]	6	-7.5
1599.0±0.5[c]	6.2	8.0

* : Data obtained from $CsMgCl_3$:Co 1.0wt.%

a,b,c: Vibronic absorptions associated with the $\gamma_4^+(\Gamma_8'^+)$, $\gamma_{5,6}^+(\Gamma_8'^+)$ and $\gamma_4^+(\Gamma_7^+)$ electronic parent levels respectively.
Each curly bracket indicates the split components of a zero-field line.

TABLE 7-2: Zeeman-infrared polarization (H⊥c) data on $CsMgCl_3$:Co 1.5wt.% at 15°K. The shifts are measured from the zero-field positions.

σ			π		
Frequency (cm^{-1})	Width (cm^{-1})	Shift (cm^{-1})	Frequency (cm^{-1})	Width (cm^{-1})	Shift (cm^{-1})
	40 kG			40 kG	
819.5±0.5*	4	-2.5	819 ±1*	-	-3.0
824.5±0.5*	5	2.5	824 ±1*	-	2.0
939 ±1[a]	11	-2.0	1030 ±1[a]	8.2	-2.3
943.5±0.8[a]		2.5	1034.6±0.5[a]		2.3
1036.6±0.8[a]	14	-2.5	-	-	-
1041.4±0.5[a]		2.3	-	-	-
1050.0±0.8[a]	6	1.8	1244 ±1	-	3
1263 ±2	13	0.5	1261 ±1	8.3	-1.5
			1264.6±0.5		2.1
1374.4±0.5	5.2	-4.6	1374 ±1	3	-5.0
1384.2±0.5	4.1	5.2	1384 ±1	3.5	5.0
1473 ±1[b]	10.3	-1.6	1472 ±1[b]	11.0	-2.6
1476.5±0.5[b]		1.9	1476.5±0.5[b]		1.9
1591.0±0.7[c]	9	0.0	1591.0±0.5[c]	8.2	0.0
	20 kG				
1039.4±0.5[a]	7	0.3			
1048.3±0.8[a]	8	0.1			
1376.5±0.5	4	-2.5			
1381.3±0.5	5	2.3			
1591.0±0.7[c]	7.1	0.0			

*Data obtained from $CsMgCl_3$:Co 2.0wt.%.
The footnote of Table 7-1 applies.

level and the remaining two with the $\gamma_{5,6}^{+}(\Gamma_8'^{+})$ and $\gamma_4^{+}(\Gamma_7^{+})$ electronic levels respectively.

Figs. 7-4 and 7-6 show that the Zeeman behaviour of the 1474.6 and 1591.0 cm^{-1} vibronic lines is analogous to that of their electronic parent levels.

The Zeeman effects of the 941.0, 1039.1 and 1048.2 cm^{-1} vibronic lines belonging to the $\gamma_4^{+}(\Gamma_8'^{+})$ electronic level are as follows. The 941.0 cm^{-1} line split into two components separated by 7 cm^{-1} at 40 kG (Fig. 7-1). The 0, 20 and 40 kG traces of the 1039.1 and 1048.2 cm^{-1} vibronic lines are shown in Fig. 7-3. Due to a slight misorientation of the crystal, the π-polarized 1032.3 cm^{-1} line has a remnant visible in the 0 kG spectrum. In a 20 kG field, both the vibronic lines broadened and moved further apart and peaked at 1040.7 and 1049.1 cm^{-1} with a weak shoulder appearing on the former line. At 40 kG the 1040.7 cm^{-1} line was resolved into two well-defined components at 1035.6 and 1043.1 cm^{-1}, while the 1049.1 cm^{-1} line shifted up to 1052.0 cm^{-1}.

Polarized (H⊥c) Spectra

When the crystals were exposed to a 40 kG field, each of the three electronic lines split into two components. Fig. 7-2 shows that in both the σ and π spectra, the components of the $\gamma_4^{+}(\Gamma_8'^{+})$ state are of equal intensity and are 5 cm^{-1} apart.

At 20 and 40 kG, the components of the $\gamma_4^{+}(\Gamma_7^{+})$ state are separated by 4.8 and 9.8 cm^{-1} respectively in the σ spectrum of Fig. 7-7. In the π spectrum recorded at 40 kG, the components appear as weaker absorptions with frequencies identical to their σ-polarized counterparts.

Fig. 7-5 of the π spectrum shows that at 40 kG the $\gamma_{5,6}^{+}(\Gamma_8'^{+})$ line experienced an incipient splitting, while only a broadening of its remnant absorption occurred in the σ spectrum.

Zeeman effects for the main polarized vibronic transitions observed are described below starting with the π spectrum measured at 40 kG. The π-polarized 1032.3 cm^{-1} vibronic line split into a main component which peaked at 1034.6 cm^{-1} and its side band at approximately 1030 cm^{-1} (Fig. 7-3). Their separation agrees well with that of 5 cm^{-1} measured for their $\gamma_4^+(\Gamma_8'^+)$ electronic parent level. The 1474.6 vibronic line associated with the $\gamma_{5,6}^+(\Gamma_8'^+)$ state was resolved into a 1476.5 cm^{-1} line and a weak shoulder at 1472 cm^{-1}. Unlike its $\gamma_4^+(\Gamma_7^+)$ electronic parent line which split at 40 kG, the 1591.0 cm^{-1} vibronic line only broadened in the same field as is shown in Fig. 7-7.

The σ spectrum is as follows. Three vibronic absorptions, of the $\gamma_4^+(\Gamma_8'^+)$ electronic state, at 941.0, 1039.1 and 1048.2 cm^{-1} were chosen for study. At 40 kG a mean splitting of 4.6 cm^{-1}, consistent with that of the electronic parent state, was recorded for both the first two lines while only a shift was observed for the third line (Figs. 7-1 and 7-3). In a 40 kG field the 1474.6 cm^{-1} vibronic line, associated with the $\gamma_{5,6}^+(\Gamma_8'^+)$ electronic state, experienced an incipient splitting (Fig. 7-5), while the 1591.0 cm^{-1} vibronic line associated with the $\gamma_4^+(\Gamma_7^+)$ electronic state just broadened (Fig. 7-7).

7.3.2 $CsCdCl_3$:Co(2)

Crystals used for this Zeeman work contained nominal doping of 1.0, 2.0 and 5.0 mole % of $CsCoCl_3$. Portions of typical axial and polarized spectra recorded are presented in Figs. 7-8 to 7-10, while the numerical results are summarized in Tables 7-3 and 7-4. The vibronic absorptions of $CsCdCl_3$:Co although sharp, are however in most cases too weak for Zeeman studies. The main set of vibronic lines examined is the one corresponding to a vibronic interval of 158 cm^{-1}. Only one of them visibly split under a magnetic field. The magnetic behaviour of

Fig. 7-8: $15^{o}K$ axial ($\underline{H} \parallel \underline{c}$) Zeeman-infrared spectra of $CsCdCl_3$:Co(2) 5 mole % illustrating the $\gamma_4(\Gamma'_8)$ electronic line and its associated vibronic band

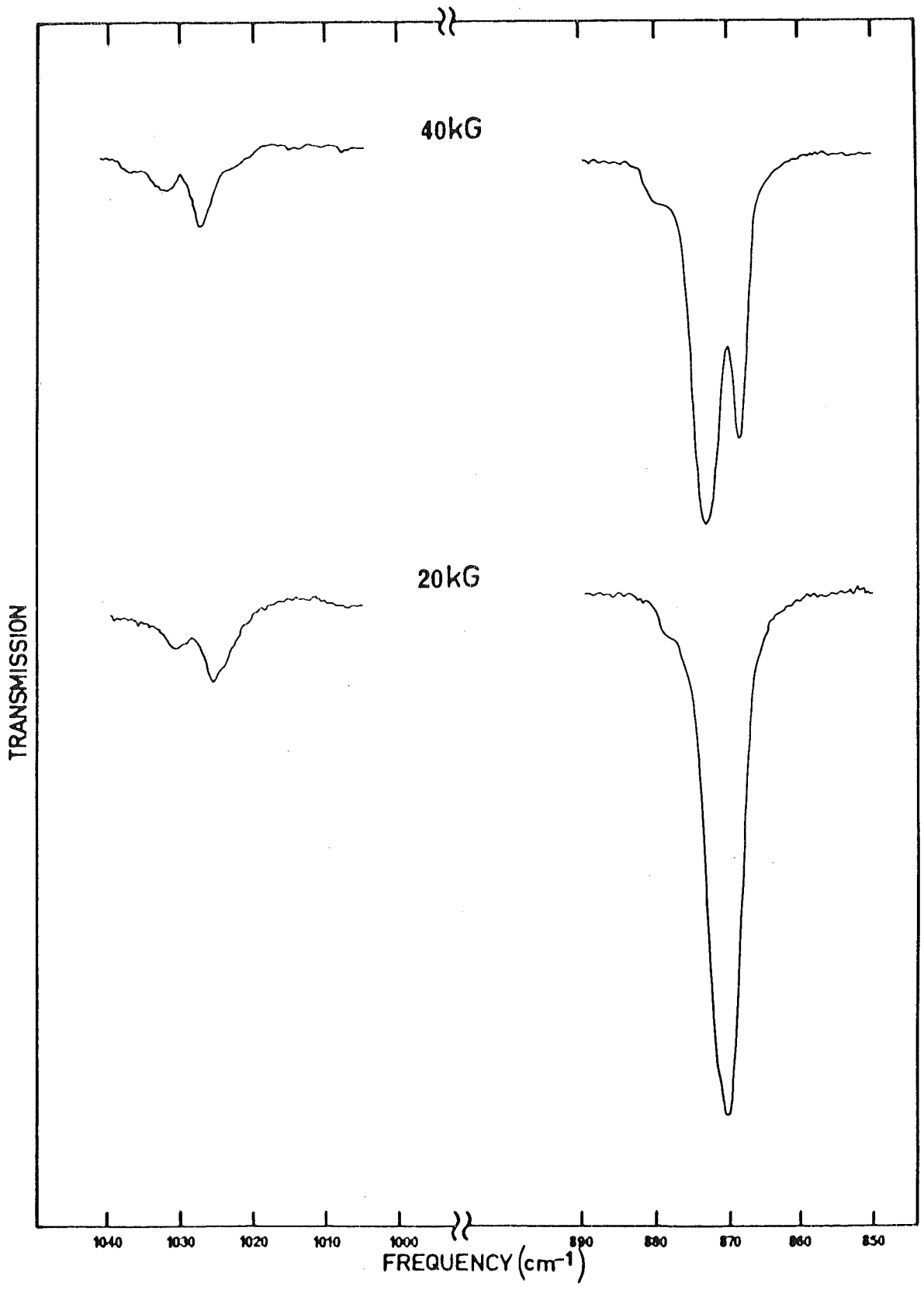

Fig. 7-9: 15^{o}K axial ($\underline{H} \parallel \underline{c}$) Zeeman-infrared spectra of $CsCdCl_3$:Co(2) 5 mole % illustrating the $\gamma_{5,6}(\Gamma'_8)$ electronic line and its associated vibronic band

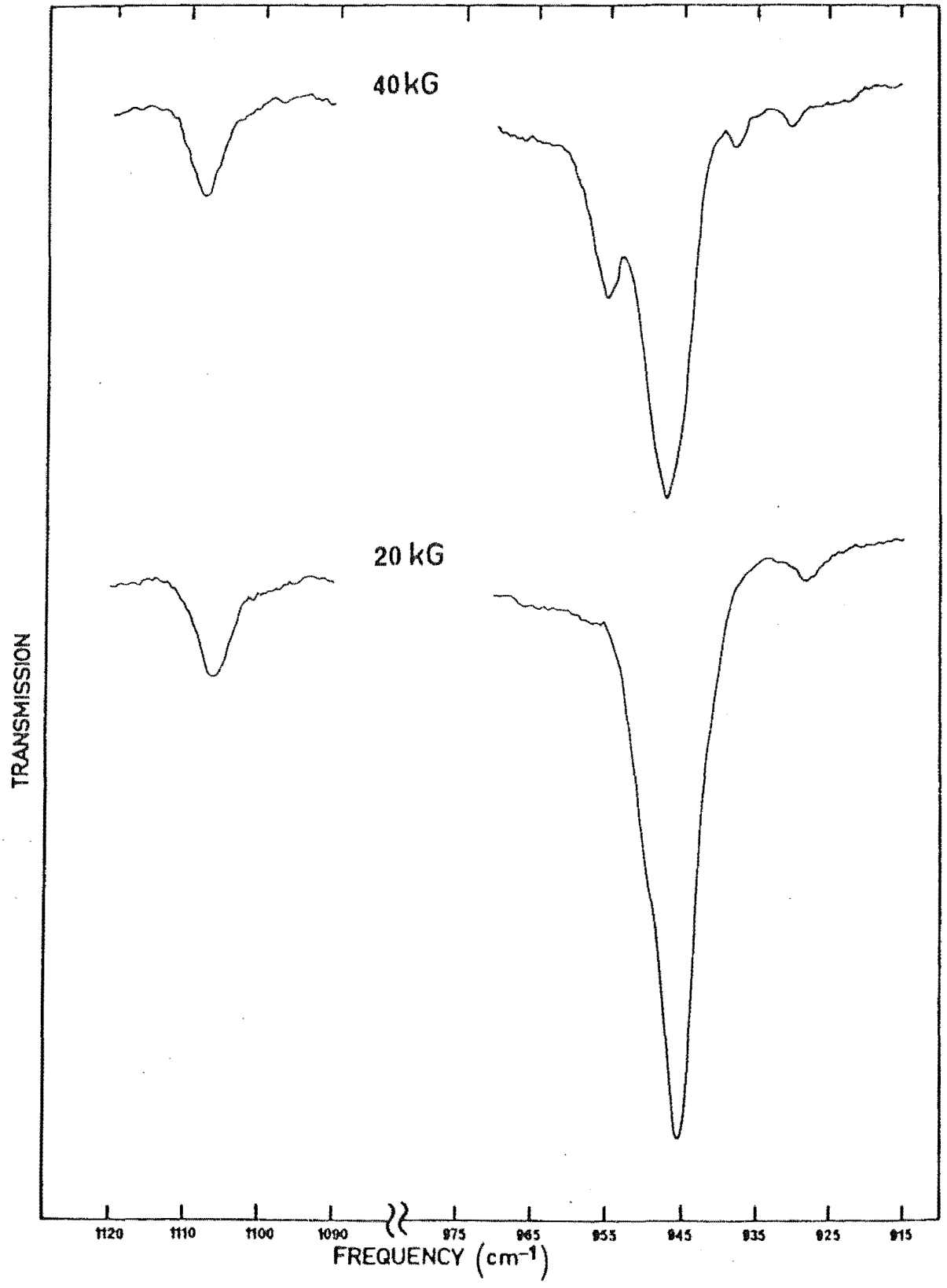

Fig. 7-10: Zeeman-infrared pattern of the $\gamma_4(\Gamma'_8)$ and $\gamma_{5,6}(\Gamma'_8)$ electronic levels of $CsCdCl_3$:Co(2) 5 mole %, and their associated vibronic bands, recorded at 15°K

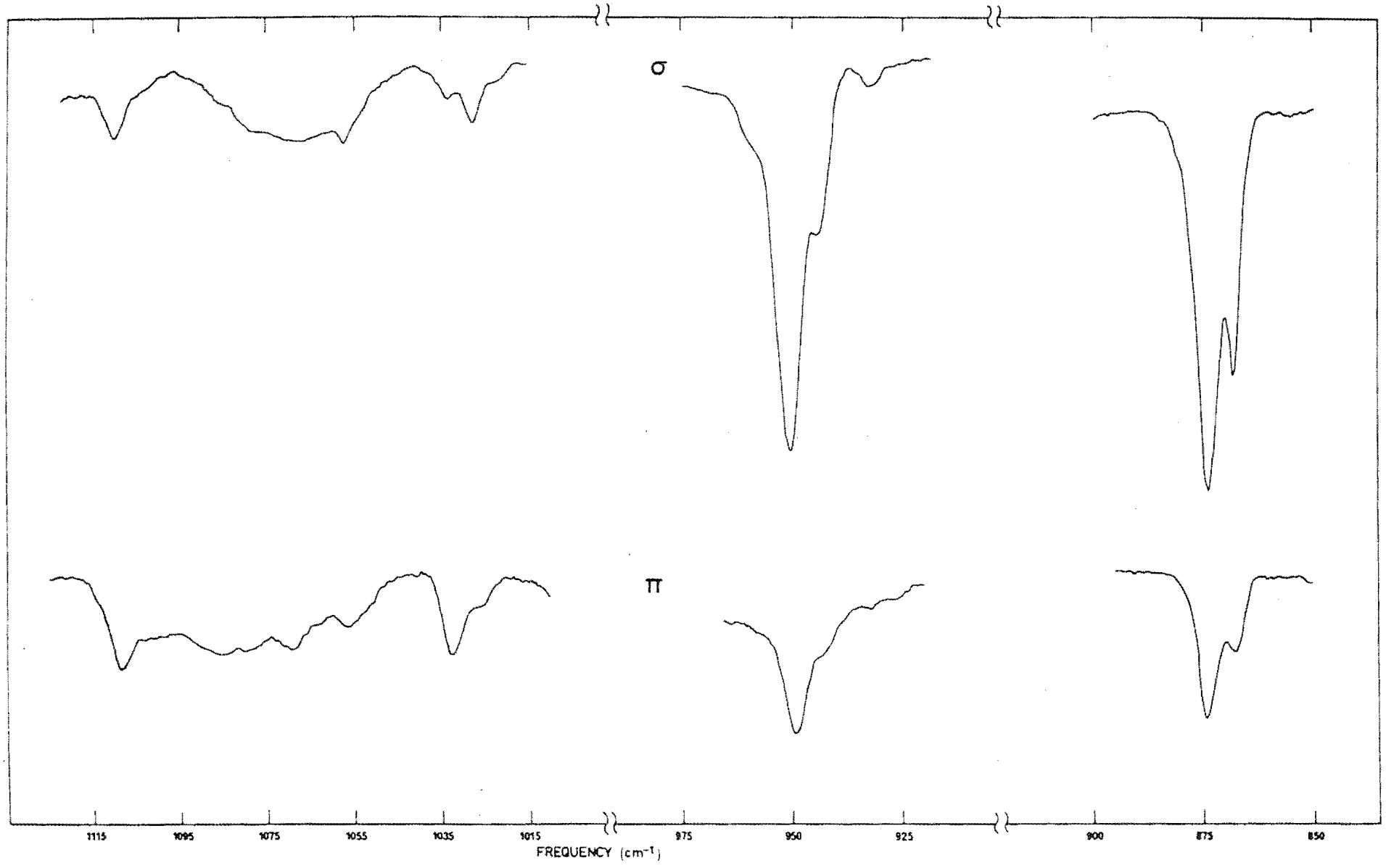

TABLE 7-3: Zeeman-infrared axial data on $CsCdCl_3$:Co 2 mole % at 15°K for (H‖c)

Frequency (cm^{-1})	Shift (cm^{-1})[a]	Width (cm^{-1})	Int.(cm^{-2})
	40 kG		
869.0±0.5	-2.2	3	0.52
873.5±0.5	2.3	4.3	1.54
880 ±1	1.7	-	-
930.0±0.7[b]	2.0	-	-
937.5±0.7	-8.6	-	-
947.2±0.5	1.1	6.3	2.33
954.7±0.5	8.6	6	0.81
1027.0±0.5[b]	2.4	-	-
1032 ±1[c]	2.0	-	-
1106.6±0.5[d]	1.1	-	-
	20 kG		
871.0±0.5	-0.2	4.3	2.85
879 ±1	0.7	-	-
928.5±0.7[b]	0.5	-	-
946.1±0.5	0.0	4.1	3.29
1025.0±0.6[b]	0.4	-	-
1030.5±0.6[c]	0.5	-	-
1105.5±0.5[d]	0.0	-	-

a: Shifts from zero-field positions.

b,c,d: Designate the vibronic lines associated with the $\Gamma_8'^{+}$ doublet of Co(2), $\gamma_4(\Gamma_8')$ and $\gamma_{5,6}(\Gamma_8')$ electronic parent levels respectively.

Each curly bracket indicates the set of split components of a zero-field line.

TABLE 7-4: Zeeman-infrared polarization data on $CsCdCl_3$:Co 5 mole % at 15°K for a 40 kG field (H⊥c)

Frequency (cm^{-1})	Shift (cm^{-1})[a]	Width (cm^{-1})	Int.(cm^{-2})
	σ spectrum		
868.6±0.5	-2.6	3	0.97
874.4±0.5	3.2	3.3	4.45
931.0±0.8[b]	3.0	-	-
943 ±1	-3.1	4	0.39
949.8±0.5	3.7	4.8	3.98
959 ±2	1.0	-	-
1027.6±0.6[b]	3.0	-	-
1033.2±0.8[c]	3.7	-	-
1057.0±0.7[b]	3.0	-	-
1070 ±3	-	-	-
1109.0±0.7[d]	3.5	-	-
	π spectrum		
868.6±0.5	-2.6	7	0.55
875.0±0.5	3.2	6.0	1.09
943 ±1	-3.1	-	-
950.0±0.5	3.9	6.0	0.97
1027 ±1[c]	-2.5	-	-
1033.0±0.6[c]	3.5	-	-
1056 ±1[d]	4.0	-	-
1070 ±1	4.0	-	-
1085 ±3	3.0	-	-
1109.0±0.7[d]	3.5	-	-

The footnote of Table 7-3 applies.

the two electronic $\gamma_4(\Gamma'_8)$ and $\gamma_{5,6}(\Gamma'_8)$ lines proved to be more interesting as their profiles were significantly altered by the field.

Axial ($\underline{H}\|\underline{c}$) Spectra

When the crystals were subjected to a 40 kG field, the following changes to the features of the zero-field axial spectra were noted. The $\gamma_4(\Gamma'_8)$ electronic line resolved into two components 4.5 cm^{-1} apart, with the higher energy component being three times as intense as the other (Fig. 7-8). The 878.3 cm^{-1} satellite line, which is distinct and sharp in the absence of a field, now appeared as a weak, broad side band. Three components constitute the 40 kG trace of the split $\gamma_{5,6}(\Gamma'_8)$ electronic level shown in Fig. 7-9, the weakest of which is the 937.5 cm^{-1} line. The central line at 947.7 cm^{-1} is three times stronger than the remaining component at 954.7 cm^{-1}. This is contrary to the usual structure of split electronic lines which have the weaker components on the lower energy side. Both the electronic lines remained unresolved and unshifted at 20 kG. However they each assumed an asymmetric line shape.

Polarized ($\underline{H}\perp\underline{c}$) Spectra

These spectra described below were recorded with the crystals exposed to the maximum field of 40 kG. They are depicted in Fig. 7-10.

σ-polarized Spectrum

Under this field, the $\gamma_4(\Gamma'_8)$ electronic line was transformed into two components at 868.6 and 874.4 cm^{-1}, with the former being the weaker. The 878.3 cm^{-1} zero-field satellite line is no longer apparent having being masked by the strong 874.4 cm^{-1} line. The $\gamma_{5,6}(\Gamma'_8)$ electronic line partially split into two components at 943.5 and 949.8 cm^{-1}, with the lower energy component being the weaker. A side band at around 959 cm^{-1} appeared on the 949.8 cm^{-1} line.

A comparison of Fig. 7-10 with Fig. 6-5 shows that the fine structure, appearing on the broad band centred at 1070 cm^{-1} of the latter figure, has been smeared out by the field. A line at 1057 cm^{-1} is the only remaining structure. All the vibronic bands examined shifted to higher frequencies.

π-polarized Spectrum

The Zeeman effects on the two electronic $\gamma_4(\Gamma'_8)$ and $\gamma_{5,6}(\Gamma'_8)$ lines in the π spectrum were identical to that of the σ spectrum. Under the influence of the field the vibronic bands became broader, which resulted in the weaker ones being less pronounced. Only the sharp intense 1029.5 cm^{-1} vibronic line, associated with the $\gamma_4(\Gamma'_8)$ electronic state, was seen to split into two components. The other vibronic bands examined followed the general trend of being shifted to higher frequencies.

7.4 ANALYSIS OF ZEEMAN-INFRARED SPECTRA

The Kramer's degenerate levels of the cobaltous ions are each split by a magnetic field into two components. The frequencies of the electronic Zeeman transitions, between the split components of the ground state and those of the excited states of these ions in $CsMgCl_3$ and $CsCdCl_3$ in a 40 kG field were computed using the Oscstrengths/H3942 and Oscstrengths/H120 programs listed in the appendix. The computed frequencies are listed in Tables 7-5 and 7-6 for $CsMgCl_3$:Co and Table 7-7 for $CsCdCl_3$:Co(2).

The experimental electronic Zeeman-infrared transition frequencies could be matched to the computed transition frequencies to within 2 cm^{-1} shown in the above tables. However Table 5-2 reveals that the g values for the $\gamma_4^+(\Gamma_6^+)$ ground state computed from the crystal field model differ by as much as 0.4 from the EPR values. A better agreement between the experimental and computed transition frequencies can be

TABLE 7-5: Computed and experimental frequencies and oscillator strengths for assigned electronic transitions in $CsMgCl_3$:Co 2.0 wt. % at 15°K for 40 kG ($H \| c$)

Electronic-Zeeman transition	Frequency (cm^{-1})		Osc. Strength (10^{-10})	
	Expt.	Compt.	Expt.	Compt.
$\gamma_4^+(\Gamma_6^+) \rightarrow \gamma_5^+(\Gamma_7^+)$	1387.5	1387.28	9.6	24.4
$\gamma_5^+(\Gamma_6^+) \rightarrow \gamma_4^+(\Gamma_7^+)$	1371	1368.93	5.0	9.5
$\gamma_4^+(\Gamma_6^+) \rightarrow \gamma_6^+(+)(\Gamma_8'^+)$	1263	1265.33	554	2330
$\gamma_5^+(\Gamma_6^+) \rightarrow \gamma_6^+(-)(\Gamma_8'^+)$		1262.07		604
$\gamma_4^+(\Gamma_6^+) \rightarrow \gamma_6^+(-)(\Gamma_8'^+)$	-	1276.65	-	0.12
$\gamma_5^+(\Gamma_6^+) \rightarrow \gamma_6^+(+)(\Gamma_8'^+)$	-	1250.75	-	0.03
$\gamma_4^+(\Gamma_6^+) \rightarrow \gamma_5^+(\Gamma_8'^+)$	826	827.55	2.3	1.4
$\gamma_5^+(\Gamma_6^+) \rightarrow \gamma_4^+(\Gamma_8'^+)$	-	818.83	-	0.5

obtained by using the EPR g values for the ground states, together with the computed g values for the excited states. The splittings evaluated using these g values were added or subtracted, as appropriate, from the zero-field transition frequencies to yield the energy level schemes of Figs. 7-11 and 7-12. Agreement between the transition frequencies thus calculated and the observed frequencies is now within 0.5 cm^{-1}.

Fig. 2-3 displays the Zeeman levels of the cobalt ion labelled by the irreps of the various symmetry groups appropriate for the cobalt ion site in a magnetic field. Selection rules governing the electronic Zeeman-infrared transitions can be derived from the direct products of these irreps with the irreps of the appropriate transition operators (Sec.2.2).

For $CsMgCl_3$:Co the transition operator is magnetic dipole while for $CsCdCl_3$:Co(2) it is electric dipole in character. The magnetic dipole and electric dipole transition operators transform similarly except that,

Table 7-6: Computed and experimental Zeeman frequencies and oscillator strengths for assigned electronic transitions in $CsMgCl_3$:Co 1.5 wt. % at 15°K for 40 kG ($\underline{H} \perp \underline{c}$).

Electronic transition	Computed Freq. (cm^{-1})	σ Experimental Freq. (cm^{-1})	σ Osc.Strength (10^{-10}) Expt.	σ Osc.Strength (10^{-10}) Compt.	π($\underline{k} \parallel \underline{H}$) Experimental Freq. ($cm^{-1}$)	π($\underline{k} \parallel \underline{H}$) Osc.Strengths ($10^{-10}$) Expt.	π($\underline{k} \parallel \underline{H}$) Osc.Strengths ($10^{-10}$) Compt.	π($\underline{k} \perp \underline{H}$)* Osc.Strengths ($10^{-10}$) Compt.
a → b	1383.12	1384.2±0.5	63.8	254.6	1384 ±1	7.1	18.2	-
b → a	1373.25	1374.4±0.5	43.7	185.3	1374 ±1	5.5	18.1	-
a → a	1377.30	-	-	-	-	-	-	19.3
b → b	1379.08	-	-	-	-	-	-	16.8
a → a,b	1265.69	1263 ±2	36	0.1	1264.6±0.5	790	1761	1761
b → a,b	1261.65			0.1	1261 ±1		1149	1149
a → b	825.37	824.5±0.5	10.7	8.6	824 ±1	-	1.1	-
b → a	821.13	819.5±0.5	6.0	6.5	819 +1	-	0.8	-
a → a	825.18	-	-	-	-	-	-	1.2
b → b	821.32	-	-	-	-	-	-	0.7

a = $\gamma_3^+(C_{2h})$ or $\gamma_2^+(+)(C_i)$ b = $\gamma_4^+(C_{2h})$ or $\gamma_2^+(-)(C_i)$

* Not observed experimentally.

TABLE 7-7: Computed and experimental Zeeman frequencies for assigned electronic transitions in $CsCdCl_3$:Co(2) 5 mole % at 15°K for 40 kG ($\underline{H} \| \underline{c}$)

Electronic-Zeeman transition	Frequency (cm^{-1})	
	Expt.	Compt.
$\gamma_4(\Gamma_6) \rightarrow \gamma_6(-)(\Gamma'_8)$	954.7	954.80
$\gamma_4(\Gamma_6) \rightarrow \gamma_6(+)(\Gamma'_8)$	947.2	947.54
$\gamma_5(\Gamma_6) \rightarrow \gamma_6(+)(\Gamma'_8)$	937.5	937.53
$\gamma_4(\Gamma_6) \rightarrow \gamma_5(\Gamma'_8)$	873.5	873.51
$\gamma_5(\Gamma_6) \rightarrow \gamma_4(\Gamma'_8)$	869.0	868.96

for groups having inversion symmetry, the former has even parity while the latter odd parity. The irreps of the x,y and z components of these two transition operators are given below for the different reduced symmetries.

Operator		$C_{3i}(C_3)$	$C_{2h}(C_2)$	$C_i(C_1)$
Magnetic dipole	z component	γ_1^+	γ_2^+	γ_1^+
	x,y component	$\gamma_2^+ + \gamma_3^+$	$\gamma_1^+ + \gamma_2^+$	γ_1^+
Electric dipole	z component	γ_1^-	γ_2^-	γ_1^-
	x,y component	$\gamma_2^- + \gamma_3^-$	$\gamma_1^- + \gamma_2^-$	γ_1^-

Here C_{3i}, C_{2h} and C_i are the effective site symmetries of the D_{3d} cobalt ion in $CsMgCl_3$. For the C_3, C_2 and C_1 symmetries, appropriate to the C_{3v} cobalt ion in $CsCdCl_3$, the same irreps occur but with no parity

labels. The electronic Zeeman states of the cobalt ions in both systems are also characterized by the same group irreps, except that those of $CsMgCl_3$:Co have even parity while those of $CsCdCl_3$:Co(2) have no parity labels (Sec. 2.2). Hence the following direct product representations, although written specifically for $CsMgCl_3$:Co, are also applicable for the case of $CsCdCl_3$:Co(2).

Transitions due to a given component of the electric dipole transition operator occur in opposite polarization to the same component of the magnetic dipole transition operator because of the orthogonality of the $\underline{E}$ and $\underline{B}$ vectors of the infrared radiation. Thus in the σ spectrum, where the $\underline{E}$ vector is perpendicular to the crystal $\underline{c}$ axis, infrared absorption occurs through the x,y components of the electric dipole transition operator or the z component of the magnetic dipole transition operator. On the other hand in the π spectrum, where the $\underline{E}$ vector is parallel to the crystal $\underline{c}$ axis, the infrared absorption is caused by the z component of the electric dipole transition operator or the x,y component of the magnetic dipole transition operator.

The selection rules for the electronic Zeeman transitions of the cobalt ions in the two double chlorides are derived as follows.

For $\underline{H} \| \underline{c}$, the appropriate symmetry is $C_{3i}(C_3)$ and the zero-field $\gamma_4^+(\Gamma_6^+)$ ground state is split into the γ_4^+ and γ_5^+ states, while the upper Zeeman states are labelled by the γ_4^+,γ_5^+ and γ_6^+ irreps as shown in Fig. 2-3. From the product representations

$$\begin{aligned} \gamma_4^+ \times (\gamma_2^+ + \gamma_3^+) &= \gamma_5^+ + \gamma_6^+ \\ \gamma_5^+ \times (\gamma_2^+ + \gamma_3^+) &= \gamma_4^+ + \gamma_6^+ \end{aligned} \qquad (7.1)$$

it follows that the $\gamma_4^+ \rightarrow \gamma_4^+$ and $\gamma_5^+ \rightarrow \gamma_5^+$ electronic transitions are both magnetic- and electric-dipole forbidden in the axial ($\underline{H} \| \underline{c}$) spectra of $CsMgCl_3$:Co and $CsCdCl_3$:Co(2).

For $\underline{H} \perp \underline{c}$, the $D_{3d}(C_{3v})$ site symmetry of the cobalt ion is lowered to either $C_{2h}(C_2)$ if the magnetic field is directed along a twofold crystal axis or $C_i(C_1)$ otherwise. Even for a 40 kG field, the Zeeman interaction is small compared with the trigonal crystal field experienced by the cobalt ions. Hence the cobalt ion site symmetry is very nearly $D_{3d}(C_{3v})$, and the electronic lines still largely retain their zero-field polarizations in the polarized ($\underline{H} \perp \underline{c}$) Zeeman-infrared spectra. For this reason the Zeeman ($\underline{H} \perp \underline{c}$) spectra are labelled as either the $\sigma(\underline{H} \perp \underline{c})$ or $\pi(\underline{H} \perp \underline{c})$ spectra. In the former, the $\underline{B}$ vector of the infrared radiation is parallel to the crystal's threefold axis while in the latter the $\underline{B}$ vector is perpendicular to the crystal's threefold axis.

In the $C_{2h}(C_2)$ symmetry, the split components of both the electronic ground- and excited-states transform as either the γ_3^+ and γ_4^+ irreps. The z component of the magnetic dipole transition operator transforms as the γ_2^+ irrep of $D_{3d}(C_{3v})$ which becomes the γ_2^+ irrep of $C_{2h}(C_2)$. The x,y component of this transition operator transforms as the γ_3^+ irrep of D_{3d} which decomposes to $\gamma_1^+ + \gamma_2^+$ in C_{2h}. The C_{2h} group has its z axis along the magnetic field direction and the γ_1^+ component of the x,y component of the magnetic dipole transition operator is along this z axis. Since the infrared radiation is also directed along this z axis, this γ_1^+ component is not operative. Hence for the $\pi(\underline{H} \perp \underline{c})$ spectra recorded, only the γ_2^+ component of the magnetic dipole transition operator need be considered. From the product representations

$$\begin{aligned} \gamma_3^+ \times \gamma_2^+ &= \gamma_4^+ \\ \gamma_4^+ \times \gamma_2^+ &= \gamma_3^+ \end{aligned} \qquad (7.2)$$

it follows that, for $CsMgCl_3$:Co, the $\gamma_3^+ \rightarrow \gamma_3^+$ and $\gamma_4^+ \rightarrow \gamma_4^+$ magnetic dipole electronic transitions are absent in both the $\sigma(\underline{H} \perp \underline{c})$ and $\pi(\underline{H} \perp \underline{c})$ spectra. These results also apply for the electric dipole electronic transitions of $CsCdCl_3$:Co(2).

In the $C_i(C_1)$ symmetry, all the six lowest Kramer's doublets are split into levels labelled by the γ_2^+ irreps, while the x,y and z components of the electric- and magnetic-dipole transition operators transform as the γ_1^+ irrep. Hence all the electronic transitions are allowed in both polarizations for the two systems examined.

Polarized Zeeman-infrared spectra were recorded with the magnetic field applied in an arbitrary direction in a plane normal to the crystal $\underline{c}$ axis, and the effective cobalt ion site symmetry is $C_i(C_1)$. However not all the electronic transitions were observed, indicating the operation of selection rules appropriate for a symmetry higher than $C_i(C_1)$. Such a symmetry can, in $CsMgCl_3$:Co, occur for the case of the magnetic field directed along a twofold crystal axis and this would be the approximate symmetry if the field is not too far removed from this axis. For the C_{2h} symmetry, only two electronic transitions are expected for each polarization in qualitative agreement with observation. In the case of $CsCdCl_3$:Co(2) there is no twofold crystal axis. However, as mentioned in Sec. 2.2, an approximate C_2 symmetry exists for the magnetic field applied along a pseudo twofold crystal axis and this symmetry gives results similar to that of the C_{2h} symmetry of $CsMgCl_3$:Co.

By utilizing the selection rules derived above for the $C_{3i}(C_3)$ and $C_{2h}(C_2)$ groups, the observed electronic Zeeman-infrared transitions can be assigned as is shown in Figs. 7-11 and 7-12. For the $\underline{H} \parallel \underline{c}$ case the zero-field electronic ground state components are labelled by the γ_4^+ and γ_5^+ irreps of the $C_{3i}(C_3)$ group, and for $\underline{H} \perp \underline{c}$ by either the γ_3^+ and γ_4^+ irreps of the $C_{2h}(C_2)$ group or the γ_2^+ irrep of the $C_i(C_1)$ group. They may alternatively be characterized by effective spin values of $+\frac{1}{2}$ and $-\frac{1}{2}$, with the $+\frac{1}{2}$ irrep having the lower energy. The lowest Zeeman levels are therefore assigned as the $+\frac{1}{2}$ irrep namely γ_4^+, γ_3^+ and $\gamma_2^+(+\frac{1}{2})$ for the respective $C_{3i}(C_3)$, $C_{2h}(C_2)$ and $C_i(C_1)$ symmetries.

Fig. 7-11: Zeeman energy-level diagram illustrating IR transition observed for $CsMgCl_3$:Co 1.0 to 2.0 wt. % at 15°K. Figures in parentheses denote experimental frequencies (cm^{-1}).

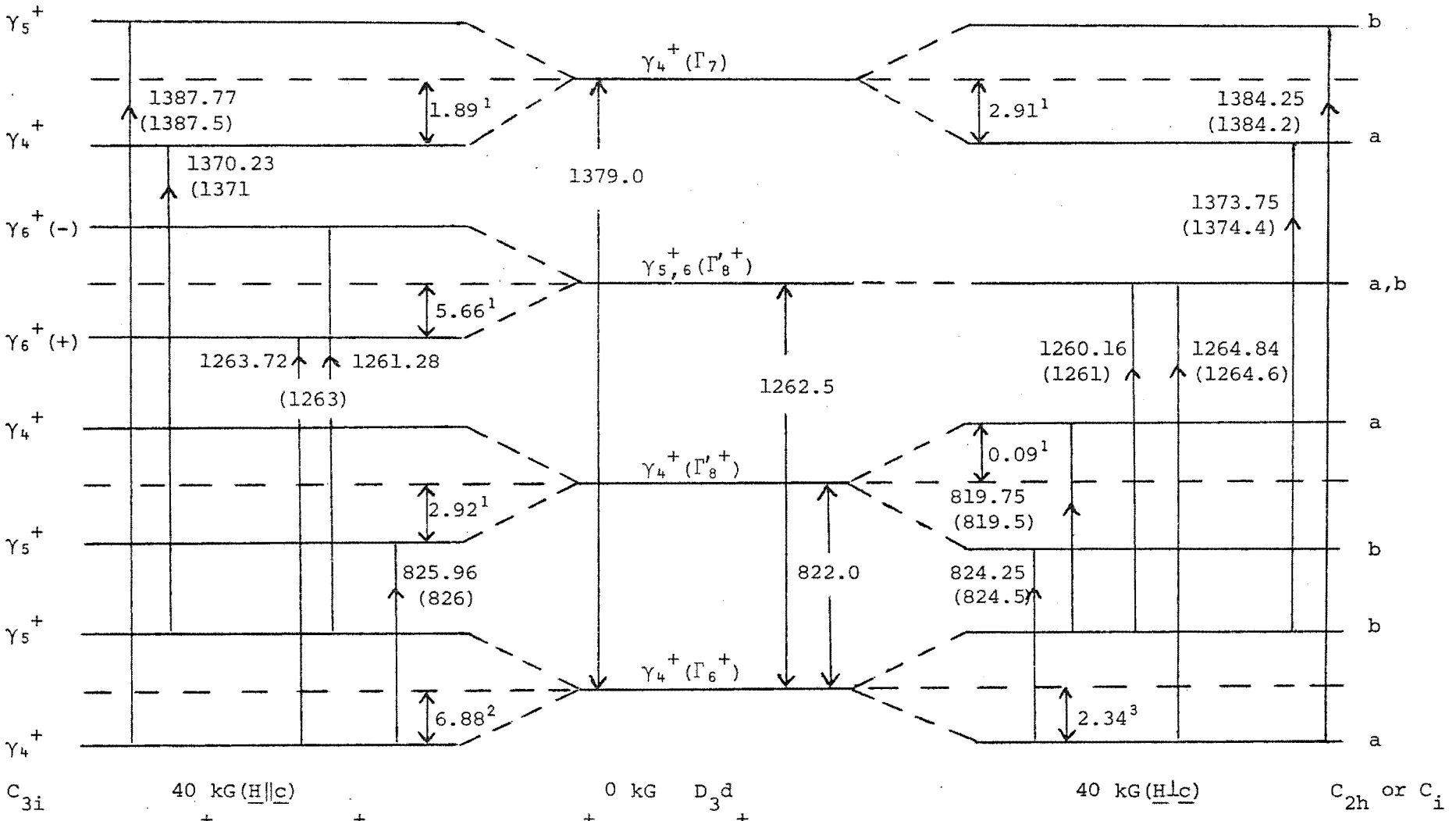

a = $\gamma_3^+(C_{2h})$ or $\gamma_2^+(+)(C_i)$ b = $\gamma_4^+(C_{2h})$ or $\gamma_2^+(-)(C_i)$

1 : Shifts calculated from computed g values of Table 4.3.

2,3 : Shifts calculated from EPR g values of 7.37 and 2.51 respectively.

Fig. 7-12: Zeeman energy-level diagram illustrating IR transitions observed for $CsCdCl_3$:Co(2) 1,2 and 5 mole % at 15°K. Figures in parentheses denote experimental frequencies in cm^{-1}.

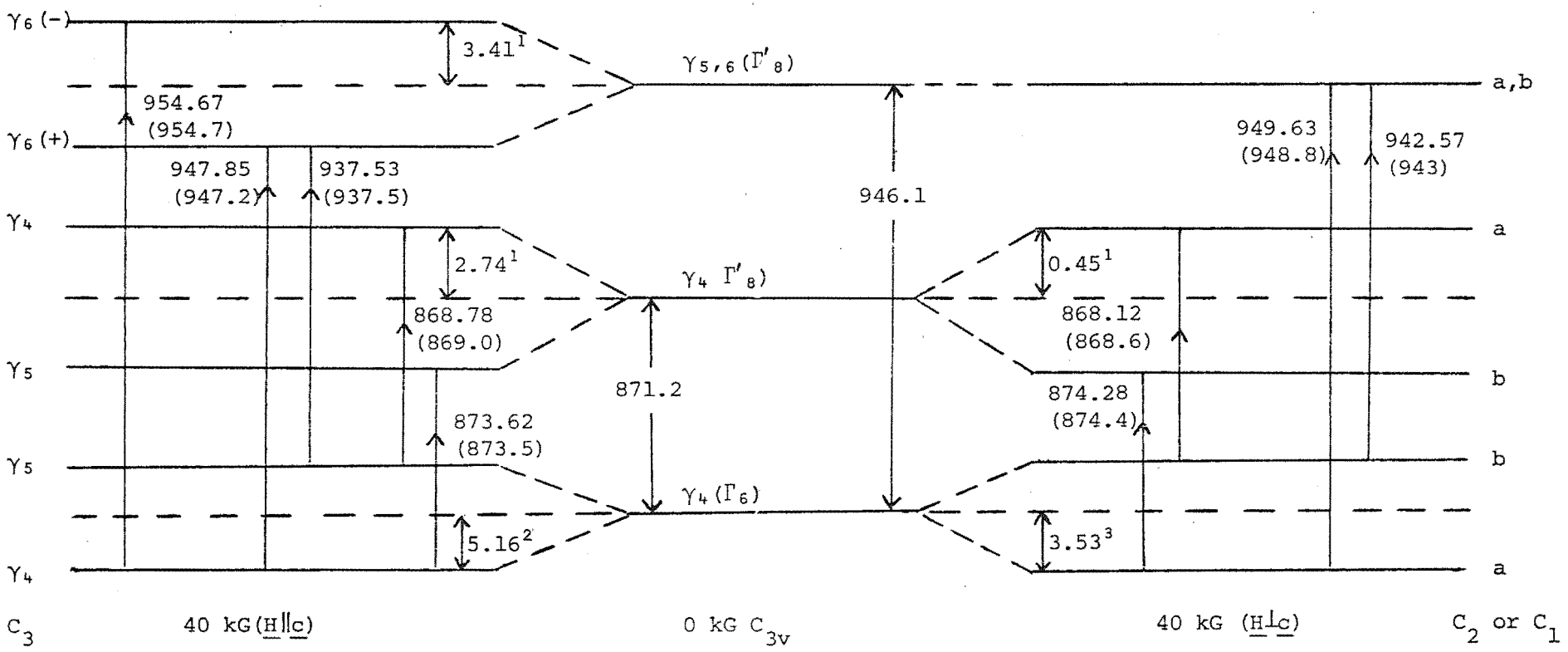

a = $\gamma_3(C_2)$ or $\gamma_2(+)(C_1)$ b = $\gamma_4(C_2)$ or $\gamma_2(-)(C_1)$

1 : Shifts calculated from computed g values of Table 4-3.

2,3 : Shifts calculated from EPR g values of 5.53 and 3.78 respectively.

TABLE 7-8: Comparison of infrared experimental and computed g values of Co^{2+}.

Electronic State	$g_{\parallel}$ Expt.	$g_{\parallel}$ Compt.	$g_{\perp}$ Expt.	$g_{\perp}$ Compt.
$CsMgCl_3$:Co				
$\gamma_4^+(\Gamma_7^+)$	1.74±0.21	2.02	3.06±0.21	3.12
$\gamma_{5,6}^+(\Gamma_8'^+)$	6.84±0.21	6.06	0.26±0.10	0.00
$\gamma_4^+(\Gamma_8'^+)$	3.09±0.32	3.13	0.17±0.21	0.10
$CsCdCl_3$:Co(2)				
$\gamma_{5,6}(\Gamma_8')$	4.02±0.11[a]	3.89	0.46±0.21	0.00
$\gamma_4(\Gamma_8')$	3.07±0.21	2.93	0.35±0.21	0.48

a: Only this experimental g value was not evaluated using equation (5.3).

The observed Zeeman-infrared transitions, for each of the zero-field electronic state, originated from either the upper or lower component of the zero-field electronic ground state. Hence their magnetic splitting factors were evaluated using equation (5.3) which incorporates the EPR ground state g values. In the case of the electronic $\gamma_{5,6}(\Gamma_8')$ state of $CsCdCl_3$:Co(2), its $g_{\parallel}$ value was evaluated from the difference of the frequencies of the observed transitions that originated from the lower component of the zero-field $\gamma_4(\Gamma_6)$ ground state. The excited state predicted g values were computed from the crystal field model as discussed in Sec. 4.5. They are in good agreement with those obtained from the Zeeman-infrared experiments. Table 7-8 lists these two sets of g values.

The predicted oscillator strengths for the magnetic dipole electronic

transitions of $CsMgCl_3$:Co at 40 kG were calculated using equation (6.2). The matrix elements of the components of the magnetic dipole transition operator $(L_z + 2S_z)$ and $(L_x + 2S_x)$, which appear in the equation, were evaluated between the lowest twelve electronic Zeeman states for both $\underline{H} \parallel \underline{c}$ and $\underline{H} \perp \underline{c}$ using the computer programs Oscstrengths/H3942 and Oscstrengths/H120 respectively (Appendix). The predicted oscillator strengths were multiplied by the appropriate Boltzmann factors $[1 + \exp(-\frac{E}{kT})]^{-1}$ and $\exp(-\frac{E}{kT})[1 + \exp(-\frac{E}{kT})]^{-1}$ for the lower and upper components of the zero-field ground state E cm^{-1} apart. Here k is the Boltzmann constant and the crystal temperature T was assumed to be $15^{\circ}K$. The experimental oscillator strengths of the observed electronic Zeeman-infrared transitions for $CsMgCl_3$:Co were also calculated using the procedure outlined in Sec. 6.4. Tables 7-5 and 7-6 list the experimental and predicted oscillator strengths and show reasonable agreement between these two sets of values. The notations $\pi(\underline{k} \parallel \underline{H})$ and $\pi(\underline{k} \perp \underline{H})$, that appear in Table 7-6, designate the two different π spectra. In the former the direction $\underline{k}$ of the infrared radiation is parallel to the magnetic field, while in the latter it is normal to the magnetic field. Of these two spectra, only the $\pi(\underline{k} \parallel \underline{H})$ spectrum can be measured with the existing Zeeman-infrared arrangement in which the direction of the radiation is restricted along the solenoidal magnet's axis. The oscillator strengths of the $\gamma_3^+ \rightarrow \gamma_3^+$ and $\gamma_4^+ \rightarrow \gamma_4^+$ electronic transitions which are only permitted in the $\pi(\underline{k} \perp \underline{H})$ spectrum, and are therefore not observed with the optical arrangement employed, are listed for completeness.

The behaviour of the vibronic bands under a magnetic field was found to parallel that of their electronic parent states. The only exception was found for the case of the 1591.0 cm^{-1} vibronic line in the polarized Zeeman spectra of $CsMgCl_3$:Co shown in Fig. 7-7. While a splitting of 10 cm^{-1} was recorded at 40 kG for its $\gamma_4^+(\Gamma_7^+)$ electronic parent state, the 1591.0 cm^{-1} vibronic line did not even shift under the same field.

Such a difference in behaviour is not easily explained. For the case of large electron-phonon interaction vibronic splittings, Satten et.al.[39] have shown that vibronic levels can have g values which are smaller than those of their electronic parent levels. However it is not evident that the $CsMgCl_3$:Co system satisfies the criterion of large electron-phonon interaction splittings, compared to the Zeeman splittings, for such effects to occur. Water absorption lines occur in the region of the 1591 cm^{-1} vibronic line and could complicate the Zeeman spectra sufficiently, resulting in an appreciable anomalous effect.

CHAPTER VIII

THE RAMAN AND INFRARED SPECTRA OF $CsCoCl_3$ AND $KCdCl_3$:Co AND THE OPTICAL SPECTRA OF $CsCdCl_3$:Co.

8.1 $KCdCl_3$:Co AND $CsCoCl_3$

8.1.1 Introduction

The electronic transitions of Co^{2+} ions in $KCdCl_3$:Co and $CsCoCl_3$ crystals were investigated using Raman and infrared spectroscopy. On substituting for the Cd^{2+} ions in $KCdCl_3$, the Co^{2+} ions are located in sites of C_s ($=C_{1h}$) symmetry. Owing to the difficulty in locating the crystal axis, no polarization studies of $KCdCl_3$:Co were attempted. The Co^{2+} ions in $CsCoCl_3$ are in sites of D_{3d} symmetry. Polarized infrared spectra of $CsCoCl_3$ have been measured. Melamud et. al.[40] have found that $CsCoCl_3$ undergoes a transition to antiferromagnetism at $21.5^{o}K$.

An account of the spectra obtained is given below.

8.1.2 $KCdCl_3$:Co

The Raman experiments were performed at liquid nitrogen temperatures and the infrared experiments at both liquid-nitrogen and -helium temperatures. Table 8-1 summarizes the numerical results. All crystals examined contained a nominal doping of 2 mole % of $KCoCl_3$.

In the low-energy portion of the randomly polarized Raman spectrum of Fig. 8-1, lie 12 lines of varying intensities with frequencies ranging from 35-265 cm^{-1}. Barr and Goldstein[41] have reported the vibrational Raman spectrum of pure $KCdCl_3$ and, except for two lines at 70 and 124 cm^{-1}, their results are in agreement with those found in this work. Lines shifted by 465, 542, 913, 1103 and 1188 cm^{-1} also appear in the spectrum.

Fig. 8-1: 80°K Raman spectrum of a randomly orientated $KCdCl_3$ crystal containing 2 mole % of $KCoCl_3$

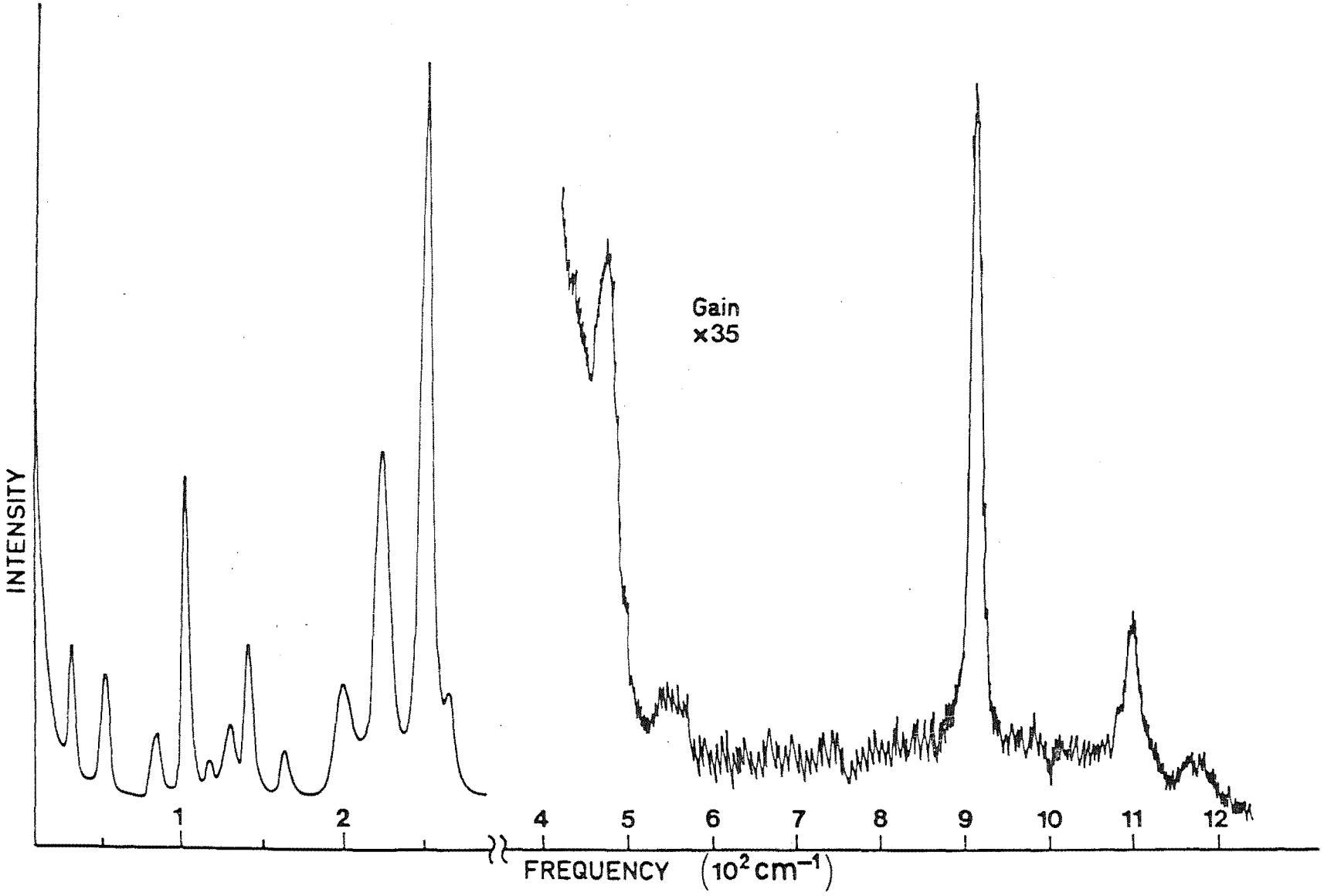

Fig. 8-2: Infrared spectra of a randomly orientated $KCdCl_3$ crystal containing 2 mole % of $KCoCl_3$

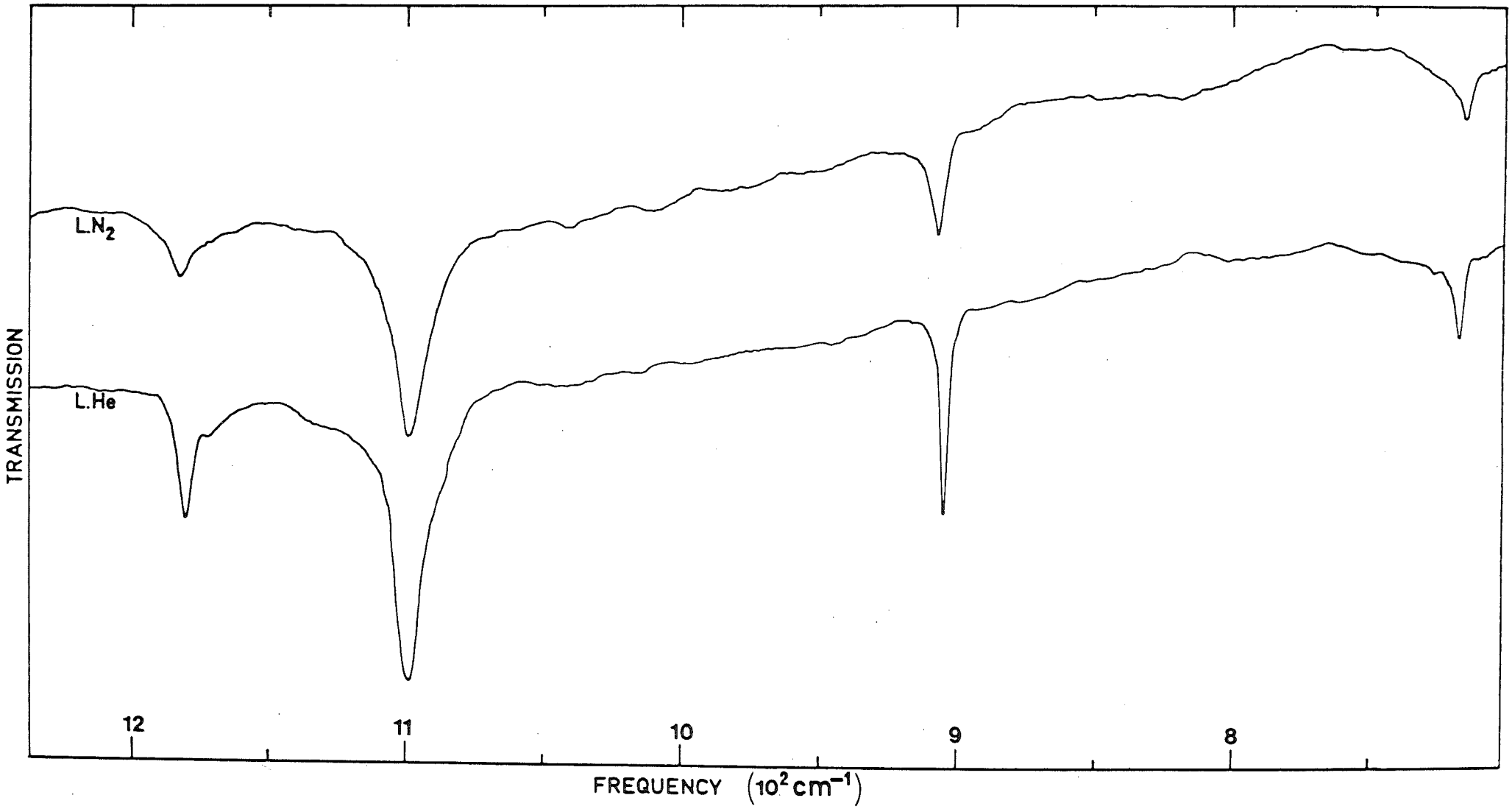

TABLE 8-1: Spectral data on randomly orientated crystals of $KCdCl_3$:Co 2 mole %. All measurements are in cm^{-1}.

Raman 80°K			
Frequency	Width	Frequency	Width
35±2	-		
55±2	-	465±4	15
86±2	-	542±4	20
105±1	5	913±2	13
119±3	-	1103±3	15
132±3	-	1188±5	20
143±2	-		
165±3	-		
200±2	-		
225±1	10		
252±1	8		
265±3	-		

Infrared			
80°K		15°K	
Frequency	Width	Frequency	Width
717.0±0.8	7	717.0±0.8	5
910.0±0.8	6	906.0±0.5	3
1101.5±0.8	13	1099.5±0.5	11
1186.0±0.8	10	1181.5±0.5	7

As seen in Fig. 8-2, the 80°K infrared spectrum of a randomly orientated $KCdCl_3$:Co crystal exhibits four sharp lines only. Unlike the other spectra of $CsCdCl_3$:Co and $CsMgCl_3$:Co, it is devoid of any broad bands. Of these four lines, only the one at 717 cm^{-1} does not appear in the Raman spectra. The remaining three lines are attributed to electronic transitions of the Co^{2+} ion. On cooling to liquid helium temperatures, only the 717 cm^{-1} line remained unshifted while a weak band appeared at 1173 cm^{-1}. The 717 cm^{-1} line is assigned as an oxygen-induced absorption, analogous to the 700 cm^{-1} line observed in the infrared spectra of oxygen-ion doped $CdCl_2$ by Johnstone[9].

8.1.3 $CsCoCl_3$

The Raman and infrared spectral data on $CsCoCl_3$ obtained at liquid-nitrogen and -helium temperatures are presented in Table 8-2.

The randomly polarized Raman spectrum (Fig. 8-3), recorded at liquid helium temperatures, shows four lines shifted by 137, 188, 266 and 296 cm^{-1} in its low-energy region. The first three lines match three of the Raman lines reported by Chadwick et.al.[24] at 133, 183, and 264 cm^{-1}. In the higher-energy region of the spectrum are a sharp line at 851 cm^{-1} and two weak broad bands at 990 and 1084 cm^{-1}.

Infrared polarization studies were done using cleaved samples with faces containing the crystal c axis. Representative spectra measured at liquid-nitrogen and -helium temperatures are shown in Fig. 8-4, while the spectral data are summarized in Table 8-2. As the 1085 cm^{-1} band was very sensitive to polarization, its variation in intensity was used as a guide to set the orientation of the polarizer. The spectrum in which this band appears most intense is designated 'polarizer 90°', while that in which it is least intense, 'polarizer 0°'. It is not possible to determine which of these spectra is σ and which is π because

Fig. 8-3: Randomly polarized Raman spectrum of $CsCoCl_3$ recorded at liquid helium temperatures.

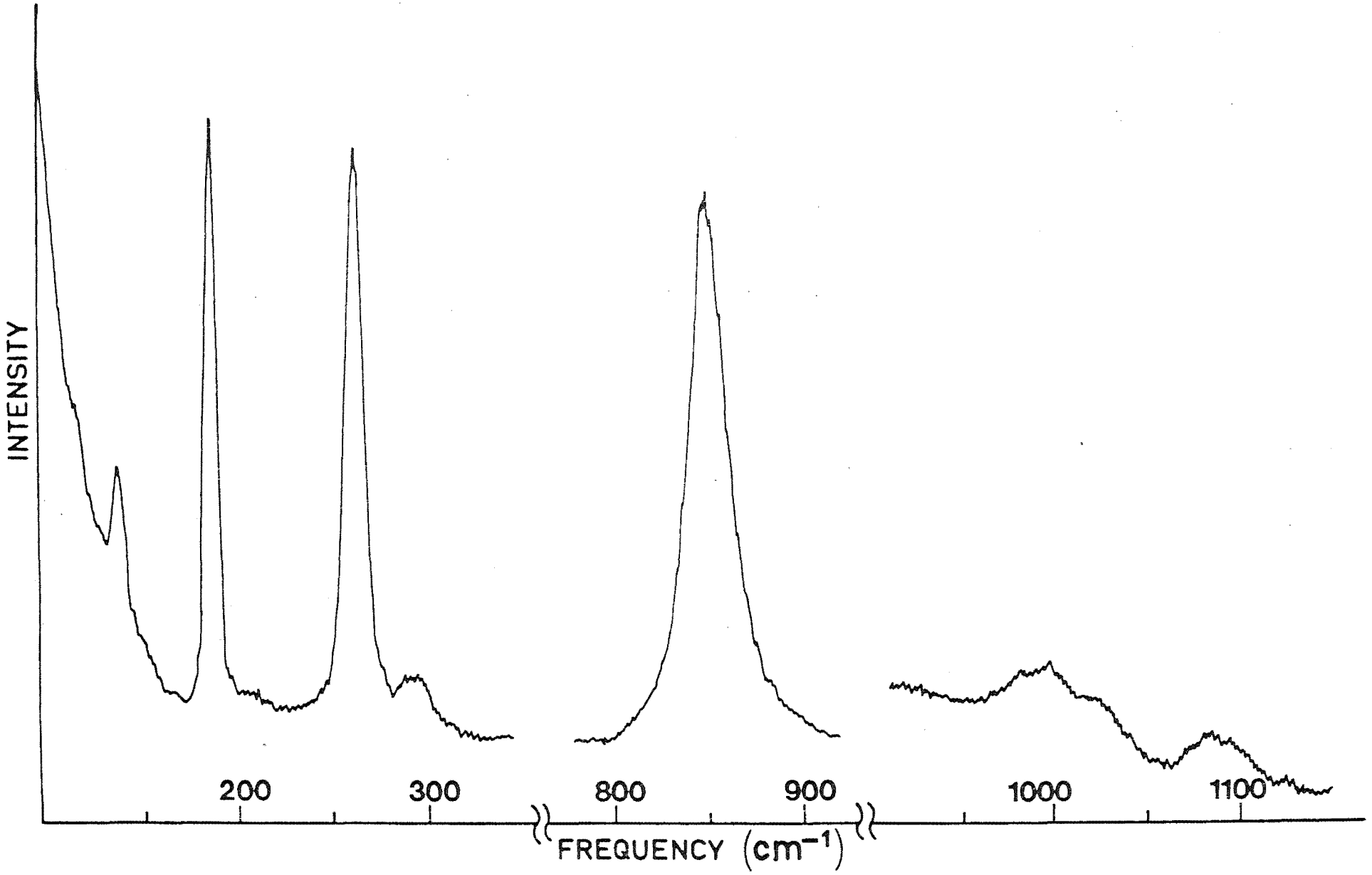

Fig. 8-4: Polarized infrared spectra of $CsCoCl_3$

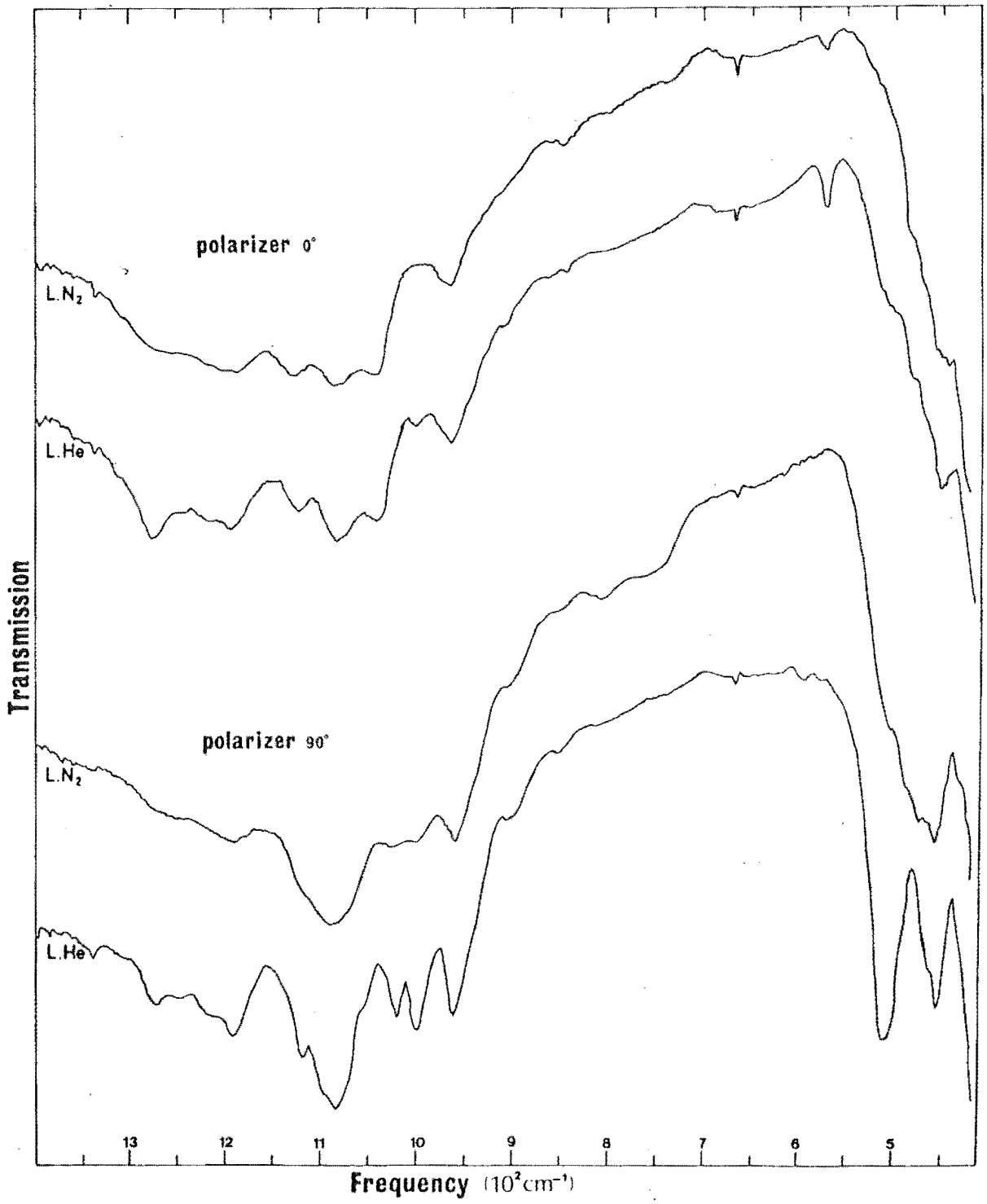

TABLE 8-2: Spectral data on $CsCoCl_3$. All measurements are in cm^{-1}.

Raman

L.N_2		L.He	
Frequency	Width	Frequency	Width
187±2	13	137±3	7
266±2	13	188±2	8
854±2	24	266±2	11
995±2	35	296±2	-
		851±1	16
		990±10	32
		1084±5	25

Infrared

Polarizer - 90°		Polarizer - 0°	
L.N_2 Frequency	L.He Frequency	L.N_2 Frequency	L.He Frequency
457±2	456±1	450±5	453±3
750±3	510±2	750±3	967±2
810±2	852±2	851±2	1003±1
853±2	905±2	972±2	1045±2
910±2	964±1	1047±2	1085±2
965±1	1001±1	1087±2	1123±2
1004±2	1023±1	1130±2	1195±2
1024±3	1085±2	1193±3	1220±2
1089±3	1118±1	1265±5	1278±2
1118±2	1192±2		
1192±2	1220±2		
1265±5	1263±2		

no axial samples of $CsCoCl_3$ could be prepared. These samples would need to be less than 1 mm thick because of the high molar extinction coefficient of $CsCoCl_3$[14], and their preparation would entail polishing in a direction normal to the cleavage planes. This is not feasible as these crystals are fragile.

Both the Raman and infrared spectra, recorded at liquid helium temperatures, exhibit no definite antiferromagnetic ordering effects. This is ascribed to insufficient cooling of the specimens to below the Neel temperature of 21.5°K.

8.2 $CsCdCl_3$:Co

8.2.1 Results

Earlier optical absorption studies on $CsCdCl_3$:Co have been undertaken by Gilmore[42] and Shaha et. al.[43]. In this work higher resolution axial and polarized spectra of this crystal were measured in the 18250 to 18700 cm^{-1} energy range at liquid-nitrogen and -helium temperatures. The crystals used contained nominal concentrations of 1 and 2.5 mole % of $CsCoCl_3$. Fig. 8-5 depicts the typical spectra recorded while the associated spectral data are listed in Table 8-3.

Fig. 8-5 reveals that the σ spectrum resembles that of the axial indicating that the transitions observed are electric dipole allowed. A similar result was found for the absorptions of the same crystal in the infrared region as reported in Sec. 6.3. The main feature of these two optical spectra is an intense broad band centred at around 18549 cm^{-1}. Several peaks appear on this band, the most prominent of which are the two sharp lines which peak at 18513 and 18501 cm^{-1}. In the low-energy region of these spectra are three weak bands at 18423, 18302 and 18286 cm^{-1}. In contrast the π spectrum is relatively featureless and only contains the remnants of the 18501 and 18286 cm^{-1} lines.

Fig. 8-5: Optical absorption spectra of $CsCdCl_3$:Co 2.5 mole % recorded at 15°K

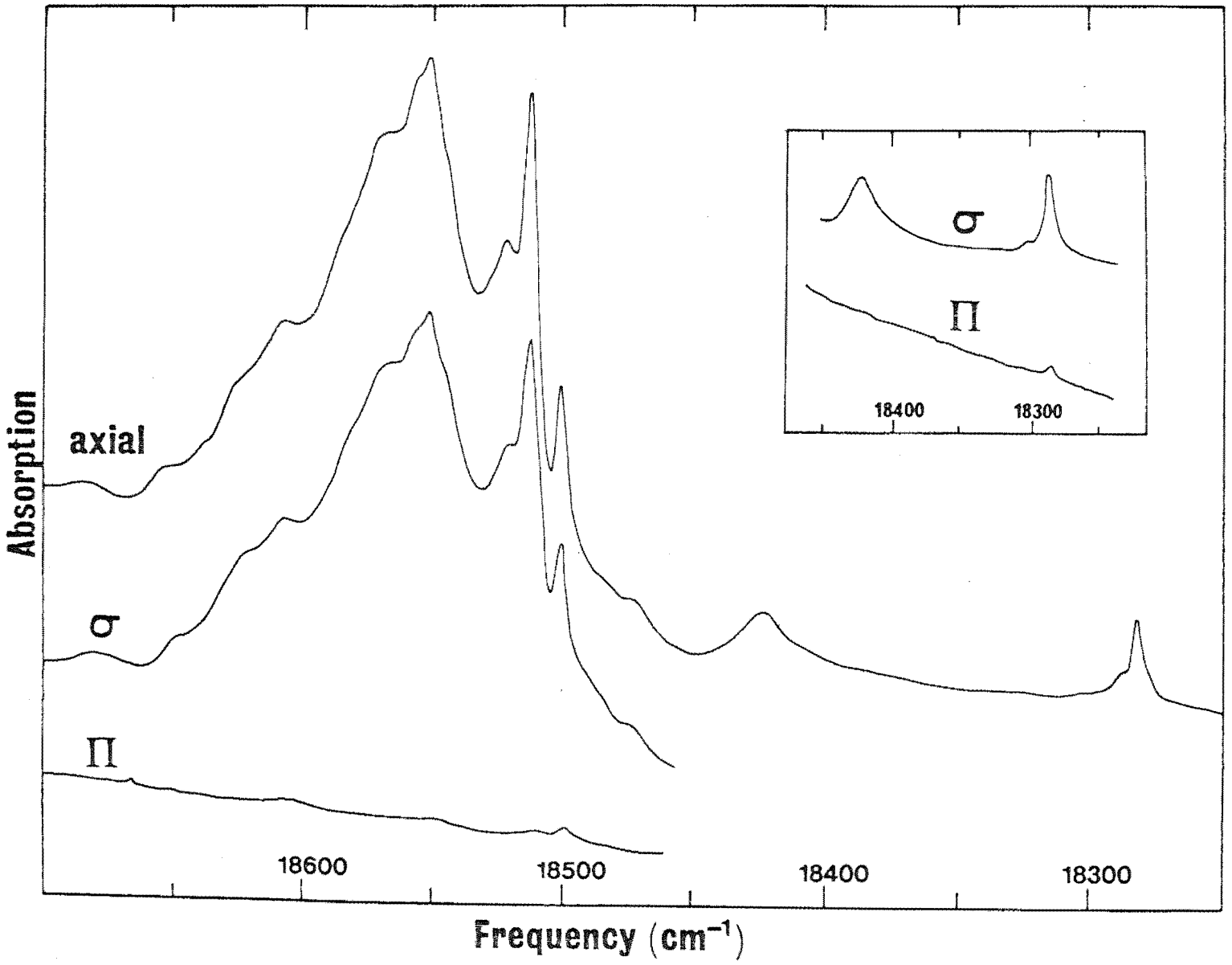

TABLE 8-3: Observed band frequencies (cm^{-1}) for the optical absorption spectra of $CsCdCl_3$:Co 2.5 mole % at 15°K.

Axial/σ	π
18286±3	18286±3
18302±7	-
18423±7	-
18471±7	-
18501±2	18501±2
18513±2	-
18520±3	-
18549±3	-
18567±7	-
18605±7	-
18622±7	-
18650±7	-
18678±14	-

TABLE 8-4: A tentative identification of the electronic lines and their associated vibronic bands of $CsCdCl_3$:Co.

Electronic parent	Vibronic	Vibronic interval
18286±3	18501±2	215±5
	18549±3	263±6
	18605±7	319±10
18302±7	18513±2	211±9
	18567±7	265±14
	18622±7	320±14

8.2.2 Analysis

Gilmore[42] observed bands at 18505 and 18550 cm^{-1} in his $5^{o}K$ spectra of randomly orientated $CsCdCl_3$:Co crystals. He assumed the cobalt ions to be in sites of predominantly cubic symmetry and attributed most of the structure of the band at 18550 cm^{-1} to the $^4T_1(^4F) \rightarrow {}^2T_1(^2P)$ electronic transition of the cobalt ions (Sec. 2.2).

Shaha et. al.[43] have reported a sharp band at 18550 cm^{-1} in the $20^{o}K$ polarized spectra of $CsCdCl_3$:Co. They assigned it as the spin forbidden transition to the doublet $^2T_1(^2G)$ state instead of the $^2T_1(^2P)$ state as assigned as Gilmore.

Zeeman-optical investigations of $CdCl_2$ crystals doped with cobalt ions have been carried out by Johnstone[44]. He obtained $1.3^{o}K$ spectra, each of which exhibits an intense broad band with several peaks on it, the strongest of which is at 19002 cm^{-1}. Weaker lines occur at lower energies. Among these are the 18823 and 18812 cm^{-1} lines which he ascribed to electronic transitions to the $\gamma_4^+(\Gamma_8^+)$ and $\gamma_{5,6}^+(\Gamma_8^+)$ states arising from a $^2T_{1g}$ cubic field term. The peaks on the broad band were identified as vibronic lines associated with these electronic levels.

The $CsCdCl_3$:Co spectrum of Fig. 8-5 is similar to that of $CdCl_2$:Co even though it is expected that the former will comprise strong electric dipole electronic transitions, while the latter is known to have relatively weak magnetic dipole electronic transitions. By analogy, the two lines at 18302 and 18286 cm^{-1} are tentatively assigned as the electronic transitions to the trigonal crystal field split components of the $\Gamma_8(^2T_1)$ state arising from either the ^2P or ^2G or ^2H cubic field multiplet. Their electric dipole character indicates that they are due to the Co^{2+} ions in the C_{3v} sites, consistent with the preponderance of these over those in the D_{3d} sites as established in Sec. 4.4.

Vibronic transitions associated with these two electronic levels could then be invoked to explain the stronger peaks appearing on the

intense broad band. These vibronic intervals are analysed to give frequencies of the peaks in the phonon density of states in the $CsCdCl_3$ host. However none of these vibronic intervals, listed in Table 8-4, match those obtained from an analysis of the infrared spectra of $CsCdCl_3$:Co. Hence the assignment of the lines at 18286 and 18302 cm^{-1} as being electronic in origin needs to be reconsidered. A Zeeman investigation is needed to verify this assignment.

CHAPTER IX

THE RAMAN AND INFRARED SPECTRA OF FERROUS IONS IN $CdCl_2$-TYPE CRYSTALS.

9.1 INTRODUCTION

A preliminary investigation of the Raman and infrared spectra of ferrous ions in $CdCl_2$ and $CdBr_2$ crystals was undertaken as a conclusion to this research project. There are several reasons for doing this. Firstly, the transitions of single cobalt ions are now well understood and it is appropriate to extend the investigation to the other ions of the transition-metal ion series. Secondly, the ferrous ion possesses an orbital triplet T_{2g} ground term which, just as for the Co^{2+} ion, can be split by the first order spin-orbit coupling. The ferrous ions are reasonably stable against oxidation and are quite readily accepted as impurities by $CdBr_2$ and $CdCl_2$.

In this chapter the results of this investigation are presented together with a tentative interpretation of the spectra obtained.

9.2 RESULTS OF $CdBr_2$:Fe

9.2.1 Raman Spectra

Raman scattering studies of $CdBr_2$ crystals containing nominal concentrations of 5 and 10 wt. % of $FeBr_2$ were done using the 4579, 4765, 4880 and 5145Å laser lines. Fig. 9-1 displays typical polarized Raman spectra recorded at $80^{o}K$.

Besides the 81 and 151 cm^{-1} phonon lines four other lines at 285, 497, 553 and 589 cm^{-1} appeared in the Raman spectra obtained. These four lines are weak, with the 285 cm^{-1} line being the weakest. Of these four lines, only the 285 cm^{-1} line appears in the Raman spectrum of Zn^{2+} -doped $CdBr_2$ and is therefore assigned as an impurity activated

Fig. 9-1: 80°K Raman spectra of four independent polarization configurations of a $CdBr_2$:Fe 5 wt. % crystal.

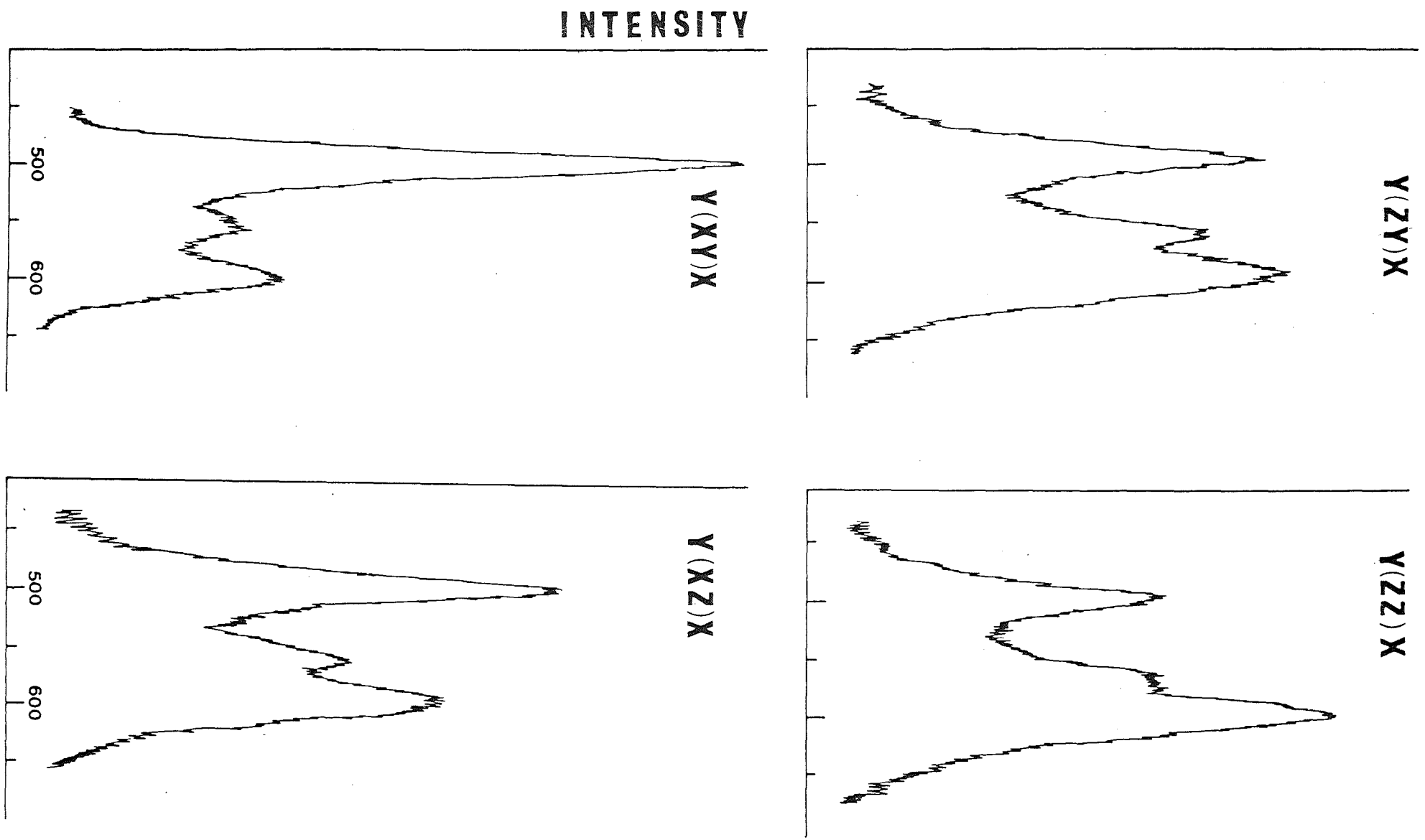

second-order phonon scattering line. The remaining lines at 497, 553 and 589 cm^{-1} are attributed to electronic transitions of the ferrous ions.

Since the 80°K Raman measurements were done, Tomblin[45] has carried out measurements at 15°K and obtained Raman lines at 491±1, 539±2, 550±1, 586±3 and 602±3 cm^{-1}. He also observed Raman lines at 492±1, 551±1, 591±3 and 603±5 cm^{-1} in the 40 kG ($\underline{H} \parallel \underline{c}$) Zeeman-Raman spectrum of $CdBr_2$:Fe recorded at 2°K.

9.2.2 Infrared Spectra

Infrared measurements of $CdBr_2$ crystals doped with nominal concentrations of 2.5, 5 and 10 wt. % of $FeBr_2$ were recorded at liquid-nitrogen and -helium temperatures. The spectra of all these crystals exhibit similar features and representative axial and polarization spectra, obtained at 80°K, are shown in Fig. 9-2. The liquid helium spectra of $CdBr_2$:Fe 5 wt. % exposed to 0, 20 and 40 kG fields are depicted in Fig. 9-3. Table 9-1 and 9-2 list the spectral data.

The spectra were measured over the 300 - 1500 cm^{-1} energy range within which $CdBr_2$ is transparent down to 320 cm^{-1}. Each of the 80°K spectra exhibits an intense wide band with structure on it. On the lower energy side of this band are lines at 493 and 551 cm^{-1} which appear only in the axial and σ spectra. These absorptions do not appear in the spectra of cobalt-doped $CdBr_2$ and are therefore attributed to iron. The 493 and 551 cm^{-1} lines match two of the Raman lines to within 2 cm^{-1} and are therefore identified as electronic lines. The similarity of the axial and σ spectra indicates that all the absorption features of the spectra are electric dipole in nature.

On cooling to 15°K, the peaks of the two electronic lines shifted to 491.0 and 547.5 cm^{-1}. Additional lines appeared at 605, 621 and 640 cm^{-1} and the broad band now has a weak shoulder at 790 cm^{-1}. The

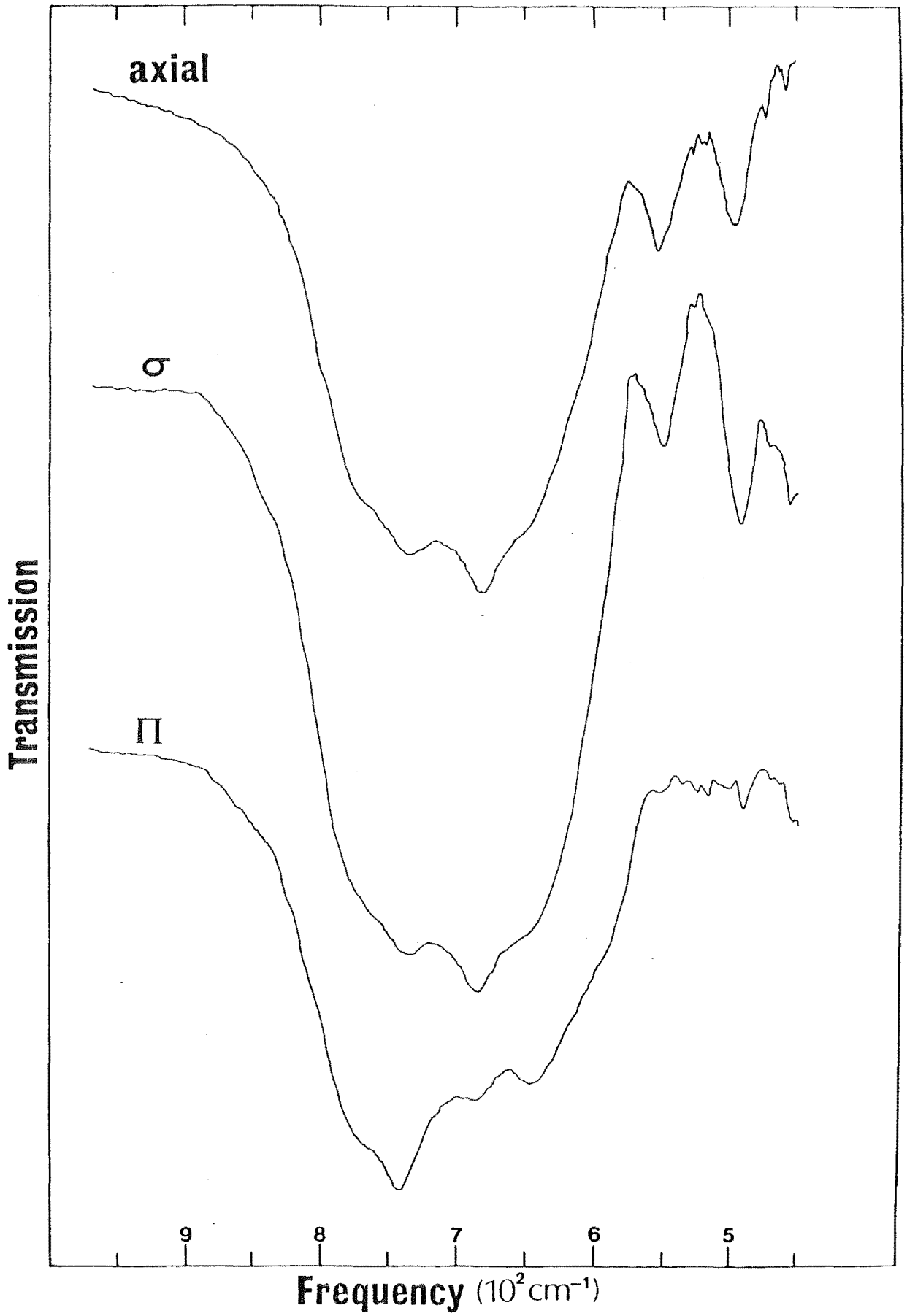

Fig. 9-2: Infrared spectra of $CdBr_2$:Fe 5 wt. % measured at 80°K.

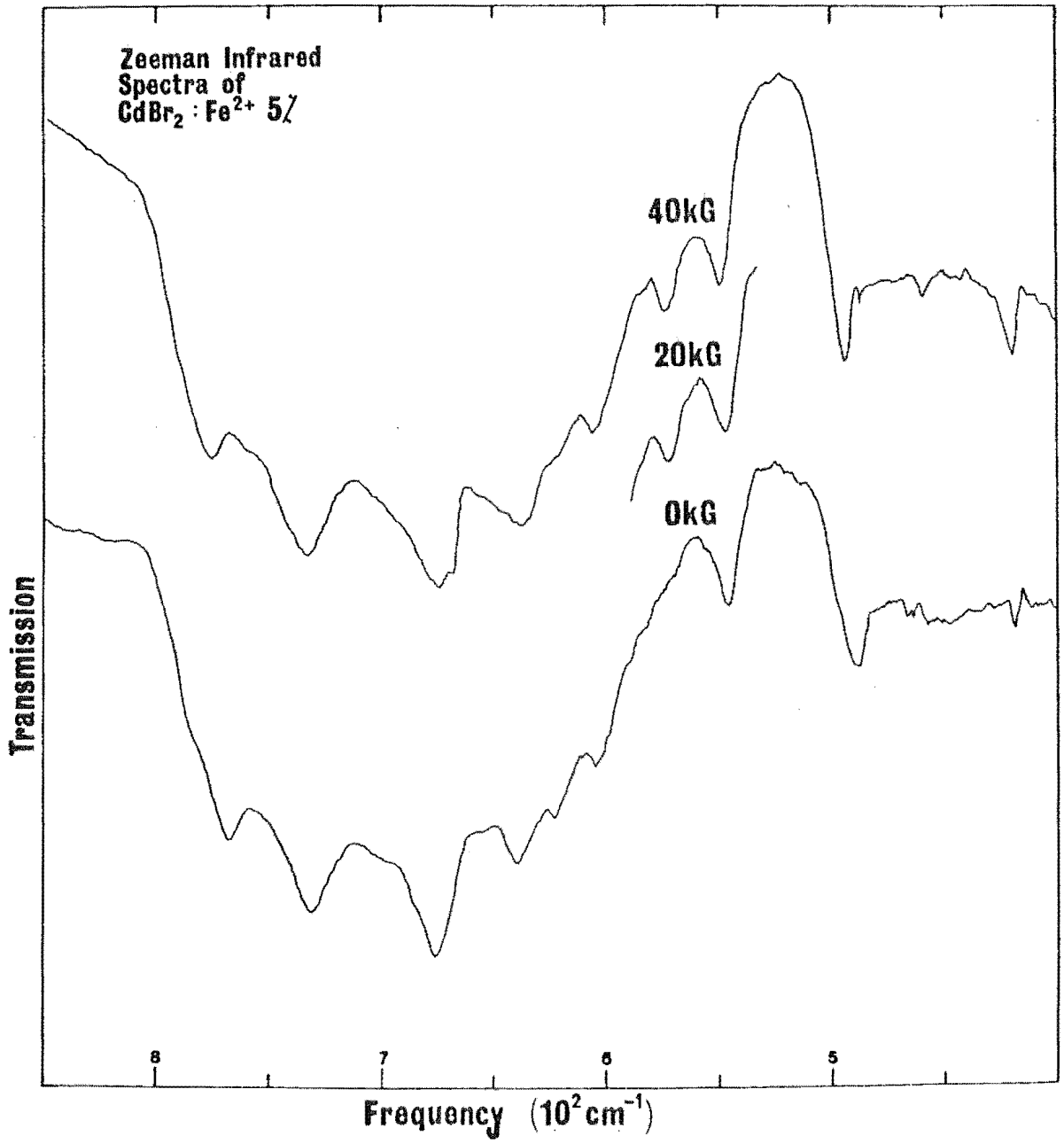

Fig. 9-3: Zeeman axial ($\underline{H} \parallel \underline{c}$) infrared spectra of $CdBr_2$:Fe 5 wt. % measured at 15°K

TABLE 9-1: Infrared axial and polarisation 80°K data on $CdBr_2$ containing a nominal doping of 10 wt.% of $FeBr_2$. All measurements are in cm^{-1}.

Axial		σ		π	
Freq.	Width	Freq.	Width	Freq.	Width
493±1	25	493±1	23	-	-
551±1	22	551±1	23	-	-
683±2	160	684±2	165	645±3	190
736±3		735±3		740±3	
770±5		770±5		770±5	

TABLE 9-2: Zeeman-infrared axial ($\underline{H} \| \underline{c}$) data on $CdBr_2$ containing a nominal doping of 5.0 wt.% of $FeBr_2$. All measurements were made at 15°K and are in units of cm^{-1}.

0 kG		40 kG		20 kG	
Freq.	Width	Freq.	Width	Freq.	Width
491.0±0.7	16	493.5±0.7	10		
547.5±0.7	12	550.0±0.7	14	548.5±0.7	16
-	-	573.5±0.7	11	574 ±1	11
605 ±1	180	607 ±1	160		
621 ±2		622 ±2			
640 ±2		639 ±2			
676 ±2		677 ±2			
732 ±2		733 ±2			
769 ±2		775 ±2			
790 ±5					

605 cm^{-1} line also appears in the 15°K Raman spectrum measured by Tomblin and so is ascribed to an electronic transition of iron.

The 676, 732 and 790 cm^{-1} bands are each separated by 185 cm^{-1} from the 491.0, 547.5 and 605 cm^{-1} electronic lines respectively, and are therefore assigned as vibronic bands of these respective electronic lines. The 769 cm^{-1} band is separated by 182±5 cm^{-1} from the electronic transition at 586 cm^{-1} detected by Raman scattering, so it is identified as a vibronic band. The vibronic interval of 185 cm^{-1} is in good agreement with the value of 183.3±1.5 cm^{-1} obtained from a vibronic analysis of $CdBr_2$:Co by Johnstone and Jones[37].

Fig. 9-3 of the Zeeman spectra shows that the absorptions shifted to higher frequencies under a 40 kG field thus confirming their electronic and vibronic nature. Of particular interest is the 573.5 cm^{-1} line that only appeared in the presence of a magnetic field. Because its frequency and separation from the electronic line at 550 cm^{-1} remained unchanged at 20 kG, it is unlikely that these two lines are Zeeman split components of a single electronic state. These two lines did not change in intensity as the magnetic-field was altered from 20 to 40 kG.

The zero-field energy separation of 184 cm^{-1} is maintained at 40 kG between the 677 and 732 cm^{-1} vibronic bands and their respective electronic parent lines at 493.5 and 550.0 cm^{-1}. An additional weak absorption appeared at 759 cm^{-1} and is 186±4 cm^{-1} from the 573.5 cm^{-1} line, which suggests that the latter is an electronic line. From the shift estimated from its 769 cm^{-1} vibronic band, the 586 cm^{-1} electronic Raman line was predicted to peak at 592 cm^{-1} at 40 kG. This was verified by Tomblin who observed an electronic Zeeman-Raman line at 591±3 cm^{-1} at 40 kG.

9.3 RESULTS OF $CdCl_2$:Fe

A cursory investigation of $FeCl_2$ -doped $CdCl_2$ crystals was performed. The 80^oK Raman spectrum features two broad bands centred at 459 and 570 cm^{-1} which are attributed to electronic transitions of the ferrous ion as they are absent in the spectra of $CoCl_2$ -doped $CdCl_2$. The 80^oK infrared spectra were recorded from 1500 cm^{-1} down to the absorption band edge of the host lattice at 450 cm^{-1}. The infrared spectrum is relatively featureless, having only an intense broad band centred at around 750 cm^{-1}. As this band is not present in the spectra of $CdCl_2$:Co, it is assigned as a vibronic band of the ferrous ion.

These spectra are too broad and featureless for any detailed analysis to be carried out.

9.4 ANALYSIS OF THE ELECTRONIC TRANSITIONS OF THE FERROUS ION IN $CdBr_2$

The ferrous ion possesses the $[Ar]\,3d^6$ configuration whose only quintet term ^5D is the ground term. In an octahedral crystal field the ^5D term splits into an upper doublet ^5E_g and a lower triplet $^5T_{2g}$. The spin-orbit interaction splits the $^5T_{2g}$ ground manifold into $\Gamma_1^+, \Gamma_3^+, 2\Gamma_4^+$ and $2\Gamma_5^+$ states, with a Γ_5^+ state lowest[46]. A Γ_4^+ triplet and a Γ_3^+ doublet lie at an energy -2λ above the Γ_5^+ ground state while higher up at -5λ, lie a Γ_1^+ singlet and two triplets $\Gamma_4'^+$ and $\Gamma_5'^+$. Here λ is the spin-orbit coupling constant, which is related to the single electron spin-orbit parameter ξ by $\lambda = -\frac{\xi}{4}$. Inclusion of the trigonal cyrstal field raises the degeneracies further. It splits the Γ_4^+ and Γ_5^+ triplets into states labelled by the γ_2^+, γ_3^+ and γ_1^+, γ_3^+ irreps, while the Γ_1^+ singlet and the Γ_3^+ doublet become the γ_1^+ and γ_3^+ states respectively of the D_{3d} group.

From EPR studies of divalent iron in $CdCl_2$, Trapp et.al.[47] have determined that the Γ_5^+ ground state is split by the trigonal crystal

field into a γ_1^+ singlet and a γ_3^+ doublet, with the latter lying 2.9 cm^{-1} below the former. Because $CdBr_2$ is isostructural with $CdCl_2$, it is reasonable to assume that the γ_3^+ doublet also lies lowest for $CdBr_2$:Fe.

Several workers have reported evidence of the Jahn-Teller effect in their work with divalent iron. Among them are Ray et.al.[48] who studied the far infrared spectra of $KMgF_3$:Fe and Freeman et.al.[49] who performed optical studies on Fe^{2+} ions in $CdCl_2$ -type crystals. Manifestations of the Jahn-Teller distortion were observed in the optical spectra of $CsCdCl_3$:Fe by Shaha et.al.[50]. The Jahn-Teller theorem[51] states that a system with an orbitally degenerate ground state will be unstable. A distortion, which will lift this degeneracy, will lower the energy of the system.

No electric dipole electronic transitions are allowed for transition-metal ions in the centrosymmetric D_{3d} sites of $CdBr_2$ and the electronic transitions of cobalt ions in these sites were found to be magnetic dipole allowed[37]. However Fig. 9-2 reveals that the lines due to the electronic transitions of the ferrous ions in $CdBr_2$ are electric dipole in character. This can only be accounted for by a lowering in the D_{3d} ferrous ion site symmetry to a noncentrosymmetric one. As the Fe^{2+} ion has a γ_3^+ doublet lowest, such a distortion could occur through the Jahn-Teller effect resulting in the lifting of the degeneracy of this γ_3^+ ground state.

The evidence for the Jahn-Teller effect in $CdBr_2$:Fe is the occurrence of electric dipole electronic transitions. These transitions are not much stronger than the magnetic dipole electronic transitions observed for $CdBr_2$:Co and so any static Jahn-Teller distortion present is small, and would only cause a small splitting of the γ_3^+ ground state. In their EPR studies of $CdCl_2$:Fe, Trapp et.al.[47] did not detect any splitting in the ground state of the Fe^{2+} ion. To all intents and purposes therefore, the D_{3d} trigonal crystal field determines the

energy level pattern of the Fe^{2+} ions in $CdBr_2$. Because electric dipole electronic transitions were observed, the actual Fe^{2+} ion site symmetry lacks inversion. This means that the states of the Fe^{2+} ions can be labelled by the irreps of the D_3 group which have no parity labels. The D_3 group was chosen because it is the highest subgroup of D_{3d} that has no centre of symmetry. More over a crystalline field of D_3 symmetry has the same even terms as that of D_{3d} symmetry. Fig. 9-4 displays the schematic energy levels of the Fe^{2+} ion in $CdBr_2$.

The zero-field 15°K electronic Raman spectrum obtained by Tomblin comprises a narrow intense line at 491 cm^{-1} and two broad bands, each of which was resolved into two components. One band has components at 539 and 550 cm^{-1} while the other at 586 and 602 cm^{-1}. On the basis of the Zeeman-infrared measurements reported below, the former and latter pairs of components are assigned to electronic transitions to the trigonal crystal field levels of the spin-orbit Γ'_4 and Γ'_5 triplets viz., $\gamma_3(\Gamma'_4)$, $\gamma_2(\Gamma'_4)$ and $\gamma_3(\Gamma'_5)$, $\gamma_1(\Gamma'_5)$ respectively. Fig. 9-4 shows the Γ'_4 triplet as being lower in energy than the Γ'_5 triplet but the alternative assignment, where the Γ'_5 triplet is lower, would be equally valid. The following argument is equally applicable for either assignment. The 491 cm^{-1} is assigned as the electronic transition to the spin-orbit Γ_1 state.

An interpretation of the infrared spectra is now attempted. As mentioned above the Jahn-Teller distortion, which would split the γ_3 ground state doublet, could account for the electric dipole electronic transitions of $CdBr_2$:Fe. In order to lift the degeneracy of this ground state, the D_{3d} ferrous ion site symmetry has to be reduced to at least C_{2h} and for electric dipole electronic transitions to occur, this C_{2h} symmetry needs to be further reduced to C_2. For such a low symmetry, electronic transitions to all the excited states are allowed from either of the two components of the γ_3 ground state. However the lines of the

Fig. 9-4: Schematic diagram of the splitting of the $^5T_{2g}(^5D)$ ground term of the Fe^{2+} ion in $CdBr_2$.

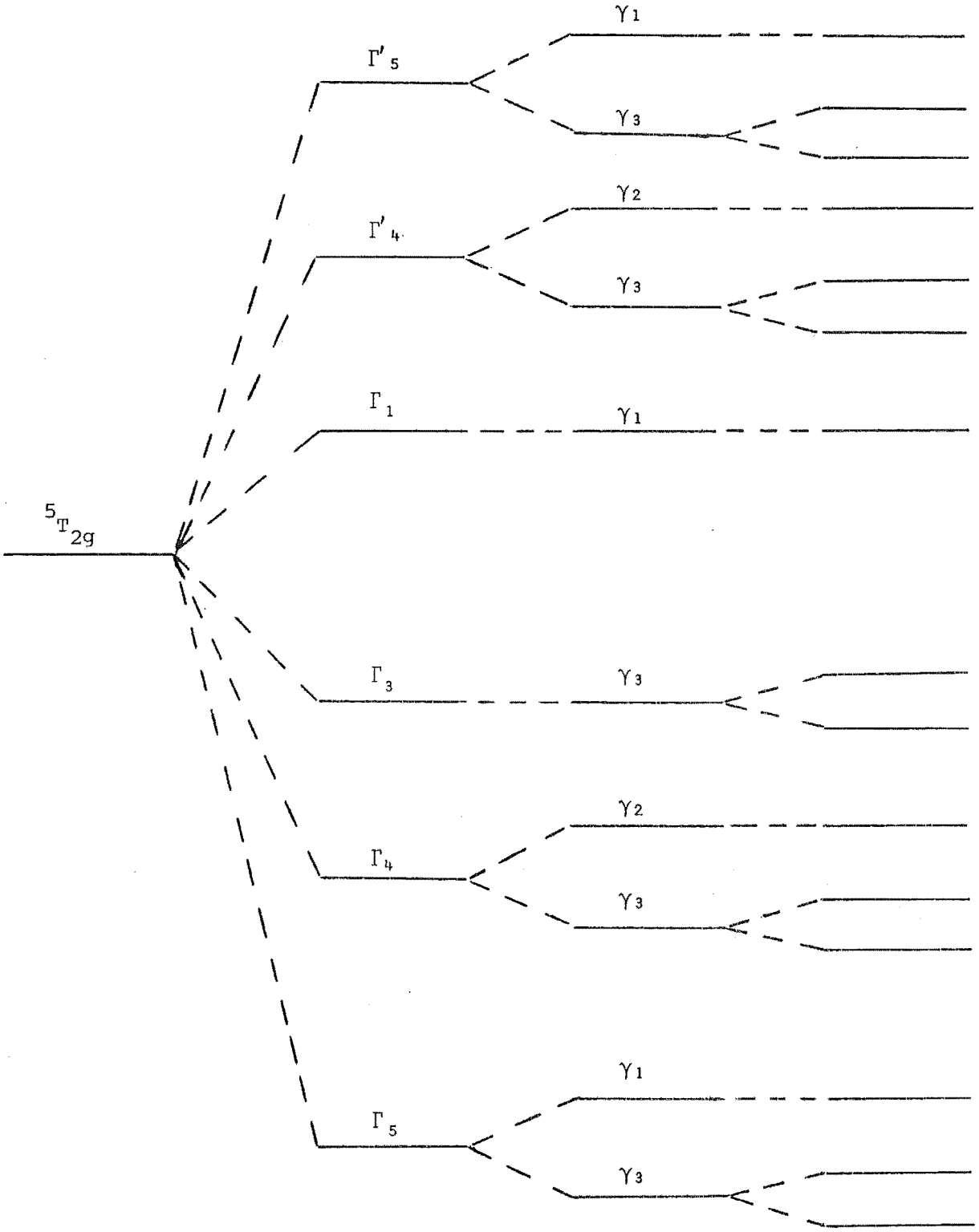

infrared spectra show polarization indicative of a higher effective symmetry. This is reasonable as the C_2 symmetry site would only be a slight modification of the D_{3d} symmetry site. The polarization selection rules were therefore derived for a D_3 symmetry.

In the D_3 group, the x,y and z components of the electric dipole transition operator transform like γ_3 and γ_2 respectively. For axial and σ spectra, the relevant direct product

$$\gamma_3 \times \gamma_3 = \gamma_1 + \gamma_2 + \gamma_3 \tag{9.1}$$

indicates that all electronic transitions are allowed from the $\gamma_3(\Gamma_5)$ ground state. However only the transitions to the $\gamma_1(\Gamma_1)$, $\gamma_2(\Gamma'_4)$ and $\gamma_1(\Gamma'_5)$ states, which were assigned as having frequencies of 491.0, 547.5 and 605 cm^{-1} respectively, were detected. Transitions to the remaining $\gamma_3(\Gamma'_4)$ and $\gamma_3(\Gamma'_5)$ states were not observed due presumably to their weak intensity. Transitions from the $\gamma_1(\Gamma_5)$ state, which is just above the ground state, are expected but are weak because of its partial depopulation at 15°K.

No electronic transitions were seen in the π spectra. From the product representation,

$$\gamma_3 \times \gamma_3 = \gamma_3 \tag{9.2}$$

it follows that transitions from the $\gamma_3(\Gamma_5)$ ground state to the excited singlet levels are forbidden in the π spectra. Non-observation of transitions to the $\gamma_3(\Gamma'_4)$ and $\gamma_3(\Gamma'_5)$ levels is, as for the axial and σ spectra, ascribed to their weak intensity.

Due to insufficient information on the Fe^{2+} ion site symmetry, no selection rules governing the electronic Zeeman-infrared transitions were derived. When a 40 kG field was applied along the crystal c axis, a shift of 2.5 cm^{-1} up in energy was recorded for each of the three zero-field 491.0, 547.5 and 605 cm^{-1} electronic lines. Because of their

identical Zeeman shifts, these lines are assigned as electronic transitions to the $\gamma_1(\Gamma_1)$, $\gamma_2(\Gamma'_4)$ and $\gamma_1(\Gamma'_5)$ levels respectively. These singlet levels are unaffected by the magnetic field and any shift in frequency of the transitions to them is due to a shift in the energy of the lower component of the $\gamma_3(\Gamma_5)$ ground state. A $g_{\|}$ value of 2.6±0.5 is evaluated for the $\gamma_3(\Gamma_5)$ ground state of $CdBr_2$:Fe from this shift. Trapp et.al.[47] estimated the $g_{\|}$ value of the ground state of $CdCl_2$:Fe at 3.68±0.05. A shift of 5 cm^{-1} was measured for the zero-field electronic 586 cm^{-1} line in the 40 kG Zeeman-Raman spectrum recorded by Tomblin. This line is assigned as the electronic transition to the upper component of the $\gamma_3(\Gamma'_5)$ doublet.

The $2^{o}K$ Zeeman-Raman ($\underline{H} \| \underline{c}$) spectrum does not contain the 574 cm^{-1} line which appears in the Zeeman-infrared ($\underline{H} \| \underline{c}$) spectrum. This line could be attributed to the electronic transition that originated from the upper component of the $\gamma_3(\Gamma_5)$ ground doublet and terminated on the lower component of the $\gamma_3(\Gamma'_5)$ excited doublet. Depopulation of the former component at $2^{o}K$ would account for the absence of the 574 cm^{-1} line in the Zeeman-Raman spectrum. Further work is required to definitely assign this line.

CHAPTER X

OVERALL SUMMARY AND CONCLUSION

Raman scattering and infrared absorption techniques have been successfully employed to obtain spectra of divalent cobalt ions in $CsMgCl_3$ and $CsCdCl_3$. These spectra exhibit electronic lines due to transitions between the spin-orbit and trigonal crystal field levels of the $^4T_{1g}(^4F)$ ground manifold of the cobalt ion. All five single ion electronic transitions were observed for $CsMgCl_3$:Co, while only three electronic transitions were detected for $CsCdCl_3$:Co(2). A crystal field fit was performed using all the 120 states of the $3d^7$ configuration and agreement to within experimental accuracy was achieved. Oscillator strengths for the magnetic dipole electronic transitions of $CsMgCl_3$:Co were computed using crystal field theory and were found to be sufficiently close to those measured from experiment, to substantiate the identification of these transitions as magnetic dipole in character.

First- and second-order phonon scattering in the Raman spectra of $CsMgCl_3$ and $CsCdCl_3$ hosts has been identified. Vibronic absorptions in the infrared spectra were analysed to give frequencies of peaks in the phonon density of states of these two hosts.

Zeeman-Raman and -infrared investigations were also carried out on the $CsMgCl_3$:Co and $CsCdCl_3$:Co systems. Selection rules, governing the occurrence of electronic transitions between the lowest twelve Zeeman levels, were derived using the group multiplication tables of the appropriate cobalt ion site symmetries. These rules were found to be in agreement with observation. The Zeeman splittings and shifts observed provided information on the magnetic splitting factors of the excited electronic states. The crystal field model was again utilized to evaluate the frequencies and oscillator strengths (for $CsMgCl_3$:Co) of the electronic Zeeman transitions and also the excited state g values. The close agreement between the predicted values of these quantities and

those measured from experiments affirms the adequacy of the crystal field theory for the two systems examined. The Zeeman patterns of the vibronic bands were found to be similar to that of their associated electronic parent lines, thus confirming their identification as vibrationally induced absorptions.

On the experimental side, several improvements and modifications on the existing Zeeman-Raman and -infrared equipment are suggested. The non-observation of splittings of the Zeeman-Raman electronic lines is partly ascribed to the depopulation of the upper component of the zero-field ground state. This could be avoided if the specimens are not cooled to liquid helium temperatures by e.g., enclosing them in an evacuated quartz tube. Problems with the low signal-to-noise ratio of the Zeeman-Raman arrangement could be surmounted if the collection optics used were more efficient. One solution is to mount a convex lens in front of the solenoid's bore so as to collect more of the scattered radiation, thus permitting more of it to pass through the B.O.C. cryostat's windows.

At present Zeeman-infrared spectral runs are restricted to cases where the magnetic field is applied along the infrared radiation beam. A split-solenoidal magnet, similar to the B.O.C. one would permit the field to be directed at right angles to the radiation beam. Electronic Zeeman transitions, which would otherwise be forbidden, could then be observed.

Raman and infrared spectra of $KCdCl_3$:Co and $CsCoCl_3$ were also recorded. However no crystal field analysis was attempted due to lack of experimental data. Further work on the $CsCoCl_3$ crystals would be worthwhile in view of the well-defined polarization of their infrared spectra and also the expected spectral effects due to antiferromagnetic ordering.

An optical investigation of $CsCdCl_3$:Co has been performed and a

tentative interpretation of the spectra given. Zeeman studies are needed to verify the assignment proposed.

A preliminary research into the transitions of the ferrous ion was undertaken as a continuation to the spectral studies of the cobaltous ion. Electronic transitions within the $^5T_{2g}(^5D)$ cubic field ground term were observed using Raman and infrared spectroscopy. Infrared measurements reveal that the electronic transitions are principally electric dipole polarized, inferring that the expected inversion symmetry of the ferrous ion sites is not present. This is an indication that the Jahn-Teller effect is operative. A $g_{||}$ value of 2.6±0.5 for the trigonal crystal field ground state of $CdBr_2$:Fe was inferred from Zeeman-infrared studies. A tentative analysis of the spectra recorded has been proposed. This research project is still at its infancy and further work is necessary to fully understand these spectra.

REFERENCES

1. J.R. Chang, G.L. McPherson and J.L. Atwood: Inorg. Chem. 14(12), 3079 (1975).
2. G.L. McPherson, T.J. Kistenmacher and G.D. Stucky: J.Chem.Phys. 52(2), 815 (1970).
3. H. Soling: Acta Chem. Scand. 22(9), 2793 (1968).
4. H.E. Swanson, H.F. McMurdie, M.C. Morris and E.H. Evans: Nat.Bur. Stand. (U.S.) Monograph 25, Sec. 6, 38 (1967).
5. R.W.G. Wyckoff: 'Crystal Structures' 2nd Edition (John Wiley and Sons, 1964) p.430.
6. W.E. Smith: J. Chem. Soc. (A), 18, 2677 (1969).
7. K. Ono, A. Ito and T. Fujita: J. Phys. Soc., Japan, 19, 2119 (1964).
8. G.F. Koster: 'Properties of the Thirty-two Point Groups' (M.I.T. Press, Massachusetts, 1963).
9. I.W. Johnstone: Ph.D. Thesis, University of Canterbury (1975).
10. Y. Tanabe and S. Sugano: J. Phys. Soc., Japan, 9, 753 (1954).
11. W.A. Runciman and K.A. Schroeder: Proc. Roy. Soc. (London), A265, 489 (1962).
12. C.J. Ballhausen: 'Introduction to Ligand Field Theory' (McGraw-Hill, 1962), p.105.
13. I. Rollerson: M.Sc. Thesis, University of Canterbury (1970).
14. A. Trutia and M. Lebl: Kristall und Technik, 4(1), 129 (1969).
15. The Merck Index (Merck and Co. Inc., New Jersey, 1968).
16. F.D. Bloss: 'An Introduction to the Methods of Optical Crystallography' (Holt, Rinehart and Winston, Inc. 1966) p.109.
17. D.J. Lockwood: Ph.D. Thesis, University of Canterbury (1969).
18. J.H. Christie: Ph.D. Thesis, University of Canterbury (1973).
19. J. Loader: 'Basic Laser Raman Spectroscopy', (Heydon and Son Ltd. 1970) p.32-35.

20. J. Hougen and S. Singh: Phys. Rev. Letters, 10, 406 (1963).

21. T.C. Damen, S.P.S. Porto and B. Tell: Phys. Rev., 142, 570 (1966).

22. J.E. Kardontchik, E. Cohen, J. Makovsky: Phys.Rev.B, 13(7), 2955 (1976)

23. A. Kiel and S.P.S. Porto: J. Mol. Spec. 32, 458 (1969).

24. A. Chadwick, J.T.R. Dunsmuir, I.W. Forrest, A.P. Lane and S. Fernando: J. Chem. Soc. (A), 2794 (1971).

25. G.L. McPherson and J.R. Chang: J. of Magnetic Resonance, 14, 310 (1974).

26. S.O. Graham and R.L. White: Phys. Rev. B, 10(11), 4505 (1974).

27. A. Edgar: J. Phys. C., 9, 4303 (1976).

28. C.K. Asawa, R.A. Satten and D.N. Stafsudd: Phys. Rev., 168, 957 (1968).

29. J.C. Christie, I.W. Johnstone, G.D. Jones and K. Zdansky: Phys. Rev. B., 12(11), 4656 (1975).

30. D.J. Newman: Adv. Phys., 20, 197 (1971).

31. A.B. Robson: M.Sc. Thesis, University of Canterbury (1969).

32. C.W. Tomblin: M.Sc. Thesis, University of Canterbury (1977).

33. H. Rinneberg and H. Hartmann: J. Chem.Phys., 52(11), 5814 (1970).

34. D.S. McClure: 'Electronic Spectra of Molecules and Ions in Crystals' (Academic Press, New York and London, (1959)), p.87.

35. E.C. Hsu and J.W. Stout: J. Chem. Phys., 59, 502 (1973).

36. D.L. Dexter: 'Solid State Physics' (Academic Press, New York and London, (1958)), p.370.

37. I.W. Johnstone and G.D. Jones: Phys. Rev. B. 15(3), 1297 (1976).

38. M.D. Sturge and H.J. Guggenheim: Phys.Rev.B. 4(7), 2092 (1971).

39. R.A. Satten, D.R. Johnston and E.Y. Wong: Phys.Rev. 171(2), 370 (1968).

40. M. Melamud, H. Pinto, J. Makovsky and H. Shaked: Phys.Stat.Sol.(b), 63, 699 (1974).

41. R.M. Barr and M. Goldstein: J.Chem.Soc., Dalton Trans., 1180 (1974).

42. F.C. Gilmore: Ph.D. Thesis, University of Tennessee, (1969), University Microfilms, Inc., Ann Arbor, Michigan.

43. R.K. Shaha, R.K. Mukherjee and A.Bose: Indian J. Phys., 43, 775, (1969).

44. I.W. Johnstone: J. Phys. C., Solid State Phys. To be published.

45. C.W. Tomblin: Private communication.

46. W. Low and M. Weger: Phys. Rev., 118(5), 1119 (1960).

47. C. Trapp, D. Smith and R. Johnson: J. Chem. Phys.55(11),(1971).

48. T. Ray, J.R. Regnard, J.M. Laurant and A. Ribeyron: Solid State Commun. 13, 1959 (1973).

49. T.E. Freeman and G.D. Jones: Phys. Rev. 182(2), 411 (1969).

50. R.K. Shaha and A. Bose: Indian J. Phys., 44, 59 (1970).

51. H.A. Jahn and E. Teller: Proc. Roy. Soc., (London), A161, 220 (1937).

APPENDIX

The programs Oscstrengths/H120 and Oscstrengths/H3942 are written in the B6700 Fortran language and appear on the following pages. The former incorporates the entire 120-dimension energy matrix and is used for $\underline{H} \perp \underline{c}$. In the latter, which is used for $\underline{H} \parallel \underline{c}$, the energy matrix comprises two 39-dimension $\gamma_4^+(-\frac{1}{2})$ and $\gamma_4^+(+\frac{1}{2})$ block matrices and a 42-dimension $\gamma_{5,6}^+$ block matrix. They are both used for computing the frequencies, magentic-dipole oscillator strengths and the g values of the lowest 12 crystal field levels of the Co^{2+} ion from the crystal field parameters for any magnetic field strength.

```
0   FILE  61=OURS/H120,UNIT=DISK,RECORD=7260,AREA=13*1,SAVE=1
1   C
2   C     ***************************************************************************
3   C     MAIN PROGRAM
4   C     CALCULATES OSCILLATOR STRENGTHS FOR CRYSTAL FIELD SPLIT LEVELS
5   C     ***************************************************************************
6         DIMENSION R(7260),F(7260),P(10),S(14400),EC(120),T(1440),
7        CA(12,12)
8    501  FORMAT(6F20.8)
9   1000  FORMAT(7F10.2)
10  1001  FORMAT('  INPUT PARAMETERS ARE :        '/)
11  1002  FORMAT(/10F12.4/)
12  1003  FORMAT(/'  ENERGY LEVELS ARE  :  '/)
13  1004  FORMAT(/10F12.4/)
14  1005  FORMAT(/'   EIGENVECTORS ARE  :   '/)
15  1006  FORMAT(/20F6.3)
16  1007  FORMAT(' MATRIX ELEMENT,ITS SQUARE,ASSOC. EIGENVAL. LABEL '/)
17  1008  FORMAT(/5F20.8,I10)
18   1010 FORMAT(1HO,X,27HMAGNETIC FIELD IN KILOGAUSS,F10.6)
19   1011  FORMAT(F10.4)
20  1111  FORMAT(/6F20.9)
21   1112 FORMAT(1HO,5F20.6,2I10)
22        READ(5,1000) (P(I),I=1,7)
23        WRITE(6,1001)
24        P(8)=-P(4)/535.00
25        P(9)=-P(5)/535.00
26        P(10)=2.0
27        WRITE(6,1002) (P(I),I=1,10)
28        P(6)=P(6)*0.8164965809
29        P(7)=P(7)*1.414213562
30        READ(5,1011) FIELD
31        WRITE(6,1010) FIELD
32        FX=FIELD*0.046685
33        DO 100 I=1,7260
34  100   R(I)=0.0
35        DO 200 LL=1,7
36        WRITE(6,1009) LL
37  1009  FORMAT(/'****',I1)
38        DO 300 I=1,7260
39  300   F(I)=0.0
40        READ(61=LL) F
41        DO 200 J=1,7260
42        F(J)=F(J)*P(LL)
43  200   R(J)=R(J)+F(J)
44        DO 250 KL=8,10
45        LL=KL+3
46        DO 350 I=1,7260
47    350 F(I)=0.0
48        READ(61=LL) F
49        DO 250 J=1,7260
50        F(J)=F(J)*P(KL)*FX
51    250 R(J)=R(J)+F(J)
52        CALL EIGEN(R,S,120,0)
53        DO 10 K=1,1440
54  10    T(K)=S(108*120+K)
55        DO 20 K=1,1440,6
56        KMAX=K+5
57    20  WRITE(6,501) (T(I),I=K,KMAX)
58        WRITE (6,1003)
59        DO 400 I=1,120
```

```
      IP=I*(I+1)/2
400   EC(I)=R(IP)-R(7260)
      WRITE(6,1004) (EC(I),I=1,120)
      DO 1400 LO=1,3
      DO 600 I=1,7260
600   R(I)=0.0
      DO 700 KL=8,10
      IF(LO.EQ.1) LL=KL
      IF(LO.EQ.2) LL=KL+3
      DO 800 I=1,7260
800   F(I)=0.0
      READ(61=LL) F
      IF(LO.LT.3) GO TO 1700
      DO 1600 I=1,39
      DO 1600 J=79,120
      KM=(J*J-J)/2+I
 1600 F(KM)=-F(KM)
1700  CONTINUE
      DO 700 J=1,7260
      F(J)=F(J)*P(KL)
700   R(J)=R(J)+F(J)
      DO 900 K=109,120
      DO 900 L=109,120
      K1=K-108
      L1=L-108
      A(K1,L1)=0.0
      B=0.0
      C=0.0
      DO 1300 I=1,120
      DO 1300 J=1,120
      KI=(K-1)*120+I
      LJ=(L-1)*120+J
      IJ=J*(J-1)/2+I
      JI=I*(I-1)/2+J
      IF(I-J) 1100,1200,1200
1100  A(K1,L1)=A(K1,L1)+S(KI)*R(IJ)*S(LJ)
      GO TO 1300
1200  IF(LO-3) 1800,1900,1800
1800  A(K1,L1)=A(K1,L1)+S(KI)*R(JI)*S(LJ)
      GO TO 1300
1900  A(K1,L1)=A(K1,L1)-S(KI)*R(JI)*S(LJ)
1300  CONTINUE
      B=A(K1,L1)*A(K1,L1)
      C=B*EC(L)-B*EC(K)
      WRITE(6,1112) EC(K),EC(L),A(K1,L1),B,C,K,L
900   CONTINUE
      WRITE(6,1111) ((A(K1,L1),L1=1,12),K1=1,12)
1400  CONTINUE
      LOCK 61
      END
```

```
      FILE  60=OURS/H120,UNIT=DISK,RECORD=7260,AREA=13*1,SAVE=1
      FILE  70=OURS/H3942,UNIT=DISK,RECORD=1000,AREA=20*1,SAVE=1
C
C     ******************************************************************************
C     PROGRAM      OSCSTRENGTHS/H3942
C
C     CALCULATES MAGNETIC DIPOLE OSCILLATOR STRENGTHS FOR THE 12 LOWEST
C     CRYSTAL FIELD LEVELS OF COBALT FOR THE CASE OF AN APPLIED
C     MAGNETIC FIELD ALONG THE Z AXIS.
C     ******************************************************************************
C     INPUT DATA REQUIRED   NUMBERS IN THE 5F10.6 FORMAT,INTEGERS IN I10
C
C     FIRST DATA CARD  AN INDEX SPECIFYING THE MATRIX ELEMENTS REQUIRED
C                      ITS VALUE IS SET TO 1 FOR ALL THE L + 2S ELEMENTS
C                      ITS VALUE IS SET TO 2 FOR THE S ELEMENTS ONLY
C                      ANY OTHER VALUE GIVES THE OSC. ST. L + 2S EL ONLY
C     SECOND DATA CARD THE PARAMETERS DQ,B,C,S,Z,V AND W
C     THIRD DATA CARD  THE APPLIED MAGNETIC FIELD IN KILOGAUSS
C
C     CPU TIME                    120 SECONDS       COST   3.50 DOLLARS
C     CPU TIME FOR ZERO FIELD      75 SECONDS       COST   2.50 DOLLARS
C     ******************************************************************************
      DIMENSION P(10),E(1000),R(1000),S(1800),PP(10),T(168),
     C ED(42,2),GA(480),U(1000),SS(1800),W(168),EG(42),G(480,2),H(7260),
     C B(7260)
 1000 FORMAT(8F10.6)
 1001 FORMAT(1HO,10F12.4)
 1002 FORMAT(1HO,' THE CRYSTAL FIELD PARAMETERS B20,B40, AND B43')
 1003 FORMAT(1HO,' THE PARAMETERS DQ,B,C,S,Z,V,W,K,L, AND M')
 1004 FORMAT(1HO,' GAMMA FOUR MINUS EIGENVALUES')
 1005 FORMAT(1HO,' GAMMA FIVE AND SIX EIGENVALUES')
 1006 FORMAT(1HO,10F12.4)
 1007 FORMAT(1HO,' AN EIGENVALUE OF THE GAMMA 4 MINUS MATRIX',F25.4)
 1008 FORMAT(1HO,'   EIGENFUNCTION')
 1009 FORMAT(1HO,10F12.4)
 1010 FORMAT(1HO,' ENERGIES,G PARALLEL VALUES AND OSCILLATOR STRENGTHS')
 1011 FORMAT(1HO,103X,' G PARALLEL VALUE')
 1012 FORMAT(1HO,4F30.6)
 1013 FORMAT(1HO,4F30.6)
 1014 FORMAT(20F6.2)
 1015 FORMAT(1HO,3I10)
 1016 FORMAT(F10.6)
 1017 FORMAT(1HO,' OSCILLATOR STRENGTHS FOR THE GAMMA 4 MINUS STATES')
 1018 FORMAT(1HO,' MAGNETIC FIELD IN KILOGAUSS',F10.4)
 1019 FORMAT(1HO,104X,' G PERPENDICULAR')
 1020 FORMAT(1HO,' AN EIGENVALUE OF THE GAMMA 5,6 MATRIX',F25.4)
 1021 FORMAT(1HO,' CORR. EIGENVALUE OF THE GAMMA 4 PLUS MATRIX',F25.4)
 1022 FORMAT(1HO,' OSCILLATOR STRENGTHS FOR THE GAMMA 4 PLUS STATES')
 1023 FORMAT(1HO,' OSCILLATOR STRENGTHS FOR THE GANMA FIVE,SIX STATES')
 1024 FORMAT(1HO,' GAMMA FOUR PLUS EIGENVALUES')
 1025 FORMAT(I10)
 1026 FORMAT(1HO,' THIS PARAMETER IS 2 FOR SPIN ONLY MATRIX EL',I10)
 1030 FORMAT(1HO,' INITIAL STATE  FINAL STATE  MATRIX ELEMENT  OSC ST.')
 1031 FORMAT(1HO,' OSC STRENGTHS BETWEEN GAMMA 5,6 AND 4 MINUS STATES')
 1032 FORMAT(1HO,' OSC STRENGTHS BETWEEN GAMMA 4 MINUS AND PLUS STATES')
 1033 FORMAT(1HO,' OSC STRENGTHS BETWEEN GAMMA 5,6 AND 4 PLUS STATES')
 1034 FORMAT(1HO,16X,' INITIAL STATE',19X,'FINAL STATE',16X,
     C'MATRIX ELEMENT',11X,'OSCILLATOR STRENGTH')
      S23=SQRT(2.0/3.0)
      S2=SQRT(2.0)
```

```
      S107=SQRT(10.0/7.0)
      READ(5,1025) NS
      WRITE(6,1026) NS
      READ(5,1000) (P(I),I=1,7)
      P(8)=-P(4)/535.0
      P(9)=-P(5)/535.0
      P(10)=2.0
      WRITE(6,1003)
      WRITE(6,1001) (P(I),I=1,10)
      P(6)=P(6)*S23
      P(7)=P(7)*S2
      READ(5,1016) FIELD
      WRITE(6,1018) FIELD
      FX=FIELD*0.04668
      DO 3200 I=8,10
3200  PP(I)=P(I)*FX
      DO 150  JJ=1,2
      DO 100 I=1,1000
      U(I)=0.0
 100  R(I)=0.0
      N=39+(JJ-1)*3
      NP=(N*N+N)/2
      DO 200 KL=1,7
      LL=KL+(JJ-1)*10
      READ(70=LL)E
      Z=P(KL)
      DO 200 I=1,NP
 200  R(I)=R(I)+E(I)*Z
      IF(FIELD.EQ.0.0) GO TO 4100
      DO 3300 KL=8,10
      LL=KL+(JJ-1)*10
      READ(70=LL)E
      Z=PP(KL)
      DO 3300 I=1,NP
3300  U(I)=U(I)+E(I)*Z
      DO 3400 I=1,NP
3400  R(I)=R(I)-U(I)
      IF(JJ.EQ.2) GO TO 4100
      DO 3500 I=1,NP
3500  U(I)=R(I)+2.0*U(I)
      CALL EIGEN(U,SS,N,0)
4100  CONTINUE
      CALL EIGEN(R,S,N,0)
      IF(JJ.EQ.1) ZERO=R(NP)
      DO 300 I=1,N
      IP=(I*I+I)/2
      ED(I,JJ)=R(IP)-ZERO
 300  CONTINUE
      IF(FIELD.EQ.0.0) GO TO 350
      IF(JJ.EQ.2) GO TO 350
      DO 350 I=1,N
      IP=(I*I+I)/2
      EG(I)=U(IP)-ZERO
 350  CONTINUE
      IF(JJ.EQ.1) WRITE(6,1004)
      IF(JJ.EQ.2) WRITE(6,1005)
      WRITE(6,1006) (ED(I,JJ),I=1,N)
      IF(FIELD.EQ.0.0) GO TO 4200
      IF(JJ.EQ.1) WRITE(6,1024)
      IF(JJ.EQ.1) WRITE(6,1006) (EG(I),I=1,N)
4200  CONTINUE
      N4=N*4
      DO 500 I=1,N4
      IM=1365+(JJ-1)*231+I
 500  T(I)=S(IM)
      IF(FIELD.EQ.0.0) GO TO 450
```

```
126          IF(JJ.EQ.2) GO TO 450
127          DO 450 I=1,N4
128          IM=1365+I
129          W(I)=SS(IM)
130    450   CONTINUE
131          DO 700 I=1,1000
132    700   R(I)=0.0
133          IF(NS.EQ.2) GO TO 5200
134          DO 800 KL=8,10
135          LL=KL+(JJ-1)*10
136          READ(70=LL)E
137          Z=P(KL)
138          DO 800 I=1,NP
139    800   R(I)=R(I)+E(I)*Z
140          GO TO 5150
141   5200   LL=JJ*10
142          READ(70=LL)R
143   5150   CONTINUE
144          DO 900 KP=1,2
145          IF((KP.EQ.2).AND.(FIELD.EQ.0.0)) GO TO 900
146          IF((KP.EQ.2).AND.(JJ.EQ.2)) GO TO 900
147          IF((JJ.EQ.1).AND.(KP.EQ.1)) WRITE(6,1017)
148          IF((JJ.EQ.1).AND.(KP.EQ.2)) WRITE(6,1022)
149          IF(JJ.EQ.2) WRITE(6,1023)
150          WRITE(6,1034)
151          DO 900 K=1,4
152          K35=K+35+(JJ-1)*3
153          DO 900 L=1,4
154          L35=L+35+(JJ-1)*3
155          IF((NS.EQ.1).OR.(NS.EQ.2)) GO TO 5300
156          IF((K.LT.4).AND.(K.NE.L)) GO TO 900
157          IF((JJ.EQ.2).AND.(K.NE.L)) GO TO 900
158   5300   CONTINUE
159          A=0.0
160          D=0.0
161          IF(KP.EQ.2) GO TO 3600
162          DO 1100 I=1,N
163          DO 1100 J=1,I
164          KI=(K-1)*N+I
165          LJ=(L-1)*N+J
166          JI=(I*I-I)/2+J
167          A=A+T(KI)*R(JI)*T(LJ)
168   1100   CONTINUE
169          DO 1150 J=2,N
170          DO 1150 I=1,J-1
171          KI=(K-1)*N+I
172          LJ=(L-1)*N+J
173          IJ=(J*J-J)/2+I
174          A=A+T(KI)*R(IJ)*T(LJ)
175   1150   CONTINUE
176          IF(K.EQ.L) WRITE(6,1011)
177          IF(K.EQ.L) D=2.0*A
178          IF(K.NE.L) D=A*A*ED(L35,JJ)
179          WRITE(6,1012) ED(K35,JJ),ED(L35,JJ),A,D
180          GO TO 900
181   3600   CONTINUE
182          DO 4400 I=1,N
183          DO 4400 J=1,I
184          KI=(K-1)*N+I
185          LJ=(L-1)*N+J
186          JI=(I*I-I)/2+J
187          A=A+W(KI)*R(JI)*W(LJ)
188   4400   CONTINUE
189          DO 4450 J=2,N
190          DO 4450 I=1,J-1
191          KI=(K-1)*N+I
```

```
      LJ=(L-1)*N+J
      IJ=(J*J-J)/2+I
      A=A+W(KI)*R(IJ)*W(LJ)
4450  CONTINUE
      C=-A
      IF(K.EQ.L) WRITE(6,1011)
      IF(K.EQ.L) D=2.0*C
      IF(K.NE.L) D=A*A*EG(L35)
      WRITE(6,1012) EG(K35),EG(L35),C,D
 900  CONTINUE
      DO 550 I=1,480
 550  G(I,JJ)=0.0
      IF(JJ.EQ.2) GO TO 1250
      DO 1250 I=1,480
      GA(I)=0.0
1250  CONTINUE
      DO 600 K=1,4
      DO 600 I=1,N
      IR=I+(K-1)*120+(JJ-1)*78
      IM=1365+(JJ-1)*231+(K-1)*N+I
 600  G(IR,JJ)=S(IM)
      IF(FIELD.EQ.0.0) GO TO 150
      IF(JJ.EQ.2) GO TO 150
      DO 650 K=1,4
      DO 650 I=1,N
      IR=I+39+(K-1)*120+(JJ-1)*39
      IM=1365+(K-1)*N+I
 650  GA(IR)=SS(IM)
 150  CONTINUE
      IF(NS.EQ.2) GO TO 5400
      DO 1400 I=1,7260
1400  H(I)=0.0
      DO 1500 KL=8,10
      LL=KL+3
      READ(60=LL) B
      Z=P(KL)
      DO 1500 I=1,7260
1500  H(I)=H(I)+B(I)*Z
      GO TO 5500
5400  CONTINUE
      READ(60=13)H
5500  CONTINUE
      DO 1600 JJ=1,2
      DO 1600 KP=1,2
      IF((KP.EQ.2).AND.(FIELD.EQ.0.0)) GO TO 1600
      IF((KP.EQ.1).AND.(JJ.EQ.1)) GO TO 1600
      IF((KP.EQ.1).AND.(JJ.EQ.2)) WRITE(6,1031)
      IF((KP.EQ.2).AND.(JJ.EQ.1)) WRITE(6,1032)
      IF((KP.EQ.2).AND.(JJ.EQ.2)) WRITE(6,1033)
      WRITE(6,1034)
      JA=1
      N1=1+(JJ-1)*78
      N2=N1+38+(JJ-1)*3
      DO 1600 K=1,4
      K35=K+35+(JJ-1)*3
      DO 1600 L=1,4
      L35=L+35
      A=0.0
      D=0.0
      IF(KP.EQ.2) GO TO 2600
      IF((NS.EQ.1).OR.(NS.EQ.2)) GO TO 5700
      IF(L.LT.4) GO TO 1600
5700  CONTINUE
      DO 1700 I=79,120
      DO 1700 J=1,39
      KI=(K-1)*120+I
```

```
      LJ=(L-1)*120+J
      IJ=(J*J-J)/2+I
      JI=(I*I-I)/2+J
      IF(I-J) 2200,2300,2300
2200  A=A+G(KI,JJ)*H(IJ)*G(LJ,JA)
      GO TO 1700
2300  A=A+G(KI,JJ)*H(JI)*G(LJ,JA)
1700  CONTINUE
      D=A*A*ED(K35,JJ)
      WRITE(6,1013) ED(K35,JJ),ED(L35,JA),A,D
      GO TO 1600
2600  CONTINUE
      IF((NS.EQ.1).OR.(NS.EQ.2)) GO TO 5100
      IF((JJ.EQ.2).AND.(L.LT.4)) GO TO 1600
      IF(JJ.EQ.2) GO TO 5100
      IF((K.LT.4).AND.(K.NE.L)) GO TO 1600
5100  CONTINUE
      DO 2900 I=N1,N2
      DO 2900 J=40,78
      KI=(K-1)*120+I
      LJ=(L-1)*120+J
      IJ=(J*J-J)/2+I
      JI=(I*I-I)/2+J
      IF(I-J) 2700,2800,2800
2700  A=A+G(KI,JJ)*H(IJ)*GA(LJ)
      GO TO 2900
2800  A=A+G(KI,JJ)*H(JI)*GA(LJ)
2900  CONTINUE
      IF((JJ.EQ.1).AND.(K.EQ.L))  WRITE(6,1019)
      D=A*A*ED(K35,JJ)
      IF(JJ.EQ.1) D=A*A*EG(L35)
      IF((JJ.EQ.1).AND.(K.EQ.L)) D=2.0*A
      WRITE(6,1013) ED(K35,JJ),EG(L35),A,D
1600  CONTINUE
2400  CONTINUE
      LOCK 60
      LOCK 70
      STOP
      END
```